

MULTIPHYSICS NATURE OF LITHIUM-ION BATTERY SAFETY ISSUES

by

Yikai Jia

A dissertation submitted to the faculty of  
The University of North Carolina at Charlotte  
in partial fulfillment of the requirements  
for the degree of Doctor of Philosophy in  
Mechanical Engineering

Charlotte

2022

Approved by:

---

Dr. Jun Xu

---

Dr. Qiuming Wei

---

Dr. Robert Cox

---

Dr. Mesbah Uddin

---

Dr. Tao Hong



## ABSTRACT

YIKAI JIA. Multiphysics nature of Lithium-ion Battery safety issues  
(Under the direction of DR. JUN XU)

Safety issues of lithium-ion batteries (LIBs) are usually initiated from an internal short circuit (ISC) that can be triggered by external accidental abusive loadings. The generated heat and the increased temperature would lead to several complicated physio-chemical changes of the batteries, *e.g.*, thermal runaway (TR). Thus, investigation of the multiphysics behaviors of lithium-ion batteries becomes a vital task to understand the battery safety issues. Experimental characterization and numerical simulation are essential ways to understand the underlying nature of the multiphysics behavior of batteries. However, experimental observation may only provide insufficient data due to the limitation of experimental technology, particularly for *in-situ* or *operando* experiment methodologies. Herein, a multiphysics modeling framework is developed. The framework provides a fundamental description and understanding of the safety behaviors of the battery cells. Next, the multiphysics framework is used to evaluate the safety risk of LIB cells. Two kinds of key safety risks evaluation problems are defined: ISC triggering risk and safety risk level. Machine learning (ML) models with data-driven algorithms are used to fast and accurately solve the related regression and classification problems. In terms of ISC triggering risk, an ISC risk evaluation model is first developed based on the training dataset generated by the combination of experimental data and simulation data. A Representative Volume Element (RVE) based mechanical model, which can predict accurate mechanical behaviors at a

much lower calculation time cost, is established to assist the data generation. The safety risk prediction high-level performance of the Support Vector Regression (SVR) predictors are indicated by various testing cases and scenarios. In terms of safety risk level evaluation, a safety risk level classification model is developed to classify the cell's safety levels under various work conditions. Random Forest (RF) classifiers are used to construct the model and realize the cell state classification based on only a short period of voltage and current signals. The multiphysics model is used as a surrogate model to generate as much as training samples, that cover various State of Charges (SOCs), short circuit resistances, and Charging/discharging-rates (C-rates), are generated. The prediction results show that the classifiers have a good performance and robustness. Finally, two typical safety issues: cell defect and TR propagation are systematically studied. The defective cells are characterized both electrochemically and mechanically to discuss the consequent ISC and thermal runaway triggering behaviors and modes. The multiphysics model will be used to provide necessary auxiliary instructions of the related mechanisms. Possible defect detection and identification indicators are also summarized. TR propagation behaviors of battery packs are also experimentally and numerically investigated. The pack level TR model is developed based on the multiphysics model via doing some simplifications and adding the coupling relationships among cells. Two major thermal spread modes are discovered, and their governing factors are discussed. Thus, the TR propagation mechanism is revealed to some extent. This study comprehensively investigates the multiphysics behavior of LIB

cells under mechanical abusive loadings, highlights the promise of the LIB cell multiphysics modeling framework. The multiphysics models provide fundamental understanding and insights of battery safety issues, as well as an innovative solution for risk evaluation and safety risk recognition.

## ACKNOWLEDGMENTS

I would like to offer my extreme gratitude to my supervisor, Prof. Xu for his invaluable supervision, support, and tutelage in all the time of my academic research and daily life

I would also like to thank my committee members, Dr. Qiuming Wei, Dr. Robert Cox, Dr. Mesbah Uddin, and Dr. Tao Hong for their insightful comments and suggestions

I would like to express my sincere gratitude to every member of our research group, especially Dr. Xiang Gao, Dr. Wen Zhang, Ms. Jiani Li, Mr. Chunhao Yuan, and Mr. Xudong Duan, for their unwavering support. Their kind help and support with modeling issues and experiments designs and equipment setups. that have made my study and life in the college a wonderful time.

I would like to extend my sincere thanks to all my co-authors, especially Prof. Binghe Liu, Prof. Lubing Wang, Mr. Weiran Yao who provide me with treasured support which was influential in shaping my research methodology and knowledge at the very beginning of my research.

I am deeply grateful to my parents for their tremendous understanding and encouragement.

## TABLE OF CONTENTS

|  |      |
|--|------|
| LIST OF TABLES .....   | xii  |
| LIST OF FIGURES .....  | xiii |
| NOMENCLATURE.....  | xix  |
| CHAPTER 1 INTRODUCTION .....                                     | 1    |
| 1.1 Background.....  | 1    |
| 1.2 Literature review.....                                       | 1    |
| 1.2.1 Multiphysics behaviors of lithium-ion batteries .....      | 1    |
| 1.2.2 Stress-induced internal short circuit.....                 | 3    |
| 1.2.3 Thermal runaway triggering and propagation.....            | 5    |
| 1.2.4 Safety risk evaluation based on multiphysics modeling..... | 7    |
| 1.3 Challenges and motivation.....                               | 10   |
| 1.4 Chapter arrangement.....                                     | 11   |
| CHAPTER 2 MULTIPHYSICS BATTERY SAFETY BEHAVIORS.....             | 13   |
| 2.1 ISC risk .....   | 13   |
| 2.2 Safety risk levels .....                                     | 14   |
| 2.3 Multiphysics modeling framework.....                         | 16   |
| 2.3.1 Sub-models .....   | 16   |
| 2.3.2 Coupling relationships .....                               | 19   |
| CHAPTER 3 INTERNAL SHORT CIRCUIT RISK UPON MECHANICAL            |      |

|  |    |
|--|----|
| ABUSIVE LOADING.....   | 22 |
| 3.1 Methods.....   | 22 |
| 3.1.1 Mechanical loading tests.....                              | 22 |
| 3.1.2 Finite element simulation.....                             | 25 |
| 3.1.3 Machine learning algorithm.....                            | 29 |
| 3.2 Results and discussion .....                                 | 30 |
| 3.2.1 Data generation .....                                      | 31 |
| 3.2.2 Machine learning approach and safety risk prediction. .... | 39 |
| 3.2.3 Generalization .....                                       | 42 |
| 3.2.4 Rationalization .....                                      | 45 |
| 3.2.4.1 Advantages.....  | 45 |
| 3.2.4.2 Pre-conditions and Limitations.....                      | 48 |
| 3.3 Conclusions.....   | 50 |
| CHAPTER 4 SAFETY RISK LEVELS UPON STRESS-DRIVEN                  |    |
| INTERNAL SHORT CIRCUIT.....                                      | 52 |
| 4.1 Methods.....   | 52 |
| 4.1.1 Experimental designs and typical results.....              | 52 |
| 4.1.2 Multiphysics model development.....                        | 54 |
| 4.1.3 Machine learning model development.....                    | 56 |
| 4.2 Data generation and model development.....                   | 57 |

|   |    |
|---|----|
| 4.2.1 Data generation process .....                                   | 57 |
| 4.2.2 Multiphysics surrogate model and parametric calculation. ....   | 58 |
| 4.2.3 Feature selection and model structure design .....              | 59 |
| 4.3 Predictive performance .....                                      | 63 |
| 4.3.1 Model variants and computing setup. ....                        | 63 |
| 4.3.2 Performance of the classifiers. ....                            | 64 |
| 4.3.2 Feature importance analysis.....                                | 71 |
| 4.3.3 Robustness analysis. ....                                       | 72 |
| 4.3.4 Impact of input period and short circuit resistance range. .... | 73 |
| 4.4 Conclusions.....  | 75 |

## CHAPTER 5 SAFETY RISKS OF MECHANICAL DEFECTIVE

|   |    |
|---|----|
| LITHIUM-ION BATTERIES .....                                   | 77 |
| 5.1 Methods.....  | 77 |
| 5.1.1 Manufacture of a defective battery. ....                | 77 |
| 5.1.2 Electro-chemo-thermal coupling model. ....              | 79 |
| 5.1.3 Mechanical test for safety evaluation. ....             | 83 |
| 5.1.4. Mechanical finite element model.....                   | 85 |
| 5.2 Results.....  | 87 |
| 5.2.1 Characterization of defective batteries.....            | 87 |
| 5.2.2 Effect of defect at different sizes and positions. .... | 94 |

|   |     |
|---|-----|
| 5.3 Discussion.....   | 96  |
| 5.3.1 Electrochemical-thermal safety evaluation of defective battery.....   | 96  |
| 5.3.2 Mechanical safety evaluation of defective battery.....                | 98  |
| 5.3.3 Key features for early detection of defective batteries .....         | 101 |
| 5.4 Conclusion .....  | 103 |
| CHAPTER 6 THERMAL RUNAWAY PROPAGATION WITHIN                                |     |
| A BATTERY PACK.....   |     |
| 6.1 Methods.....  | 105 |
| 6.1.2 Experimental battery samples .....                                    | 105 |
| 6.1.2 Thermal runaway propagation experiment design.....                    | 106 |
| 6.1.3 Establishment of the thermal runaway propagation model.....           | 107 |
| 6.2 Results and discussion .....  | 116 |
| 6.2.1 Experimental results and calibration of the model .....               | 116 |
| 6.2.2 Thermal runaway propagation of large pack under ideal conditions..... | 119 |
| 6.2.3 Propagation modes and speed.....                                      | 122 |
| 6.2.4 Thermal runaway propagation under random thermal conditions .....     | 126 |
| 6.3 Conclusions.....  | 127 |
| CHAPTER 7 CONCLUDING REMARKS.....   | 129 |
| REFERENCES .....  | 131 |
| APPENDIX A: Support Vector Regression Problem.....                          | 141 |

|  |     |
|--|-----|
| APPENDIX B: Multiphysics Model Setups for Data Generation .....            | 142 |
| APPENDIX C: Feature Analysis for Safety Risk Classification .....          | 145 |
| APPENDIX D: Calculation of Steady-state Temperature of Defective Cell..... | 148 |
| APPENDIX E: PERMISSION LETTERS .....                                       | 150 |

## LIST OF TABLES

|  |     |
|--|-----|
| Table 1 Summary of the experimental setup.....   | 23  |
| Table 2 Basic information of cylindrical cells. ....   | 31  |
| Table 3 Basic information of pouch cells. ....   | 31  |
| Table 4 Summary of all the generated training samples. ....  | 38  |
| Table 5 The training/ testing sample combinations and<br>corresponding model parameters. ....                            | 39  |
| Table 6 Comparisons of the ISC distance between experimental results and<br>ML predictions. ....                         | 44  |
| Table 7 Experimental setup of the cycling tests.....   | 54  |
| Table 8 Comparison between different classification models. ....   | 64  |
| Table 9 Performance of the classification models. ....   | 66  |
| Table 10 Comparison between typical methodologies of battery cell<br>safety risk prediction. ....                        | 69  |
| Table 11 Basic information about battery samples. ....   | 79  |
| Table 12 Equations for chemical reaction and phase change.....   | 82  |
| Table 16 Values used in the equations for chemical reaction and phase change. ....                                       | 82  |
| Table 14 Estimation of characteristic parameters of the defects at different conditions ..                               | 95  |
| Table 15 Key features of defective batteries produced by<br>the local foreign body intrusion. ....                       | 102 |
| Table 16 Parameter values and data sources. ....   | 114 |
| Table 17 Comparison of triggering time and temperature rise between<br>experimental results and simulation results. .... | 119 |

## LIST OF FIGURES

|   |    |
|---|----|
| Figure 1 Multiphysics behaviors of safety issues of LIBs <sup>15</sup> .....  | 2  |
| Figure 2 Typical results of battery mechanical abusive loading test <sup>19</sup> .....   | 3  |
| Figure 3 Failure criteria established based on simulation and experimental data <sup>5, 31, 32</sup> ....   | 5  |
| Figure 4 Experimental results of TR and TR propagation test <sup>8, 11</sup> .....  | 6  |
| Figure 5 Multiphysics modeling framework of LIBs <sup>48</sup> .....  | 8  |
| Figure 6 Evaluation of battery safety under mechanical loading based on ML methods.   | 10 |
| Figure 7 Achievement of the safety risk. ....   | 14 |
| Figure 8 Different short circuit evolution processes. (a) voltage/ temperature behaviors of three common evolution processes. (b) comparison of voltage behaviors between normal cells and defective cells. ....  | 16 |
| Figure 9 Framework of the multiphysics modeling.....  | 21 |
| Figure 10 Schematic diagram of the experimental designs and mechanical test platform.....   | 24 |
| Figure 11 Tests of stacked-layer samples of 18650 cells (a) The stacking structure of the battery jellyroll. Experimental designs of stacked-layer samples: (b) cylinder radial indentation; (c) cylinder axial indentation. ....                           | 25 |
| Figure 12 Radial compression tests of 18650 cells. (a) 0%-offset, 0%; (b) 60%-offset, 0%; (c) 0%-offset, 50%; (d) 60%-offset, 50%; .....  | 26 |
| Figure 13 Indentation tests of 18650 cells. (a) 0-degree, 0%; (b) 0-degree, 30%; (c) 0-degree, 60%; (d) 45-degree, 0%; (e) 45-degree, 60%.....  | 27 |
| Figure 14 Three-point bending of 18650 cells. (a) 50mm-span, 0%; (b) 50mm-span, 60%; (c) 40mm-span, 0%; (d) 40mm-span, 60%; .....   | 28 |
| Figure 15 Tests of stacked-layer samples of pouch cells. (a) D = 1 mm; (b) D = 1.5 mm; (a) D = 2 mm; (b) D = 2.5 mm; .....  | 29 |
| Figure 16 Tests of pouch cells. (a) out-of-plane compression; (b) 20mm-diameter sphere indentation. ....  | 29 |
| Figure 17 Finite element modeling methods of cells. (a) Mechanical modeling flow chart and testing curves of cell constituents in (b) the ZZ direction and (c) XX/ YY directions. (d) Equivalent stress-strain curves are computed from the RVE model. .... | 33 |

|   |    |
|---|----|
| Figure 18 Experimental designs and test results. Experimental results of stacked-layer samples: (a) cylinder radial indentation; (b) cylinder axial indentation of cylindrical cells, and (c) particle indentation of pouch cells. Experimental results of single-cell samples: (d) 0%-offset compression, (e) 50%-offset compression, (f) 0-degree indentation, (g) 45-degree indentation, (h) 50mm-span three-point bending, and (i) 40mm-span three-point bending of cylindrical cell; (j) out-of-plane compression, and (k) 20mm-diameter sphere indentation of pouch cells. .... | 35 |
| Figure 19 Generation methodology of the argument vectors and their mapping relationship. (a) the generation of argument vector $X$ , (b) the mapping relationship between $X$ and $Y$ . ....  | 37 |
| Figure 20 The flow chart of the offline training and online prediction processes. ....  | 39 |
| Figure 21 Safety risk evaluation of two types of cells under testing loading conditions. 18650 cylindrical cells under (a) radial compression loading, (b) indentation loading, and (c) three-point bending. And pouch cells under (d) compression loading, and (e) 20mm-diameter sphere indentation loading. (Predicter 1 for Cases a,b, c and Predict 2 for Cases d, e).....  | 42 |
| Figure 22 Safety risk prediction of cylindrical cells at different SOCs and under different loading conditions. (a) Safety risks at different SOCs, (b) interpolation prediction of safety risk of cells with 30%-SOC under radial compression loading. Extrapolation prediction of safety risk of cells under: 50%-offset radial compression at (c) 0%-SOC and (d)-60% SOC; 45-degree indentation at (e) 0%-SOC and (f) 60%-SOC. (Predicter 3 for Case b and Predicter 4 for Cases c-e).....   | 44 |
| Figure 23 Validation of the FE model for the MC criterion. The model is validated by two typical loading conditions (a) radial compression, (b) indentation, and (c) 50-mm three-point bending (Simulation 1: the FE model developed in this paper; Simulation 2: the homogenous model developed for MC failure criterion from Ref. <sup>5, 45</sup> ). ....  | 47 |
| Figure 24 Comparison between the SVR predictor and the Mohr-Coulomb failure criterion. (a) Determination of the fracture line. (b) Comparison of ISC displacement prediction between the SVR predictor and the MC criterion (average value for experiment and the SVR predictor). Case 1: radial compression; case 2: indentation; case 3: 50-mm three-point bending; case 4: 50%-offset radial compression; case 5: 45-degree indentation; case 6: 40-mm three-point bending. ....   | 48 |
| Figure 25 Classification of battery safety issues. (a) Cycling test experimental  |    |

|   |    |
|---|----|
| design and the typical behaviors: (b) L0 normal battery; (c) L1 damaged battery; (d) ISC triggering test experiment design and the typical behaviors: (e) L2 ISC is triggered but no TR; (f) L3 ISC is triggered, and TR will be triggered. ....  | 54 |
| Figure 26 Framework of the multiphysics modeling.....   | 55 |
| Figure 27 Multiphysics model validation. Validation of the battery model at different C-rates:(a) 0.1C; (b) 0.2C; (c) 0.5C; (d) 1C. Validation of the thermal transfer model at different SOCs: (e) 0.3SOC; (f) 0.6SOC; (g) 0.8SOC; (h) 0.1SOC.....   | 56 |
| Figure 28 Datasets regroup process .....  | 57 |
| Figure 29 Data generation process.....  | 58 |
| Figure 30 Parametric calculation results. (a) Results of the battery model at different C-rates and short circuit resistance; (e) Results of the coupling model at different initial SOCs and short circuit resistances (dots represent data points).....   | 59 |
| Figure 31 Fundamental model structure and training process of the ML classification model.....  | 62 |
| Figure 32 Feature distribution for C0 .....   | 62 |
| Figure 33 Feature distribution for C1 .....   | 62 |
| Figure 34 Feature distribution for C2 .....   | 63 |
| Figure 35 Validation and performance of the classification models. Confusion matrix of (a) C0;(b) C1; (c) C2 (horizontal labels represent prediction results, vertical labels represent their true labels, elements in the matrix present the ratio of samples with the predicted label in their true group). Receiver operating characteristic (ROC) curves (d) C0;(e) C1; (f) C2; ..... | 65 |
| Figure 36 Prediction process demonstration. Prediction process of four scenarios: (a) L0, normal cell during 1C discharging; (b) L1, defective cell during 1C discharging; (c) L2, ISC is triggering during 0.1 C charging (TR is not triggered) (d) L3, ISC is triggering during 0.1 C charging (TR is not triggered) (Level=-1 means risk level is unknown).....                        | 67 |
| Figure 37 Feature importance analysis of classifiers C1 and C2. Feature importance based on permutation method and crosstab for selected features under top 25% sample (averaged feature values of X in tests samples   |    |

|   |    |
|---|----|
| with top or bottom 25% possibility given by the classifiers): (a) C1 (b) C2.....  | 72 |
| Figure 38 Performance analysis of classifiers. Robustness: Prediction score of classifiers C1 and C2 with (a) current error ( $u_e=0$ mA) and (b) voltage error ( $i_e=0$ mA). $\Delta t_s$ is set as 1 min and $\Delta t_1$ is set as 5 min; Effects of period selection and resistance range on prediction accuracy: Prediction scores when (c) normalized period increase and (d) max resistance of damaged batteries increases. ....                          | 74 |
| Figure 39 Schematic diagram of the screw indentation experiment.....  | 78 |
| Figure 40 1C CC-CV voltage-time curve for cell used during the screw indentation.....   | 79 |
| Figure 41 Modeling of the multi-physics model. (a) Coupling strategies. (b) geometry, boundary conditions, and heat source setting of the model. The ISC heat is produced by ISC resistance, the discharging heat is produced by the internal resistance. The convection cooling is considered. ....  | 81 |
| Figure 42 Validations of the sub-models within the multiphysics coupling model. (a) Battery model. Comparison of discharging voltage curves at different rates between simulation and experiment; (b) Electrochemical-thermal coupling model. Comparison of voltage, temperature curve after the onset of the ISC during the screw penetration loading.   | 81 |
| Figure 43 Experiment Methods. (a) Particle indentation, the diameter of the indenter is 10 mm, the loading rate is 2 mm/min; (b) 3-point bending, the span is 60 mm, the loading rate is 2mm/min. The indentation and 3-point bending experiment were conducted on an INSTRON 2345. (c) 160 mm free drop, a smartphone drop test machine was used. The voltage (OCV) and temperature (K-type thermocouple) signals are measured by a 34970A data acquisition..... | 84 |
| Figure 44 Material properties for the battery model. The model used here is an anisotropic elastoplastic homogenous model. (a) Constitutive relationship obtained by out-of-plane compression test; (b) In-plane elastic modulus estimated by three-point bending; (c) Material coordinate system definition. ....  | 86 |
| Figure 45 Geometries and boundary conditions of the FE mechanical model. (a) Local compression loading; (b) Three-point bending; (c) Free drop loading; (d) Modeling of defected area. ....   | 86 |
| Figure 46 Validation of the finite element model. (a) normal battery indentation; (b) defected battery indentation. (c) normal battery 3-point bending. (d) defected battery 3-point bending.....   | 87 |

- Figure 47 Cell behaviors during mechanical indentation. (a) Force, voltage, and temperature responses of the battery during the loading; (b) Schematic diagram of the battery's physical appearance..... 89
- Figure 48 Differences of electrochemical characteristics between defective batteries and normal batteries. (a) Comparison of 1C CC-CV cycling curve, charging cutoff voltage is 4.4V, discharging cutoff voltage is 3.7V, cutoff rate of CV charging is set as 1/50 C; (b) Comparison of the impedance spectroscopy curve, the ohmic internal resistance and polarization resistance changes little; (c) The self-discharging phenomenon indicates a micro ISC. .... 91
- Figure 49 Changes in electrochemical characteristics of the defected battery. (a) comparison of 1C CC-CV cycling capacity curves between the defected battery and the normal battery; (b) Comparison of CV stage period-cycle curve..... 91
- Figure 50 The defect producing process and the internal change of the battery. (a) The damaged area and its distribution of each reaction within the defective battery. The first 10 layers are shown here. Note that the thickness of the collector and separator are small such that the displayed colors look light. (b) Schematic diagram of short-circuit evolution... 93
- Figure 51 Effect of different defect areas and positions. (a) Capacity loss and leakage at different indenter size (center position); (b) Capacity loss and leakage at different positions (2mm defect)..... 95
- Figure 52 Effect of indenter sizes and indentation positions (1C CC cycling, sphere steel particle). (a) voltage response at different indenter size (from 1.0 mm to 2.5 mm diameter, center); (b) voltage response at different positions (0, 10, 20 mm from center, 2 mm)..... 95
- Figure 53 Cycling steady-state temperature at different short-circuit resistance and ambient temperature. Assessment of safety level based on average temperature. .... 97
- Figure 54 Mechanical safety of the defective battery. (a) Compression loading at 2 mm/min (screw, center), the critical failure force of defective battery has a significant decrease due to stress concentration; (b) 2mm/min 60mm span 3-point bending, no failure but a peak decrease for the defective battery; (c) 160 mm free drop, no failure, voltage, and temperature change. .... 100
- Figure 55 Schematic illustration of the penetration test's experimental method. Experimental equipment, design and the definition of battery

|  |     |
|--|-----|
| numbers in this paper. ....  | 107 |
| Figure 56 Schematic of the TR propagation model. (a) The thermal equivalent method of a single battery and links among cells; (b) Node division method; (c) Schematic of the electric connections. ....  | 113 |
| Figure 57 Schematic illustration of the cylindrical surface contact resistance measurement. (a) Numerical experiment setup and calculation method of equivalent resistance; (b) Calculation results, the relationship between spacing and thermal resistance.....  | 114 |
| Figure 58 Typical results of experiments and comparison between experiment and simulation. (a) single battery TR; (b) 1×2 pack TR; (c) 3×3 pack TR. ....   | 119 |
| Figure 59 Typical results of the TR of a 20×20 ideal thermal contact pack and the estimation method of the total TR propagation time. (a) propagation direction and speed; (b) comparison between theoretical curve calculated by the propagation theory and numerical calculation curve; (c) estimation method for the situation in which the first TR is triggered inside; (d) estimation method for T shape packs; (e) propagation speeds at different packing angles. .... | 122 |
| Figure 60 Typical phenomena and mechanisms of TR propagation when thermal contact changes. (a) simulation results: 1×2 pack ( $\theta_c = 0.74$ W/K (or $d = 0$ mm) and $\theta_c = 2.94$ W/K (or $d_p = \sim 0.01$ mm)); (b) propagation front of pack at $\alpha=90^\circ$ under mode II; (c) propagation front of pack at $\alpha_p=60^\circ$ under mode II. ....   | 124 |
| Figure 61 Schematic of the coupling effect of battery spacing and ambient temperature on TR propagation speed. The value $\log(v)$ is used to indicate the TR propagation spatial speed. $v$ is the propagation spatial speed and $D$ is the diameter of the battery. ....   | 126 |
| Figure 62 TR propagations under conditions with random thermal contacts among batteries. The equivalent thermal transfer coefficients are set as random between 0 W/K to 2.7 W/K (a) $N-t$ curves and (b) their related possible propagation path.....   | 127 |
| Figure 63 Model setups of the battery model .....  | 142 |
| Figure 64 Boundary conditions of the thermal model .....   | 142 |

## NOMENCLATURE

| <b>Nomenclature</b> |   |                     |  |
|---------------------|---|---------------------|--|
| $Y, y$              | True value                                  | $X, x$              | Input argument vector                        |
| $\mathbf{u}$        | Displacement field                          | $\mathbf{F}_L$      | Deformation gradient                         |
| $\mathbf{F}_V$      | Body force                                  | $\mathbf{S}$        | Piola–Kirchhoff stress tensor                |
| $\varepsilon_l$     | volume fraction                             | $t_+$               | transfer data                                |
| $D_{eff}$           | modified diffusion coefficient              | $i_l$               | current density                              |
| $k_{eff}$           | modified electrical conductivity            | $\phi_l$            | potential of the electrolyte                 |
| $Y_p$               | Predicted value                             | $F$                 | Loading force                                |
| $F_{ISC}$           | Short circuit triggering force              | $\varepsilon$       | Strain                                       |
| $\varepsilon_{ij}$  | Strain component                            | $\varepsilon_i$     | Principle strain                             |
| $h_{ikllmn}$        | Tensor for description of discretized space | $C_{SVR}$           | Regularization parameter                     |
| $\gamma_{SVR}$      | Kernel coefficient for RBF                  | $\varepsilon_{SVR}$ | The epsilon-tube width for epsilon-SVR model |
| $SoC$               | State of charge                             | $\sigma$            | Stress                                       |
| $\sigma_{ij}$       | Stress component                            | $\sigma_i$          | Principle stress                             |
| $\sigma_{eq}$       | Equivalent stress                           | $w, b, \beta$       | Learnable parameters for SVR                 |
| $\zeta$             | Coefficient for penalizing the objective    | $\mu_g$             | Mean value                                   |
| $s$                 | Loading displacement                        | $\sigma_g^2$        | Variance                                     |
| $t$                 | Time  | $F1$                | F1 score                                     |
| $\Delta t_s$        | Short time interval                         | $\Delta t_1$        | Long time interval                           |
| $R_{short}$         | Short circuit resistance                    | $T$                 | Temperature                                  |
| $C_{rate}$          | Charge/discharge rate                       | $u, U$              | Voltage                                      |

|             |   |             |   |
|-------------|---|-------------|---|
| $P$         | Pressure  | $C_d$       | Discharge capacity  |
| $i, I$      | Current   | $I_{short}$ | Short circuit current   |
| $i_e$       | Current deviations  | $RA$        | Area resistance   |
| $u_e$       | Voltage deviations  | $\delta$    | Voltage change  |
| $C_p$       | Constant pressure thermal capacity  | $\rho$      | Material density  |
| $q$         | Heat flux   | $Q$         | Heat power  |
| $U_{ocv}$   | Open-circuit voltage  | $k$         | Thermal conductivity  |
| $Q_{short}$ | Short circuit joule heat  | $Q_{cell}$  | Heat produced by the cell during the discharging process                                      |
| $Q_{exo}$   | chemical reaction heat  | $Q_{rad}$   | Thermal radiation heat  |
| $Q_{joule}$ | Joule heat  | $Q_{conv}$  | Thermal convection heat   |
| $T_i$       | Jellyroll temperature   | $S_{cell}$  | Free surface area of cell   |
| $T_{si}$    | Shell temperature   | $h_{conv}$  | Convection heat dissipation coefficient   |
| $T_{amb}$   | Ambient temperature   | $T_{c,x}$   | Triggering temperature of reaction $x$  |
| $T_{TR}$    | Thermal runaway triggering temperature  | $h_t$       | Equivalent heat transfer coefficient  |
| $R_{ohm}$   | Ohm resistance  | $R_{short}$ | Equivalent resistance of short-circuit  |
| $Q_{trans}$ | Heat transfer between the cell and the fixture/ indenter  | $R_{ct}$    | Charge transfer resistance  |
| $S_t$       | Total contact area  | $c_{sei0}$  | Initial value of the dimensionless amount of lithium-containing metastable species in the SEI |
| $c_{sei}$   | Dimensionless amount of lithium-containing metastable species in the solid electrolyte interphase | $c_{a0}$    | Initial value of the dimensionless amount of lithium intercalated within carbon               |
| $c_a$       | Dimensionless amount of lithium intercalated within   | $c_e$       | Dimensionless concentration of electrolytes   |

|            |  |            |  |
|------------|--|------------|--|
|            | carbon   |            |  |
| $c_{cc}$   | Dimensionless amount of solid phase of current collector         | $c_{sep}$  | Dimensionless amount of solid phase of separator           |
| $c_{e0}$   | Initial value of the dimensionless concentration of electrolytes | $K_{s,g}$  | SEI generation constant                                    |
| $\alpha_c$ | Initial degree of conversion of cathode                          | $m_a$      | Mass density of anode                                      |
| $c_{s,g}$  | SEI generation rate  | $m_c$      | Mass density of cathode                                    |
| $c_{s,d}$  | SEI decomposition rate   | $m_e$      | Mass density of electrolyte                                |
| $\kappa_0$ | Initial electrical conductivity                                  | $z$        | Dimensionless measure of SEI thickness                     |
| $E$        | Young's modulus  | $z_0$      | Reference dimensionless measure of the SEI layer thickness |
| $S_{sei}$  | SEI decomposition area   | $\kappa$   | Electrical conductivity                                    |
| $S_e$      | Electrolyte decomposition area                                   | $\kappa_e$ | Electrical conductivity after melting                      |
| $S_{ae}$   | Anode-electrolyte reaction area                                  | $C_{loss}$ | Capacity loss  |
| $t_d$      | Discharging period during defect introduction                    | $S_m$      | Separator collapse area                                    |
| $d$        | Displacement   | $S_{ce}$   | Cathode-electrolyte reaction area                          |
| $\sigma_b$ | Stefan–Boltzmann constant  | $Q_d$      | Total released heat during defect introduction             |
| $T_s$      | Steady state temperature   | $L$        | Particle diameter  |
| $A_a$      | Frequency factor for anode decomposition                         | $V$        | Cell volume  |
| $A_c$      | Frequency factor for cathode decomposition                       | $\eta$     | Efficiency factor  |
| $A_{cc}$   | Frequency factor for electrochemical reactions                   | $R_g$      | Gas constant   |
| $A_s$      | Frequency factor for SEI decomposition                           | $E_a$      | Activation energy for anode decomposition                  |

|             |   |             |   |
|-------------|---|-------------|---|
| $A_e$       | Frequency factor for electrolyte decomposition                    | $E_c$       | Activation energy for cathode decomposition     |
| $A_{cc}$    | Frequency factor for collector melting                            | $E_{ec}$    | Activation energy for short circuit             |
| $A_{sep}$   | Frequency factor for separator decomposition                      | $E_s$       | Activation energy for SEI decomposition         |
| $C$         | Capacity of battery   | $E_e$       | Activation energy for electrolyte decomposition |
| $\alpha_c$  | Initial degree of conversion of cathode                           | $E_{cc}$    | Activation energy for collector melting         |
| $Q_a$       | Anode decomposition heat  | $h_a$       | Enthalpy of anode decomposition reaction        |
| $Q_s$       | SEI decomposition heat  | $h_c$       | Enthalpy of cathode decomposition reaction      |
| $Q_{ec}$    | Thermal runaway short circuit heat                                | $h_{ec}$    | Heat released by short-circuit                  |
| $Q_c$       | Cathode decomposition heat  | $h_s$       | Enthalpy of SEI decomposition reaction          |
| $Q_e$       | Electrolyte decomposition heat                                    | $h_e$       | Enthalpy of electrolyte decomposition reaction  |
| $V_{cell}$  | Volume of cell  | $\rho_{jr}$ | Density of jellyroll                            |
| $R_r$       | Internal resistance of battery                                    | $\rho_s$    | Density of shell                                |
| $R_{inner}$ | Inner radius of jellyroll   | $c_{p,jr}$  | Specific heat capacity of jellyroll             |
| $R_{outer}$ | Outer radius of jellyroll   | $c_{p,s}$   | Specific heat capacity of shell                 |
| $\theta_p$  | Equivalent thermal resistance between battery shell and jellyroll | $t_{cell}$  | Thickness of battery shell                      |
| $\theta_c$  | Equivalent thermal resistance between two batteries               | $l_{cell}$  | Length of battery                               |
| $K_c$       | Equivalent thermal transfer coefficient between two batteries     | $\alpha_p$  | Packing angle                                   |
| $d_p$       | Cell spacing within pack  | $N_{TR}$    | Number of thermal runaway triggered cells       |
| $\rho_p$    | Packing density   | $v_{TR}$    | Thermal runaway propagation speed               |

|                   |  |       |   |
|-------------------|--|-------|---|
| $D_{\text{cell}}$ | Diameter of cell                             | $B_p$ | Number of batteries in the width directions |
| $H_p$             | Number of batteries in the length directions | $L_n$ | Dimensionless distance                      |
| $v_n$             | Dimensionless propagation spatial speed      |       |   |

## CHAPTER 1 INTRODUCTION

### 1.1 Background

LIBs are playing increasingly important roles to promote the mobility of current society. The energy density of the LIBs has been improved significantly, along with superior cyclability and low cost. However, as the increasing number of safety incidents, such as fire/explosion, of LIBs become more frequent and violent, battery safety becomes an important factor hindering people from adopting LIBs as power sources in various scenarios. Safety issues of LIBs are usually caused by additional heat sources produced by an ISC that can be caused by accidental mechanical abuses<sup>1-5</sup>, electrical abuses (overcharging or over-discharging)<sup>6,7</sup>, and thermal abuses (overheating)<sup>8,9</sup>. The generated heat and the increased temperature would lead to several complicated physiochemical changes, such as decomposition reactions, phase changes<sup>10,11</sup>, and fatal fire/explosion consequences of the batteries<sup>12-15</sup>. Therefore, an in-depth understanding of the complexity of the multiphysics nature of LIB safety behaviors upon mechanical abusive loading poses a grand challenge. Furthermore, understanding the fundamental mechanism would further unlock new opportunities in battery design, application, and monitoring.

### 1.2 Literature review

#### 1.2.1 Multiphysics behaviors of lithium-ion batteries

Generally, safety issues of LIBs are usually initiated from an ISC<sup>16-20</sup>. The short circuit generates heat and increases the temperature, which triggers future related

decomposition reactions (electrodes and electrolyte) and the phase changes (separators, collectors)<sup>10, 11</sup>. These complicated physiochemical changes finally lead to thermal runaway (TR) and fatal fire/explosion consequences of the batteries<sup>12-15</sup> (Fig.1). The complex nature is caused by the coupling effects of mechanics, thermology, and electrochemistry for batteries upon abusive loadings.

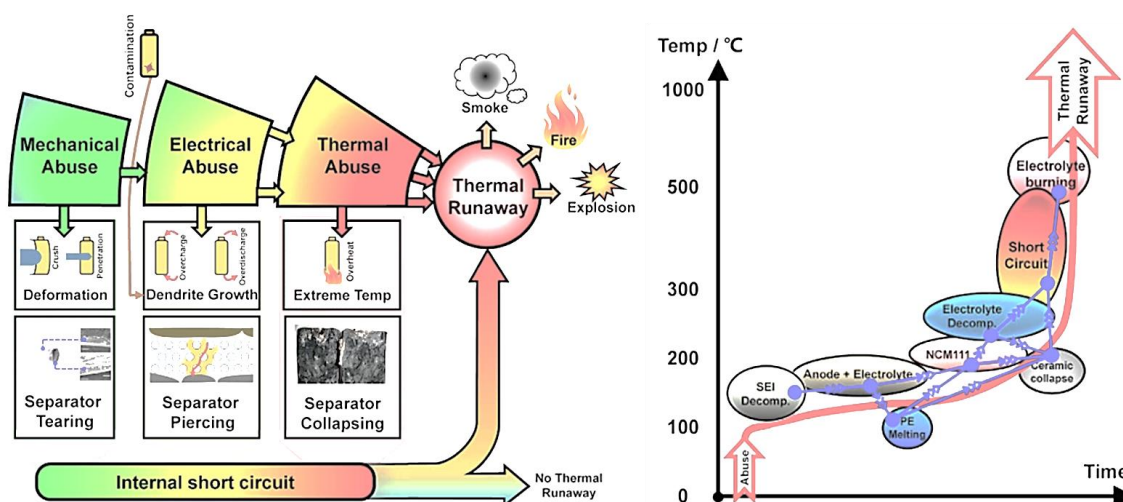


Figure 1 Multiphysics behaviors of safety issues of LIBs<sup>15</sup>.

Experimental characterization of battery safety is an essential way to understand the underlying nature of the multiphysics behavior of batteries<sup>17, 21-23</sup>. Overcharge and large-current (rate) charge characterization<sup>24-26</sup> have been used at the cell level to reveal the safety behavior upon electrochemical abusive loadings. External heat has also been used to investigate the safety behavior upon thermal abusive loadings<sup>12, 18</sup>. Among those methods, applying mechanical abusive loadings is the most reliable and controllable way to trigger ISC, including compression<sup>5, 27-34</sup>, indentation<sup>1, 3, 19, 35-39</sup>, bending<sup>5, 28, 30, 32</sup>, nail penetration<sup>40-43</sup> and dynamic impact<sup>28, 34</sup>). The mechanical, thermal, and electrochemical

behaviors of the batteries were characterized by recorded loading forces, open-circuit voltages (OCV), and surface temperatures in time history <sup>29</sup>.

Observation and measurement of the ISC triggering tests indicate that ISC and TR are two milestone events in battery safety issues <sup>6, 44, 45</sup> (Fig. 2). ISC is determined by the voltage drop due to the consumption of the battery capacity by joule heat <sup>17</sup>. After the triggering of ISC, the produced joule heat would provide sufficient energy for the triggering of the thermal runaway in some cases, which may release tremendous heat, toxic gases and finally cause the subsequent fire/explosion accidents <sup>10, 19, 46-48</sup>. Temperature measurements during the experiments indicate a possible violent TR following an ISC <sup>49-51</sup>. The quantitative relations among mechanical factors <sup>52, 53</sup> and electrochemical factors (*e.g.*, state of charge (SOC) <sup>33, 54-56</sup> and state of health (SOH) <sup>33, 56</sup>) were investigated to elucidate the phenomenological coupling effects of mechanical and electrochemical fields.

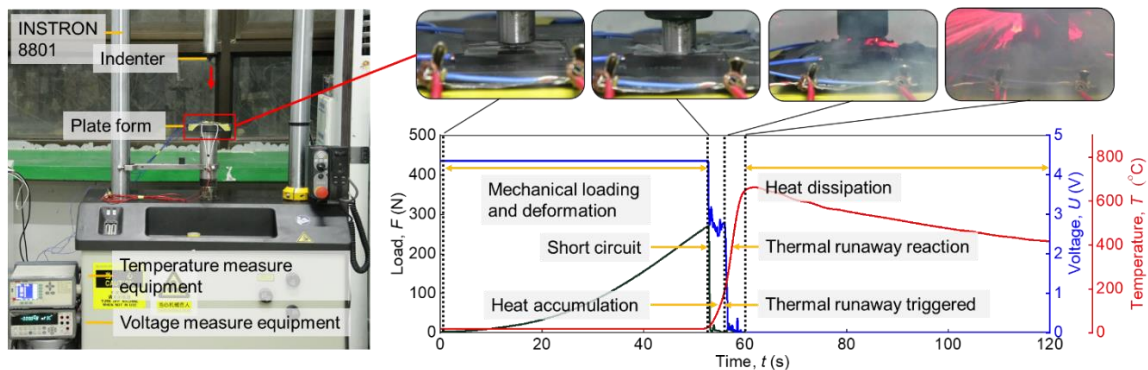


Figure 2 Typical results of battery mechanical abusive loading test <sup>19</sup>.

### 1.2.2 Stress-induced internal short circuit

Plenty of experimental methods have been developed to trigger the ISC. For the thermal-triggered method, there is a phase change material method <sup>57</sup>, and a memory alloy

method<sup>58</sup>. For the electric-trigger method, fast charging/discharge, overcharging/discharging, and cycling can cause ISC. To control the ISC position, a metallic particle is retrofitted into the battery<sup>59</sup>. External mechanical abusive loading is one of the most common triggers of ISC<sup>39,60</sup>, including penetration<sup>61</sup>, pre-holed separator method<sup>62,63</sup> and internal particle<sup>64</sup> are all popular ISC triggers methods.

In mechanical abusive experiments, voltage drop and temperature rise are two characteristic phenomena that occur when a cell is short-circuited<sup>4,45,48</sup>. As such, by monitoring the voltage profile and temperature distribution field, ISC's can be captured easily<sup>29,30,65</sup>. Based on the mechanical tests of batteries, Sahraei et al. realized the prediction of onset of ISC based on FE simulation and pointed out that the point of failure of the material in tension is correspondent to the point of short-circuit<sup>66</sup>. Greve et al. then proposed a Mohre-Coulomb (MC) ISC/fracture criterion for cylindrical LIB<sup>5</sup> (Fig. 3). The abusive loading tests can indicate the ISC point under various loading conditions. The corresponding cases were modeled to obtain the complete stress-strain distribution in the cell. Based on the ISC point and the stress-strain distribution, the stress-/strain-based ISC criterion was generated. To be more general, a unified strength theory (UST) ISC criterion is also established<sup>28</sup> (Fig. 3). Those criteria are established for a homogenous model which simplifies the layered battery structure into a homogenized solid. Further studies, using advanced techniques (*e.g.*, CT (computed tomography) scanning) and visualizing the rapid failure mechanism of ISC inside the cell<sup>27,67,68</sup>, indicate that the deformation or fracture

of the separator is the main reason that leads to stress-induced ISC<sup>16</sup>. Thus, Wang and Yuan et al. established strain-based ISC criteria for separators based on a detailed battery model which mode the battery components in detail, respectively<sup>31,32</sup> (Fig. 3). Those criteria are useful for engineers and serve as an important mechanical-electric coupling relationship in multiphysics modeling.

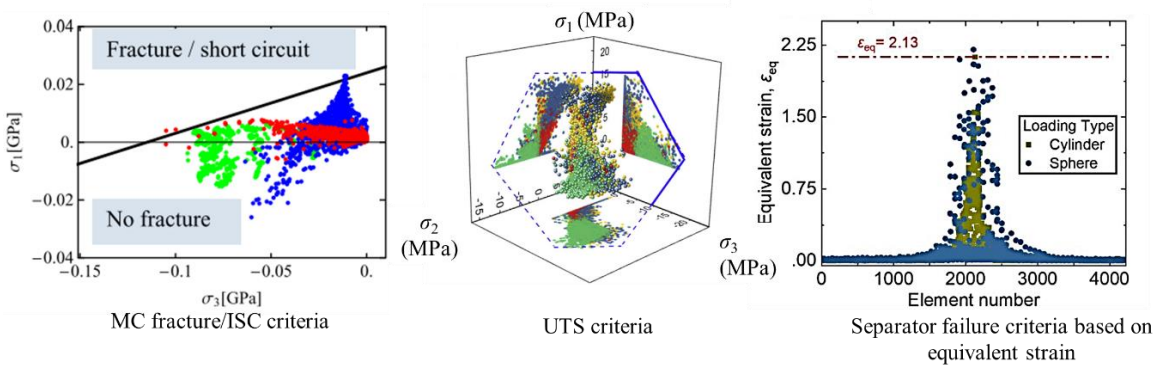


Figure 3 Failure criteria established based on simulation and experimental data<sup>5, 31, 32</sup>.

### 1.2.3 Thermal runaway triggering and propagation

TR is one of the most severe consequences that could cause fatality incidents<sup>10, 15</sup>. The Joule heat produced by the ISC process provides the initial energy before the temperature reaches the threshold value of TR. TR is one of the most serious consequences of ISC. Generally, TR occurs when an exothermic reaction develops out of control [18]. When the temperature is high enough, the reaction heat production rate will be triggered and becomes much higher than the heat dissipation rate, and the temperature increases irreversibly (Fig. 4). The mechanisms of thermal reactions are continually studied and gradually unraveled. Based on the theories of thermal reactions, many TR models have been established based on theoretical equations and finite element (FE) computational techniques. The models are

mainly based on Arrhenius formulations and provide related activation energies and the enthalpies of various decomposition reactions for the compounds <sup>69, 70</sup>. With the help of capable equipment, *e.g.*, high-speed X-ray imaging, many details of the mechanisms of thermal runaway inside cells were further revealed <sup>71, 72</sup>.

When the TR of the first battery of a battery pack is triggered, the neighboring batteries will be heated and probably triggered to yield runaway reactions in some specific scenarios <sup>8</sup>. This phenomenon, called TR propagation, can lead to catastrophic hazards within battery packs <sup>9, 73</sup>. To determine the behavior and mechanisms underlying this phenomenon, several theoretical and numerical experiments were conducted <sup>12, 74, 75</sup> (Fig. 4). Numerous experiments show that thermal conduction, thermal radiation, and thermal accumulation during fire heating are three important factors for TR propagation, no matter for cylindrical cells <sup>76</sup>, prismatic cells <sup>77, 78</sup>, or pouch cells <sup>13</sup>. Among these factors, thermal contact <sup>79</sup>, interspacing and appropriate fire retardant materials between the cells are required to hinder fire propagation <sup>80, 81</sup>.

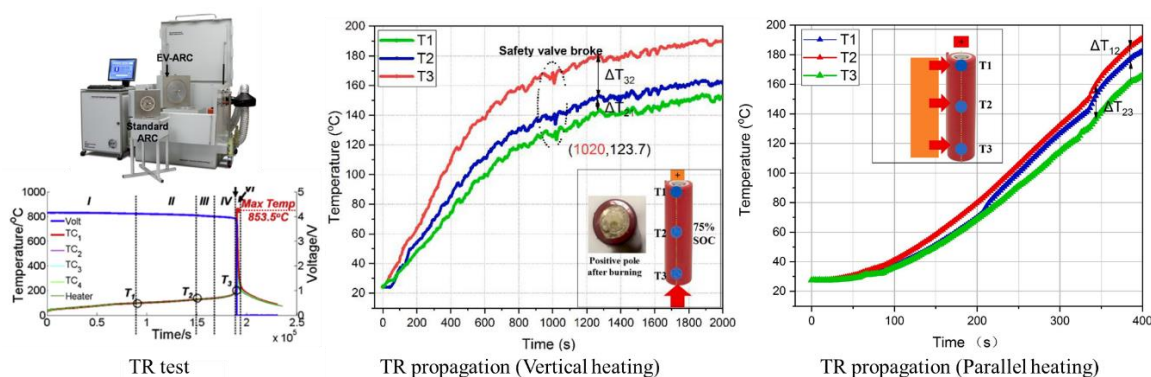


Figure 4 Experimental results of TR and TR propagation test <sup>8, 11</sup>.

#### 1.2.4 Safety risk evaluation based on multiphysics modeling

Considering the safety issues as well as time- and cost-effectiveness, multiphysics FE models of batteries were established and validated to provide a reasonable description of force responses, deformation, stress field, and strain field <sup>4, 5, 21, 30, 32, 82</sup>.

In the electrochemical field, the typical 1D battery model developed in recent years <sup>83-86</sup> has been able to satisfactorily predict battery electrochemical behavior. To simplify the model, an equivalent circuit is usually used to simulate the ISC. The ISC criteria are used to bridge the electrochemical model and the mechanical model. Besides, the Arrhenius equation has been mainly used to describe the decomposition reaction rate for the TR <sup>18, 48</sup>. In the thermal field, heat sources were extracted from the battery electrochemical heat, short-circuit joule heat, and TR reaction heat <sup>43, 87, 88</sup> while the heat dissipation consists of heat radiation, convection, and battery venting. In the mechanical field, both homogeneous <sup>5, 89, 90</sup> and detail models <sup>32, 91, 92</sup> were developed. Possible improvements, such as the introduction of anisotropy, strain rate effects, and SoC effects, were also achieved <sup>30, 93</sup>.

Based on the battery electrochemical model and electrical/ thermal equations, Guo et al. developed a multiphysics model for a Li-ion battery module that includes three cells connected in series. The model can predict the 3D profiles of the electrical potentials and temperature in the battery <sup>94</sup>. Chiu et al. then considered short circuit and TR modeling via artificially giving a potential value at the positive end of the battery in their model <sup>43</sup>. The model can accurately describe the voltage during ISC and temperature during TR. To

establish the relationship between structure fracture and ISC in multiphysics modeling, Zhang et al. further involve a representative-sandwich (RS) based mechanical model. Their model uses the maximum tensile failure criterion and calculates the current flow across the failure component layers<sup>37, 95</sup>. Based on that progress, Liu et al. proposed a fully coupled multiphysics computational framework model in COMSOL to describe the complete process from initial deformation to the final TR<sup>48</sup> (Fig. 5). Furthermore, a more detailed FE geometry modeling<sup>1, 19</sup> was developed, and further extended to the active particle level<sup>96</sup>. However, due to the computational intensity, the fully coupled multiphysics framework cannot directly be applied to large-scale simulations, such as module- or pack-level simulations<sup>21</sup>. Thus, Deng et al. applied the composite “Tshell” elements of LS-DYNA in the coupled model to reduce the number of elements and, therefore, computational time considerably<sup>97</sup>. Case studies indicated that the composite “Tshell” elements can achieve comparable results in multiple solvers with much less time<sup>97, 98</sup>.

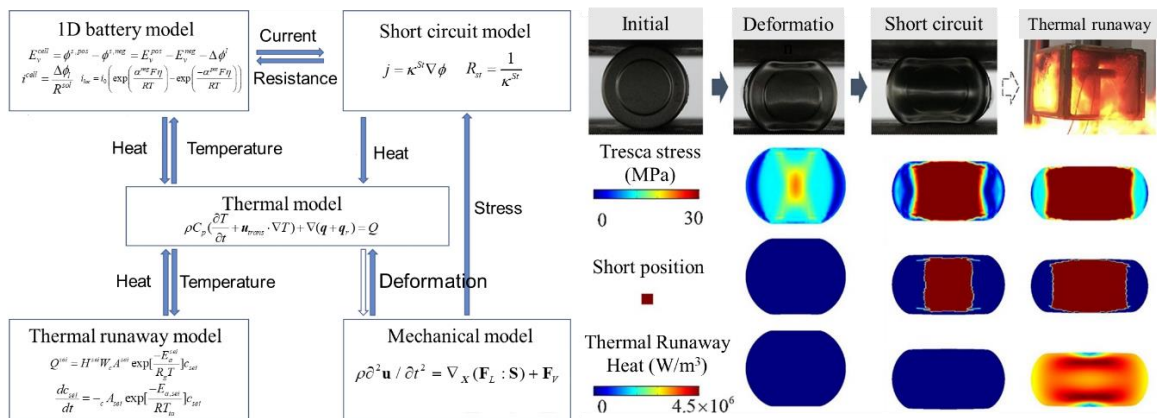


Figure 5 Multiphysics modeling framework of LIBs<sup>48</sup>.

To enhance the efficiency and the accuracy of the FE model, the emerging machine

learning (ML) methodology was used to assist the battery safety evaluation and design<sup>99-104</sup>. Recently, Li et al. demonstrated a data-driven safety envelope predicted by several typical classifications and regression ML algorithms, including Artificial Neural Networks (ANN) and Support Vector Machines (SVM)<sup>105</sup>. The training samples were generated from a detailed FE model developed based on several material tests and cell tests (Fig. 6). This method overcomes the limitation of computational sources. Apart from the prediction of ISC based on mechanical features, Naha et al. develop an online ISC detection using a Random Forests (RF) classifier<sup>99</sup>. The training features are obtained from battery current and voltage data. Attia et al. and Severson et al. developed data-driven models that can accurately predict the cycle life using early-cycle data<sup>101, 106</sup>. The good performance stemmed from their understanding of the capacity degradation mechanism of the selected cells<sup>101, 106</sup>. The models greatly reduced the calculation and experimental time as well.

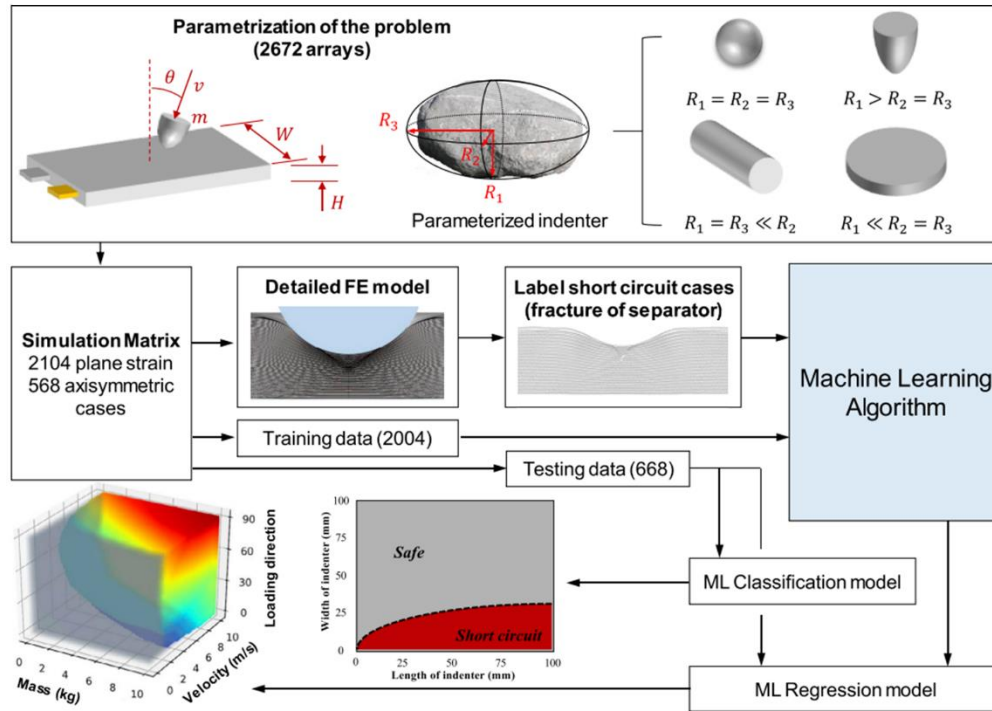


Figure 6 Evaluation of battery safety under mechanical loading based on ML methods.

### 1.3 Challenges and motivation

As mentioned above, several experimental, theoretical, and numerical studies have provided us with some understanding of the multiphysics behaviors of LIBs. Multiphysics models of batteries were established and validated to provide a reasonable description of force responses, deformation, stress field, and strain field<sup>4, 5, 21, 30, 32, 82</sup>. In terms of short-circuit triggering prediction. Those studies proposed either strain-<sup>31</sup> or stress-based<sup>32, 82</sup> failure criteria to indicate the boundary of ISC for a cell upon external mechanical loading. However, the results are still not satisfactory due to: (1) the limited generalization of the model; and (2) the stochastic nature of the complicated battery cell in material and electrochemical properties as well as possible assembling defects. In terms of safety risk evaluation, traditional methods estimation usually relies on empirical models and aims to

detect short circuits in the initial stage <sup>107</sup>. Commonly selected indicators are directly measurable variables <sup>108</sup>, *e.g.*, current, voltage, and temperature, as well as calculated variables <sup>65,109</sup>, *e.g.*, internal resistance and level of battery consistency (for battery pack)<sup>110</sup>. However, short circuits may happen in a variety of scenarios. The value of short circuit resistance also has a very large range (from hard ISC with TR to soft ISC which only lead to minor defect <sup>1,19</sup>). Single characteristics or thresholds cannot capture all short circuit behaviors and consequences of short circuits are not always high-risk issues <sup>19</sup>. Thus, in my thesis work, the very fundamental issues, including ISC, TR, TR propagation, and defect (produced by specific external loadings), will be studied based on multiphysics modeling and experiment. Furthermore, the related safety risk will be defined, and the corresponding evaluation methods will be developed based on experimental data, numerical computation, and data-driven methodology combined manner.

#### 1.4 Chapter arrangement

Chapter 2 introduces some basic conceptions, definitions, and multiphysics modeling frameworks used in this dissertation. Chapter 3 presents the development of the ISC risk prediction model that can accurately predict the safety risk of lithium-ion batteries induced by mechanical stress. Chapter 4 discusses the establishment of the battery safety risk classification model that can accurately and quickly predict the safety risk level of the LIB cells during the charging/ discharging. Chapter 5 focuses on the safety issues of defective cells, especially aiming at the electrochemical performance, thermal safety, and mechanical

integrity of the battery. Chapter 6 provides an efficient yet accurate pack level TR model that is constructed based on theoretical analysis. Chapter 7 summarizes the conclusions of this dissertation.

## CHAPTER 2 MULTIPHYSICS BATTERY SAFETY BEHAVIORS

In this chapter, multiphysics behaviors and mechanisms of two milestone events, ISC and TR, are discussed, some basic conceptions, definitions, and the multiphysics modeling frameworks used to describe cells in this dissertation are provided. According to safety behaviors and corresponding mechanisms, two kinds of risks, including ISC triggering risk and safety risk level, are defined to evaluate the safety risk of the cell. The ISC risk is defined as the possibility of the triggering of the ISC under a given mechanically loading condition. Further, four representative safety risk levels are defined. Finally, a general battery multiphysics modeling framework is provided. The sub-models and corresponding coupling relationships are also presented.

### 2.1 ISC risk

ISC happens when the anode contacts with the cathode. The direct cause is the deformation or disfunction of the separator<sup>16</sup>. Abusive conditions, such as mechanical loading, over-heat, and over-charge may directly trigger the ISC for cell<sup>45</sup>. Here we focus on mechanically triggered ISC. In mechanical abusive experiments, short circuit triggering can be recognized by voltage drop and temperature rise<sup>29, 30, 65</sup>. Considering nonlinearity, complexity, and uncertainty of the safety behaviors of LIBs, the safety risk  $Y$  is defined as the probability of the triggering of ISC. According to experimental results<sup>111</sup>, ISC is triggered when the loading force reaches a specific value (Fig. 7), defined as the short circuit force  $F_{ISC}$  here.  $F_{ISC}$  distribute within a value range. Thus, we suppose  $F_{ISC}$

follows a one-dimensional Gauss distribution,  $F_{ISC} \sim N(\mu_g, \sigma_g^2)$ . The two parameters, i.e., the mean ISC force  $\mu_g$  and the variance  $\sigma_g^2$ , of the used gaussian possibility density distribution function, are calculated from a group of measured ISC forces:

$$\mu_g = \frac{1}{n} \sum_{i=1}^n F_{ISC,i}, \quad (1)$$

and variance  $\sigma^2$  is calculated by

$$\sigma_g^2 = \frac{1}{n} \sum_{i=1}^n (F_{ISC,i} - \mu)^2, \quad (2)$$

Then, the ISC triggering possibility under each loading force can be obtained by taking the integral of probability density function:

$$Y = k(F) = P(F_{ISC} < F) = \int_0^F \frac{1}{\sigma_g \sqrt{2\pi}} e^{-\frac{(F-\mu_g)^2}{2\sigma_g^2}} dF. \quad (3)$$

We also have the mapping  $g : s \rightarrow F$ , where  $s$  is loading displacement. Thus, safety risk can be expressed by the function of  $s$ ,

$$Y(s) = k(g(s)) = \int_0^{g(s)} \frac{1}{\sigma_g \sqrt{2\pi}} e^{-\frac{(g(s)-\mu_g)^2}{2\sigma_g^2}} g'(s) ds. \quad (4)$$

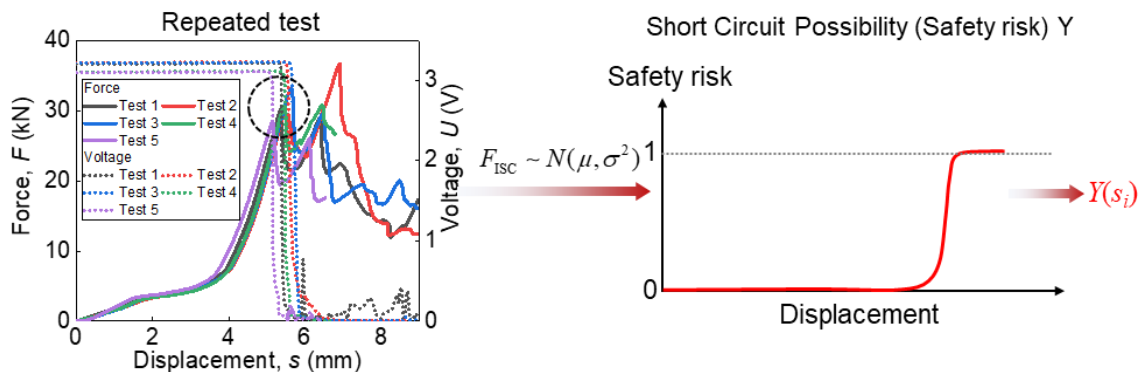


Figure 7 Achievement of the safety risk.

## 2.2 Safety risk levels

When ISC is triggered, the joule will provide the initial energy for the triggering of the exothermic reactions or phase changes. When the temperature is high enough, the related exothermic reactions will be triggered. The reactions will produce heat and lead to further temperature increases. When the heat production rate becomes much higher than the heat dissipation rate, the temperature increases irreversibly, which means TR occurs (case 1 in Figure 8)<sup>10</sup>. When the ISC joule could not provide enough initial energy, TR will not be triggered (cases 2 in Figure 8a)<sup>19</sup>. However, for some cases, such as pouch cells with medium SOC under small mechanical indentation, the voltage can recover almost to its original value in a short period with relatively minor voltage drops and small temperature rise (cases 3 in Figure 8a)<sup>19</sup>. The recovered cells are a kind of defective cell that can work as normal (Figure 8b)<sup>1</sup>. Those complicated evolution processes are mainly determined by cells' electrochemical status (*e.g.*, SOC), triggering conditions (*e.g.*, contact mode and contact area), and initial conditions (*e.g.*, temperature). Thus, the safety risk is hard to be quantized or predict by any single indicator. However, according to the safety risk level of different types of behaviors after short circuit triggering, cells' status can be classified. Here four levels are defined: (1) Normal cells (L0): the cell is intact and works normally; (2) Defective cells (L1): the cell is shorted before, but the short circuit resistance  $R_{\text{short}}$  is large enough ( $10^1 \sim 10^3 \Omega$ ) so that it still works similarly as normal with a minor short circuit or current leakage under cycling conditions; (3) Shorted cells without possible TR risk (L2): the cell is shorted (no longer work normally), but the TR will never happen due to its

limited heat generation under the current boundary conditions; (4) Shorted cells with possible TR risk (L3): the cell is shorted, and the TR will happen under the current boundary conditions in the future. Two typical scenarios can cause/exhibit battery safety issues, i.e., cycling test (long-term) and abusive testing (short-term).

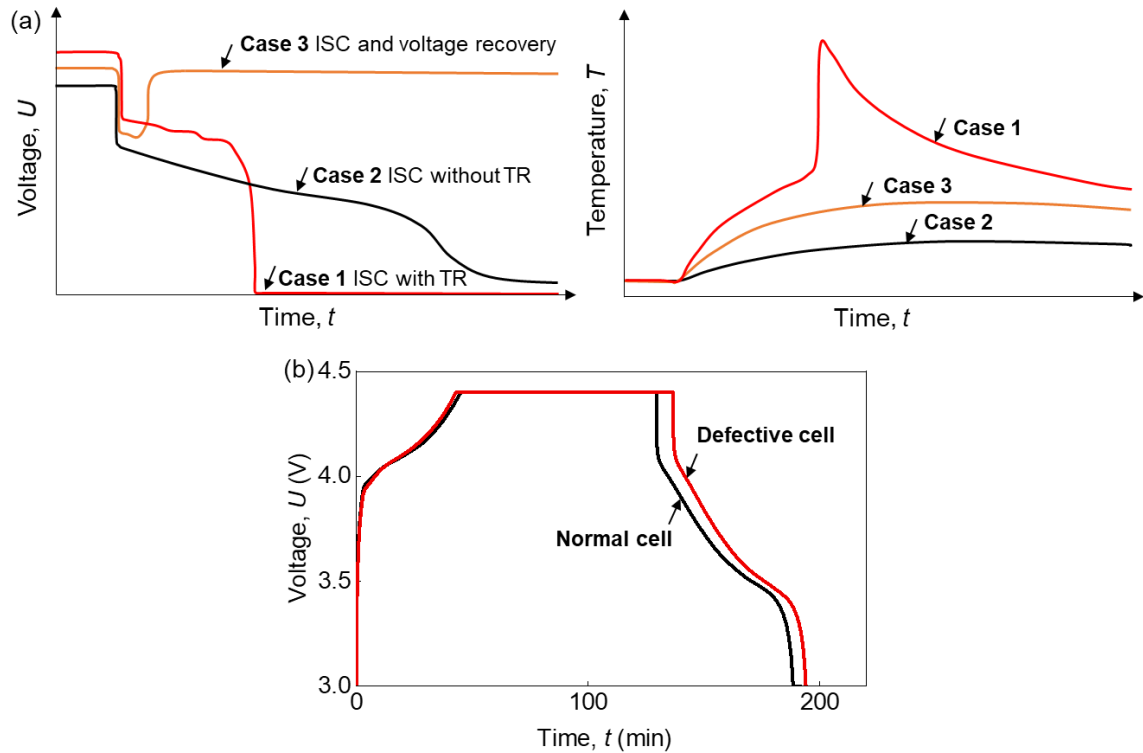


Figure 8 Different short circuit evolution processes. (a) voltage/ temperature behaviors of three common evolution processes. (b) comparison of voltage behaviors between normal cells and defective cells.

### 2.3 Multiphysics modeling framework

The multiphysics modeling framework consists of sub-models and coupling relationships among them. The sub-models and coupling relationships can be modified according to actual need and boundary conditions.

#### 2.3.1 Sub-models

The modeling framework has five sub-models (Fig. 9):

(1) Mechanical model: solve the deformation, stress, strain state with cell's material properties and boundary conditions. Newton's second law is used:

$$\rho \frac{\partial^2 \mathbf{u}}{\partial t^2} = \nabla_{\mathbf{x}} (\mathbf{F}_L : \mathbf{S}) + \mathbf{F}_V, \quad (5)$$

where  $\mathbf{X}$  is the material coordinate.

(2) Battery electrochemical model: solves the voltage and short circuit current of the cell based on thermal and short circuit conditions. The classical 1D battery model was first established by Newman et al.<sup>112</sup>. In this model, the mass balance and charge balance of electrolytes is expressed as<sup>48</sup>

$$\begin{cases} \varepsilon_l \frac{\partial c_l}{\partial t} = -D_{eff} \nabla c_l + \frac{i_l t_+}{F} \\ i_l = -k_{eff} \nabla \phi_l + \frac{2k_{eff} R_g T}{F} \left(1 + \frac{d(\ln(f))}{d(\ln(c_l))}\right) (1 - t_+) \nabla \ln(c_l) \end{cases}, \quad (6)$$

where  $1 + d\ln f / d\ln c_l$  is the molar activity coefficient;  $R_g$  is the gas constant, and  $F$  is Faraday's constant. The 1D battery model utilizes half of the thickness of the cathode and anode, as well as the entire thickness of the separator. Depending on the situation, a 2-D or 3-D model can also be built<sup>98</sup>.

(3) Short circuit model: simulates the short circuit and corresponding heat generation process. The equivalent circuits before and after the short circuit are shown in Fig. 8. The voltage and current are provided by the battery model. According to Ohm's law, the short circuit current is

$$I_{short} = \frac{U_{cell}}{R_{short} + R_0}, \quad (7)$$

According to Joule's law, the short circuit heat is

$$Q_{short} = I_{short}^2 R_{short}, \quad (8)$$

(4) Heat transfer model: solves thermal field based on initial conditions, boundary conditions, and heat sources from battery model and short circuit model. The dominant equation is:

$$\rho C_p \frac{\partial T}{\partial t} + \nabla \cdot \mathbf{q} = Q, \quad (9)$$

where  $\rho$  is the material density,  $C_p$  is the constant pressure thermal capacity,  $T$  is temperature,  $Q$  is the total heat power, and  $\mathbf{q}$  is the heat flux, that can be written as

$$\mathbf{q} = -k \nabla T, \quad (10)$$

where  $k$  is the thermal conductivity.

The heat sources  $Q$  consist of heat from the battery model  $Q_{cell}$ , joule heat from the short circuit model  $Q_{short}$ , and TR reaction heat from the TR model. Natural convection in the free surface  $Q_{conv}$  and heat transfer between the cell and fixtures  $Q_{trans}$  can also be considered. Thus, heat power  $Q$  equals to

$$Q = Q_{short} + Q_{cell} + Q_{conv} + Q_{trans}, \quad (11)$$

where  $Q_{conv}$  equals to:

$$Q_{conv} = S_c h_{conv} (T - T_{amb}), \quad (12)$$

where  $S_c$  is the free surface area,  $T_{amb}$  is the ambient temperature,  $h_{conv}$  thermal convection coefficient.  $Q_{trans}$  can be written as:

$$Q_{trans} = S_t h_t (T - T_{amb}), \quad (13)$$

where  $S_i$  is the total contact area,  $h_i$  is an equivalent coefficient.

(5) Thermal runaway model: simulates thermal runaway triggering and its heat generation process. In the TR model. A group of Arrhenius equations was used to describe the reaction rates of the decomposition of the cell constituents<sup>75</sup>:

$$\left\{ \begin{array}{l} c_x = c_{x,0} - \int_0^t \frac{dc_x}{dt} dt \\ \frac{dc_x}{dt} = \frac{dc_{x,d}}{dt} - \frac{dc_{x,g}}{dt} \\ \frac{dc_{x,d}}{dt} = A_x c_x^{n_{x,1}} (1 - c_x)^{n_{x,2}} \exp\left(-\frac{E_{a,x}}{RT}\right) (T > T_{c,x}) \end{array} \right. , \quad (14)$$

where x represents different reactions including SEI decomposition, the reaction between cathode and electrolyte, electrolyte decomposition, the reaction between anode and electrolyte, separator decomposition, the intense ISC caused by separator collapse and direct contact between anode and cathode. The exothermic reaction heater source is calculated by<sup>18, 88</sup>:

$$\left\{ \begin{array}{l} \frac{dQ_x}{dt} = h_x m_x \frac{dc_x}{dt} (T > T_{c,x}) \\ \frac{dQ}{dt} = \sum \frac{dQ_x}{dt} \end{array} \right. , \quad (15)$$

where  $h_x$  is the reaction enthalpy,  $m_x$  is the mass density,  $T_{c,x}$  is triggering temperature.

### 2.3.2 Coupling relationships

(1) Electro-mechanical coupling (relationship 1 in Figure 9)

The mechanical model and electrochemical model are coupled by the ISC criteria.

The ISC criteria are the critical stress or strain state of the cell when the ISC is triggered. At present, three types of ISC criteria (for homogeneous model) are available based on the stress, i.e., maximum principal stress criteria, Mohr-Coulomb criteria, and unified strength criteria <sup>45</sup>. The short circuit resistance can be regarded as a function of the stress/ strain state. It is generally set as an empirical value or an empirical curve. Then, the short circuit current can be calculated by the electrochemical model.

(2) Electrical relationship (relationship 2 in Figure 9)

The electrochemical model transfer cell voltage to the short circuit model. The short circuit model calculate the short circuit current based on Ohm's Law and return short circuit current to the electrochemical model

(3) Thermo-mechanical coupling (relationship 3 in Figure 9)

The mechanical model provides the thermal model with deformed geometry. And temperature field also influences material properties used in the mechanical model. However, thermal effects on material properties are usually ignored in multiphysics modeling due to its high computational cost.

(2) Electro-thermal coupling (relationships 4 and 5 in Figure 9)

The electrochemical model and short circuit model provide the thermal model heat sources. The heat generation includes joules heat of the resistance of current collector and short circuit resistance, produced reaction, polarization, and irreversible heat <sup>19</sup>. The heat transfer model returns temperature to the two models.

## (4) Thermal relationship (relationship 6 in Figure 9)

The thermal runaway model obtains the temperature field from the heat transfer model and calculates the reaction rates of the related exothermic reactions and returns the heat generation rate to the heat transfer model.

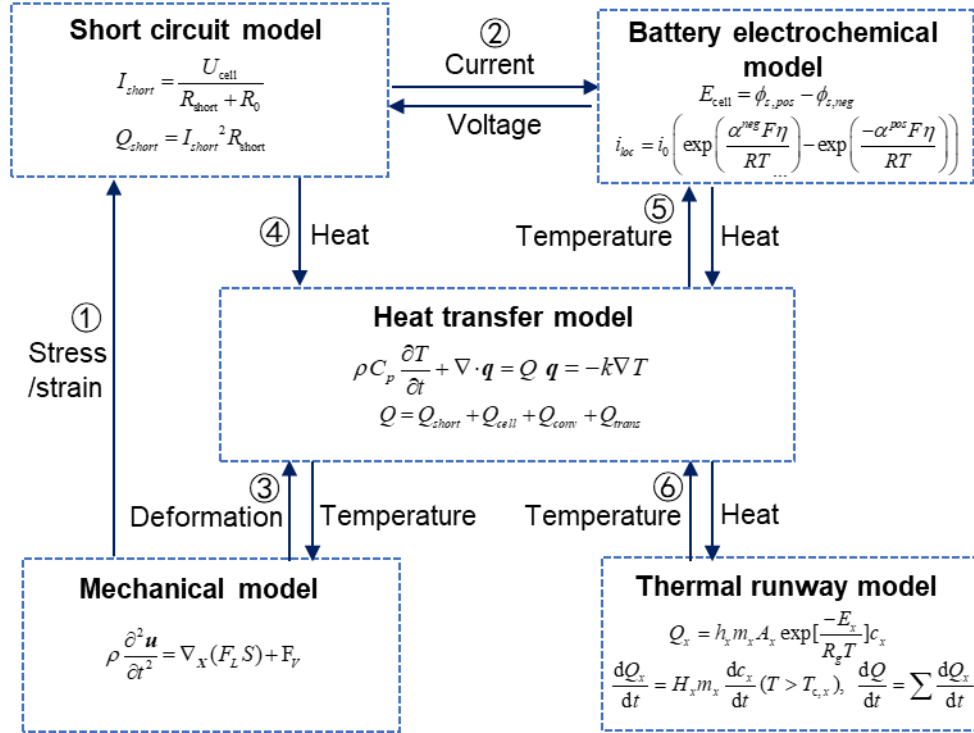


Figure 9 Framework of the multiphysics modeling.

## CHAPTER 3 INTERNAL SHORT CIRCUIT RISK UPON MECHANICAL ABUSIVE LOADING

In this chapter, we experimentally investigate the ISC triggering behavior, first define ISC risk induced by mechanical stress, and develop data-driven models that can accurately predict the ISC risk of the cell. A numerical computational model based on the RVE perspective was constructed to accurately describe the mechanical behavior and achieve the strain states under different loading conditions. Based on the validated FE model and experimental statistics, we generate a dataset ranging from 0% SOC to 60% SOC. SVR with Radial Basis Function (RBF) kernel is used to predict the ISC risk based on the strain state. The safety risk prediction high-level performance of the SVR predictors is indicated by various testing cases and scenarios.

### 3.1 Methods

#### 3.1.1 Mechanical loading tests

The quasi-static mechanical tests of the batteries were carried out with a SUNS material testing system with a 200-kN capacity (Fig. 10). Various platens and anvils were used to realize different loading conditions, such as platen for compression, 5 mm cylinder indenter, and different sizes of spheres (1, 1.5, 2, 2.5, 20 mm in diameter) for indentation test, and two 5 mm cylinder supporters for the bending test. Samples were placed on the corresponding supporter and applied a 100 N-preload to eliminate the possible gap between the sample and indenter. The loading speed was set as 5 mm/min for cylindrical cells and

0.5 mm/min for stacked-layer samples and pouch cells. The open-circuit voltage of the battery samples were simultaneously measured by A 34970 Agilent digital multimeter. The triggering of ISC was judged by the voltage signal (voltage decreasing). To improve the data quality, we conducted a large amount of LIB mechanical loading tests (13 scenarios, 75 tests for cylindrical cells; 6 scenarios, 30 tests for pouch cells) (Table 1). Thus, the experimental results cover the strain states to the largest extent.

Table 1 Summary of the experimental setup.

| Cell types       | Sample types   | Group number | Loading     | Size or position                   | SOC                      | Loading speed |          |     |
|------------------|----------------|--------------|-------------|------------------------------------|--------------------------|---------------|----------|-----|
| Cylindrical cell | Stacked-sample | 1            | Indentation | 5mm cylinder radial direction      | 0%                       | 0.5 mm/min    |          |     |
|                  |                | 2            |             | 6mm cylinder axial direction       | 0%                       |               |          |     |
|                  |                | 3            | Compression | 0% (battery length)-offset, radial | 0%                       |               |          |     |
|                  |                | 4            |             | 0%-offset, radial                  | 60%                      |               |          |     |
|                  |                | 5            |             | 50%-offset, radial                 | 0%                       |               |          |     |
|                  |                | 6            |             | 50%-offset, radial                 | 60%                      |               |          |     |
|                  | Cell           | Cell         | 7           | Indentation                        | 0-degree (central axial) | 0%            | 5 mm/min |     |
|                  |                |              | 8           |                                    | 0-degree                 | 30%           |          |     |
|                  |                |              | 9           |                                    | 0-degree                 | 60%           |          |     |
|                  |                |              | 10          |                                    | 45-degree                | 0%            |          |     |
|                  |                |              | 11          |                                    | 45-degree                | 60%           |          |     |
|                  |                |              | 12          |                                    | Bending                  | 50mm-span     |          | 0%  |
|                  |                |              | 13          |                                    |                          | 50mm-span     |          | 60% |
|                  |                |              | 14          |                                    |                          | 40mm-span     |          | 0%  |
|                  |                |              | 15          |                                    |                          | 40mm-span     |          | 60% |
| Pouch Cell       | Stacked-sample | 16           | Indentation | 1 mm-particle                      | 0%                       | 0.5 mm/min    |          |     |
|                  |                | 17           |             | 1.5 mm-particle                    | 0%                       |               |          |     |
|                  |                | 18           |             | 2 mm-particle                      | 0%                       |               |          |     |
|                  |                | 19           |             | 2.5 mm-particle                    | 0%                       |               |          |     |
|                  | Cell           | Cell         | 20          | Indentation                        | 20mm-particle            |               | 0%       |     |
|                  |                |              | 21          | Compression                        | Out-of-plane             |               | 0%       |     |

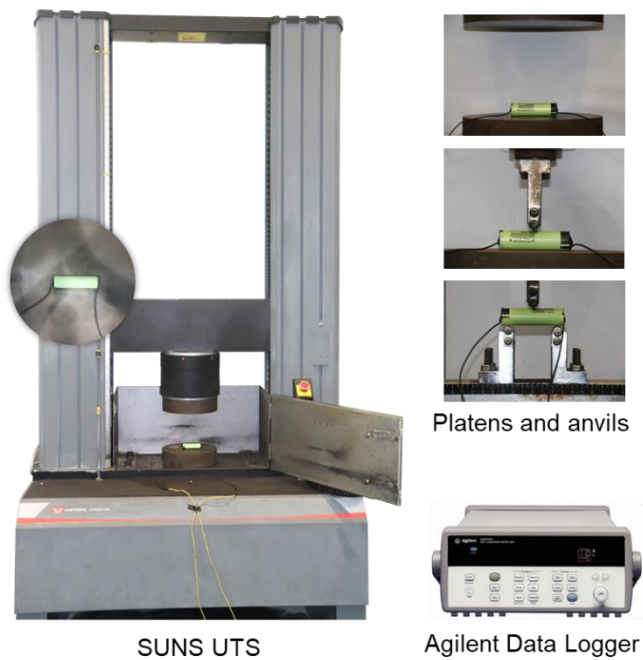


Figure 10 Schematic diagram of the experimental designs and mechanical test platform.

To prepare stacked-layer samples, we disassembled batteries. The component materials, including the anode, cathode, and separator (Fig. 11a), were cut into squares with a dimension of  $30\text{m}\times 30\text{mm}$  and stacked together.

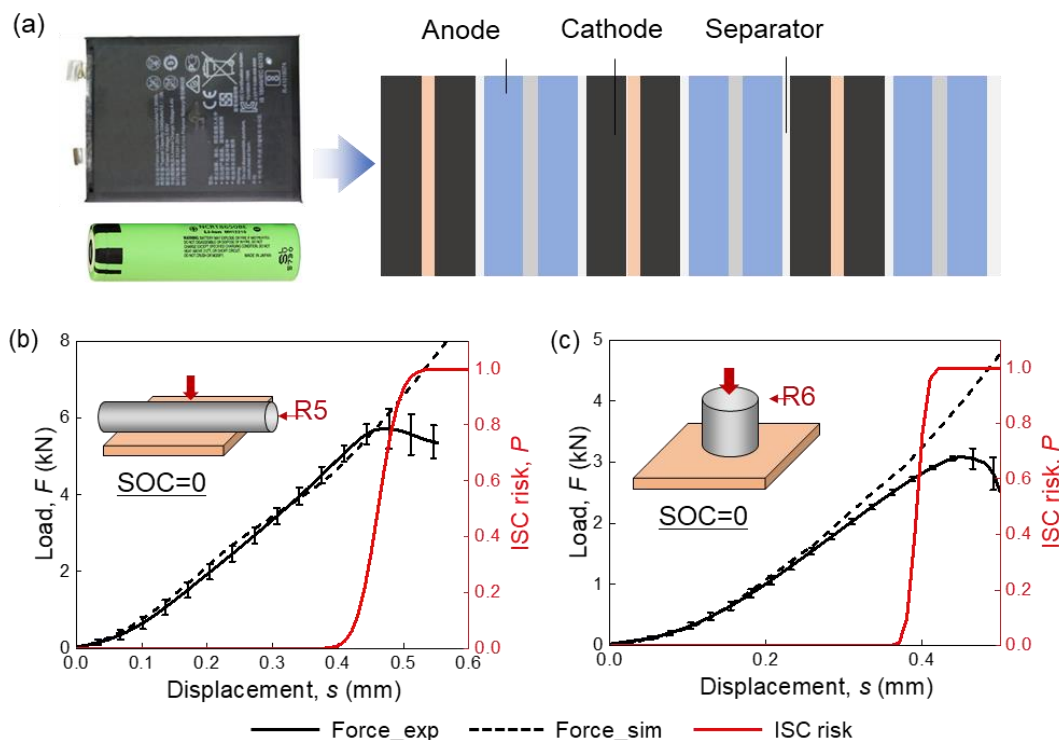


Figure 11 Tests of stacked-layer samples of 18650 cells (a) The stacking structure of the battery jellyroll. Experimental designs of stacked-layer samples: (b) cylinder radial indentation; (c) cylinder axial indentation.

### 3.1.2 Finite element simulation

The mechanical models are developed by Altair Hypermesh and solved by the nonlinear FE solver RADIOSS. Material card MAT28 is used to describe the material properties. The boundary conditions are set the same as the experimental designs. A general contact type (TYPE 7) is used to describe both the part-to-part contact and self-contact. The material properties of the battery components are not directly used in the final cell model due to its high demand for computing. Here, we employ an equivalent material property for the homogenized element according to the periodicity of the layered structure. Thus, the total element number and calculation cost are significantly reduced. The

calculation times for the mechanical models are around 1 hour at Intel core i7 CPU 1.80 GHz 8 cores. The FE models are validated by comparing the load-displacement curves between simulation and experimental results (Figs. 12-16).

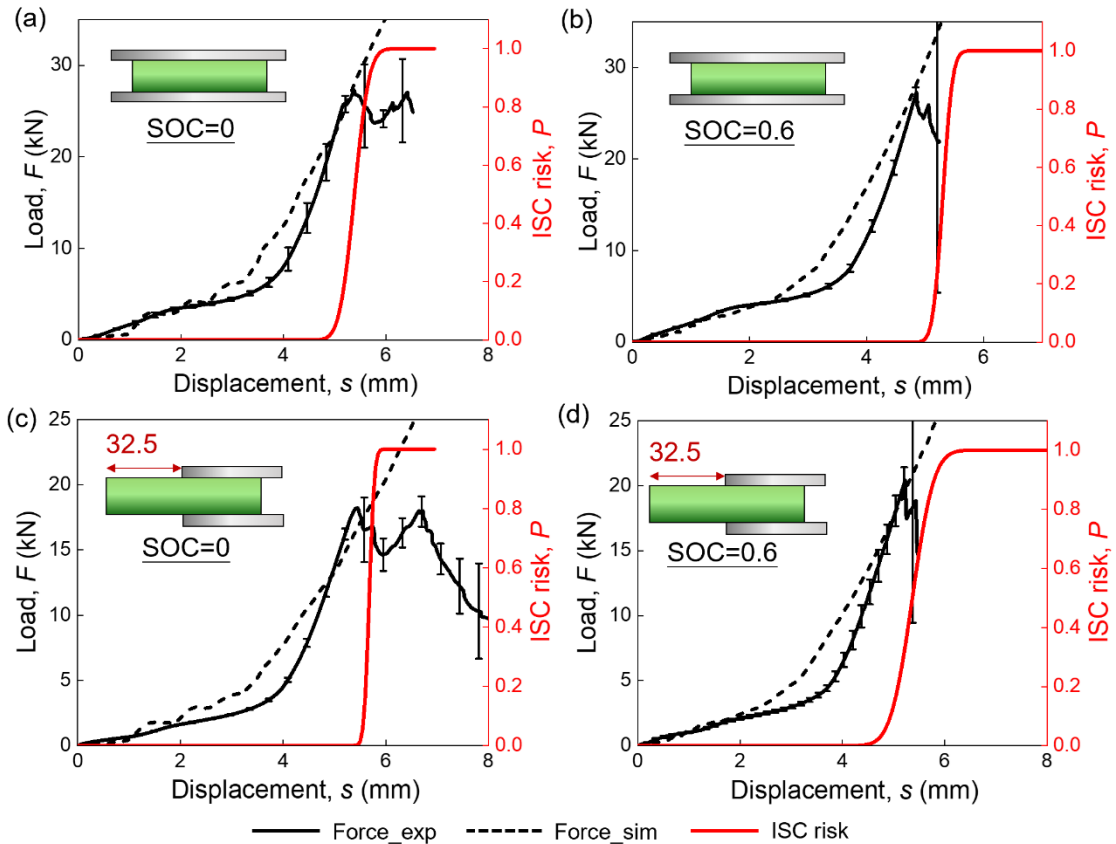


Figure 12 Radial compression tests of 18650 cells. (a) 0%-offset, 0%; (b) 60%-offset, 0%; (c) 0%-offset, 50%; (d) 60%-offset, 50%;

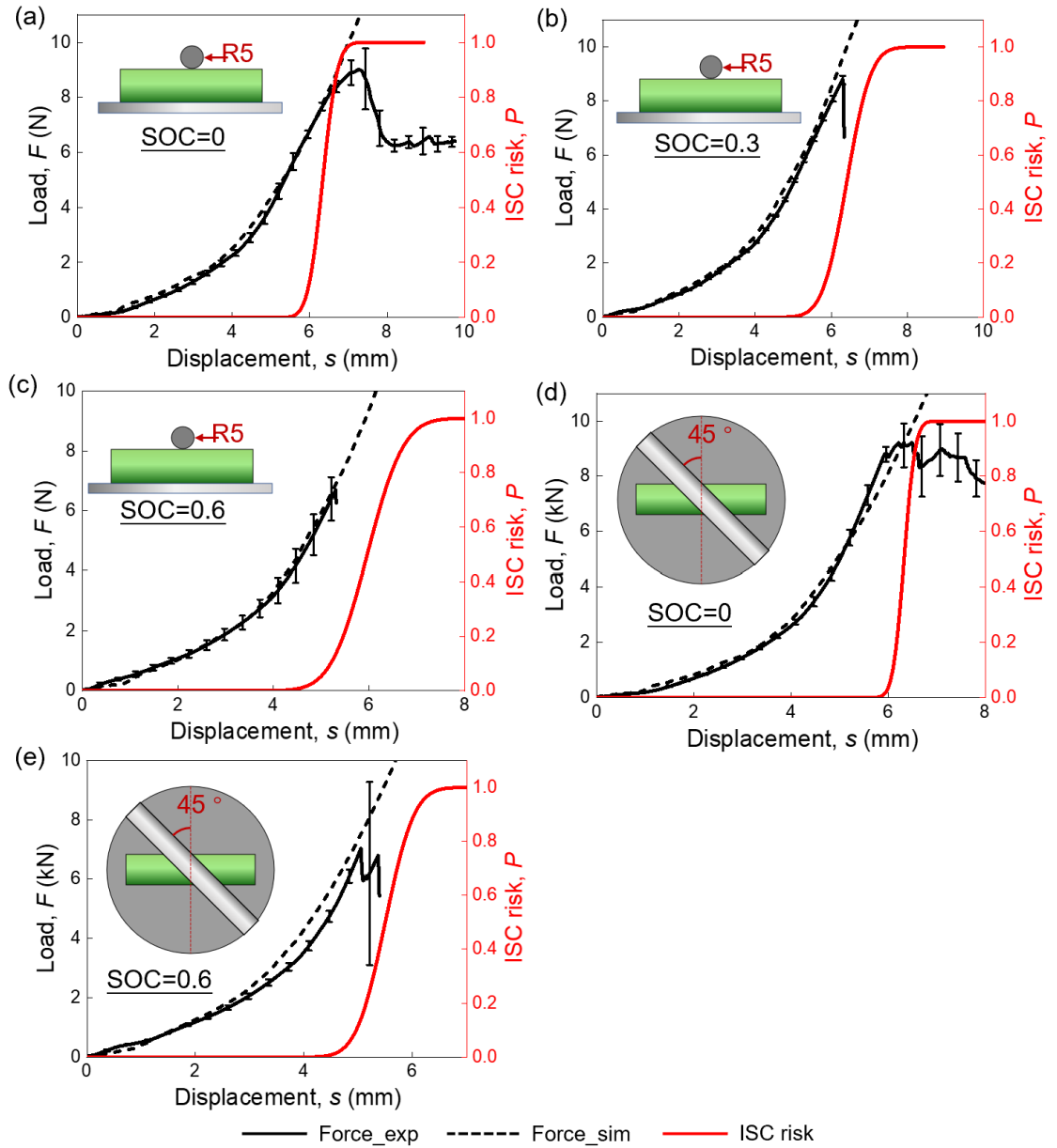


Figure 13 Indentation tests of 18650 cells. (a) 0-degree, 0%; (b) 0-degree, 30%; (c) 0-degree, 60%; (d) 45-degree, 0%; (e) 45-degree, 60%.

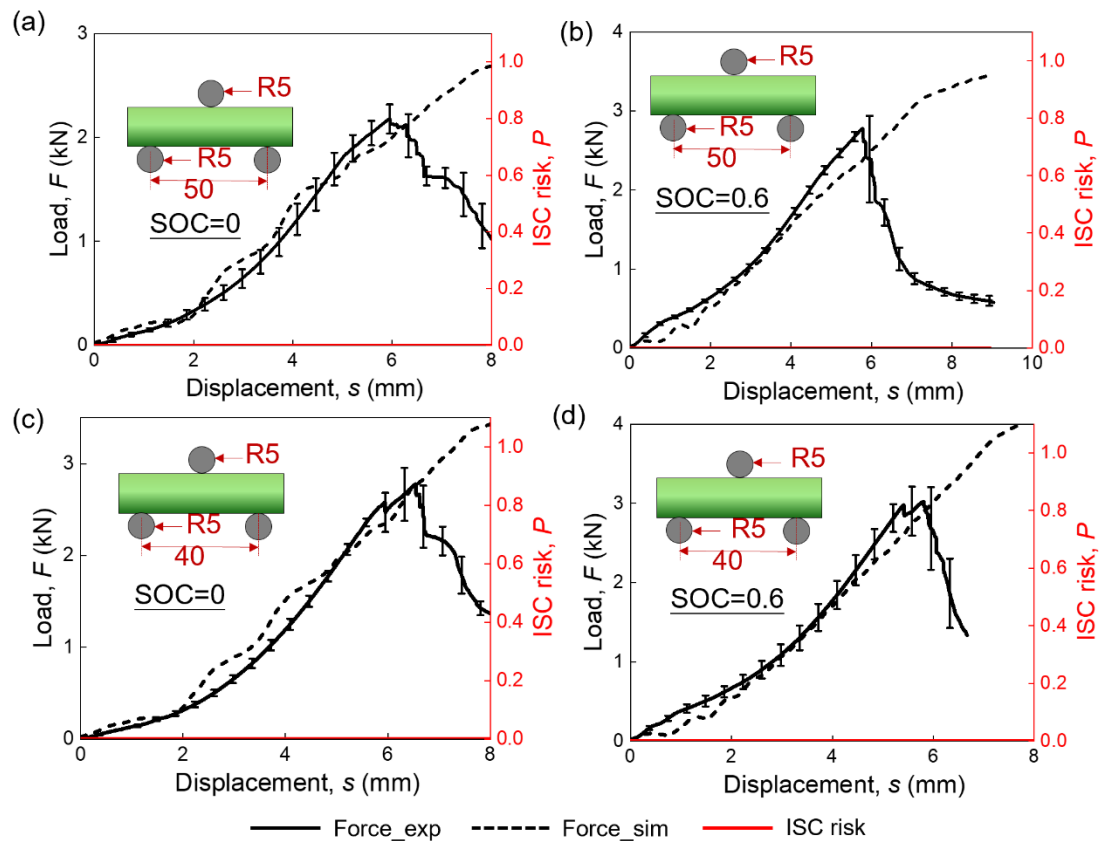


Figure 14 Three-point bending of 18650 cells. (a) 50mm-span, 0%; (b) 50mm-span, 60%; (c) 40mm-span, 0%; (d) 40mm-span, 60%;

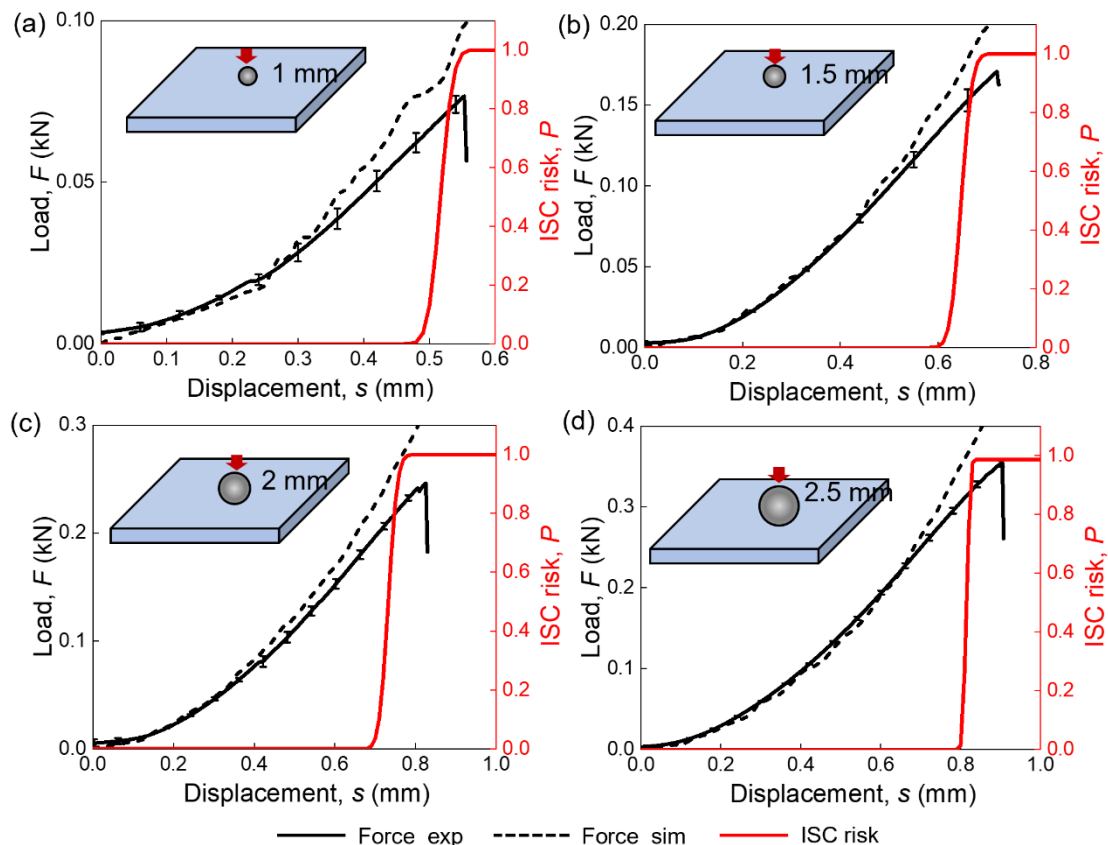


Figure 15 Tests of stacked-layer samples of pouch cells. (a)  $D = 1$  mm; (b)  $D = 1.5$  mm; (c)  $D = 2$  mm; (d)  $D = 2.5$  mm;

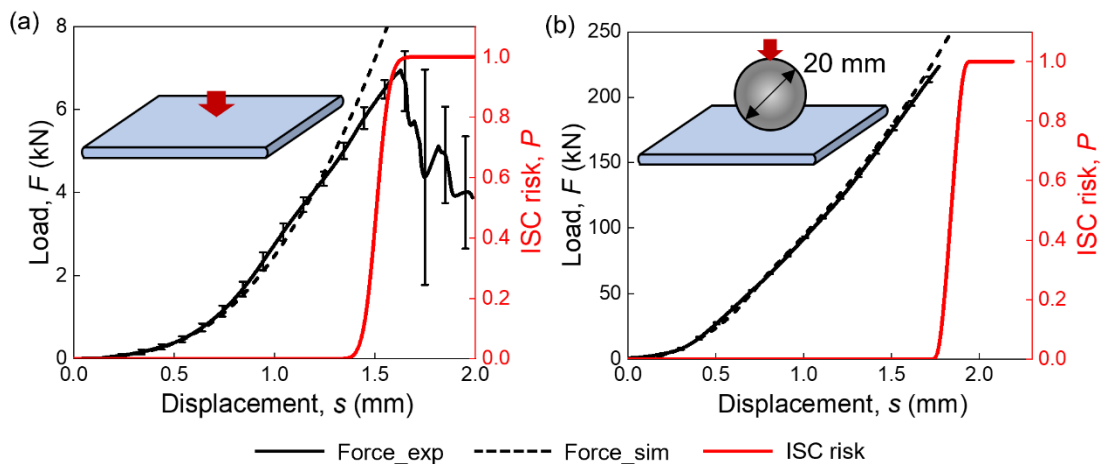


Figure 16 Tests of pouch cells. (a) out-of-plane compression; (b) 20mm-diameter sphere indentation.

### 3.1.3 Machine learning algorithm

The ML algorithm SVR with RBF kernel is trained to develop the data-driven safety

risk prediction model (APPENDIX A). To increase the model stability and reduce complexity, we perform the data standardization and matrix dimensionality reduction.  $Y$  is mapped to the range  $(-\infty, +\infty)$  before feeding the data to improve the stability of the predicted curves:

$$Y' = -\ln\left(\frac{1}{Y} - 1\right), \quad (16)$$

and the predicted  $Y_p$  should be calculated by the following equation after predicting:

$$Y_p' = \frac{1}{1 + e^{-Y_p}}, \quad (17)$$

where  $Y_p$  is the prediction. Three hyper-parameters,  $C_{SVR}$ ,  $\gamma_{SVR}$ , and  $\varepsilon_{SVR}$ , are optimized via the exhaustive grid search program. The training results and durations are listed in Table 5. The ML models are validated by comparing ISC risk-displacement curve between predictions and statistical data (Fig. 18).

A Support Vector Machines (SVM) problem is a quadratic programming problem (QP). The algorithm complexity of the QR solver is between  $O(n_{\text{feature}} \times n_{\text{sample}}^2)$ , and  $O(n_{\text{feature}} \times n_{\text{sample}}^3)$ . The computational requirements increase quicker with the number of training vectors  $n_{\text{sample}}$  rather than the feature number  $n_{\text{feature}}$ . Thus, SVMs are suitable for the ISC prediction problem because the feature number is very large while the training sample is relatively small. The time cost is trivial in the magnitude of seconds (Table 5).

### 3.2 Results and discussion

### 3.2.1 Data generation

To validate the methodology, we selected two common types of commercially used LIBs in this study, i.e., cylindrical cell and pouch cell. The cylindrical cell is a type of 18650 cell with NCA cathode and graphite anode widely used in electric vehicles. The size is 18 mm (diameter) ×65 mm (length). The pouch cells with LCO cathode and graphite anode are widely used in cellphones and computers. The dimension is 82 mm×63 mm×4.4 mm. Generally, a LIB cell consists of a battery casing, a winding structure jellyroll, and some other minor electrical and structural parts (Tables 2 and 3).

Table 2 Basic information of cylindrical cells.

| <b>Parameters</b>          | <b>Value</b>    |
|----------------------------|-----------------|
| Nominal capacity           | 3.350 Ah        |
| Charging cutoff voltage    | 4.2 V           |
| Discharging cutoff voltage | 3.7 V           |
| Cathode thickness          | 0.17 mm         |
| Anode thickness            | 0.2 mm          |
| Separator thickness        | 0.016 mm        |
| Cathode material           | NCA             |
| Anode material             | Graphite        |
| Separator material         | PP/PE           |
| Cathode collector material | Al              |
| Anode collector material   | Cu              |
| Al plastic film            | Al plastic film |
| Layer number               | 19              |

Table 3 Basic information of pouch cells.

| <b>Parameters</b>          | <b>Value</b> |
|----------------------------|--------------|
| Nominal capacity           | 3.350 Ah     |
| Charging cutoff voltage    | 4.4 V        |
| Discharging cutoff voltage | 3.7 V        |
| Cathode thickness          | 0.26 mm      |
| Anode thickness            | 0.21 mm      |
| Separator thickness        | 0.016 mm     |

|                            |                    |
|----------------------------|--------------------|
| Cathode material           | LiCoO <sub>2</sub> |
| Anode material             | Graphite           |
| Separator material         | PP                 |
| Cathode collector material | Al                 |
| Anode collector material   | Cu                 |
| Al plastic film            | Al plastic film    |
| Layer number               | 24                 |

The LIB mechanical models are developed based on the Representative Volume Element (RVE) method to ensure generality and calculation efficiency. For cylindrical cells, the RVE model of the jellyroll consists of two layers of the anode, two layers of the cathode, and four layers of the separator (Fig. 17a). An orthotropic crushable foam material model is used for these three component materials. The material properties of the jellyroll are obtained from material tests. The yield curves in the *ZZ*, and *XX/YY* directions are obtained from the out-of-plane compression (Fig. 17b)<sup>32</sup> and in-plane tension tests (Fig. 17c)<sup>2, 113, 114</sup>. As such, the RVE model can calculate the equivalent stress-strain curve in all three directions (Fig. 17d). Then, the detailed RVE can be represented by a homogenized equivalent element. The equivalent material properties are used to develop cell models. Here, a transversely isotropic crushable foam material model is used to develop the homogenized equivalent element. Also, the steel shell of the cylindrical cells with a thickness of 0.012 mm is considered. Johnson-Cook model is used to describe the elastoplastic behavior of the shell<sup>114</sup>. All the other trivial mechanical parts, such as the pressure release mechanism, are ignored. Similarly, for the pouch cell, the jellyroll is modeled in the same way, and the material properties are taken directly from our previous

work<sup>19</sup>. The pouch cell casing is ignored here due to its low stiffness and thin thickness (about 0.1 mm, at least an order of magnitude smaller than the thickness of the cell)<sup>37,66</sup>.

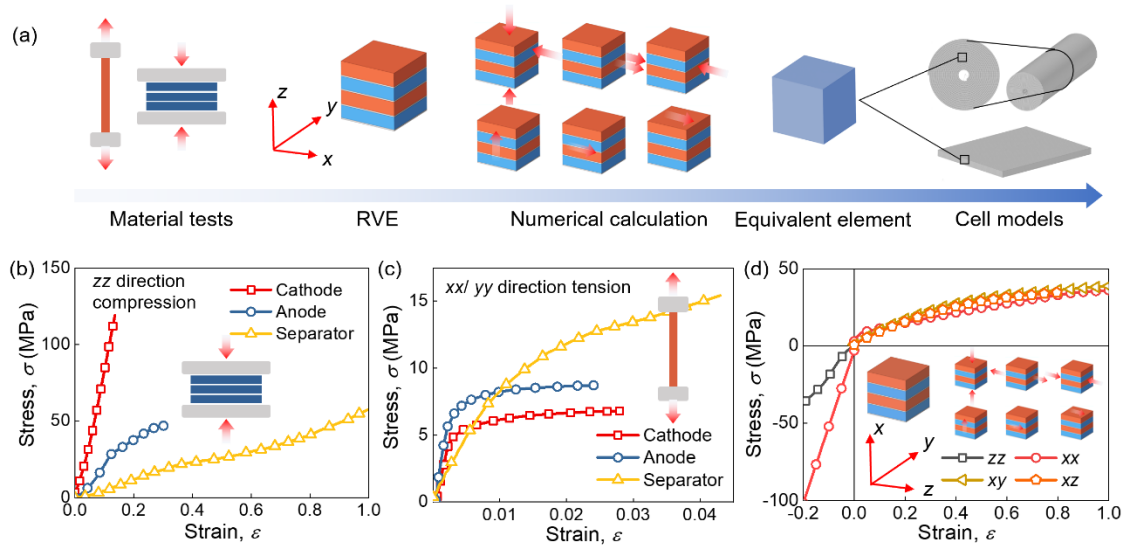


Figure 17 Finite element modeling methods of cells. (a) Mechanical modeling flow chart and testing curves of cell constituents in (b) the ZZ direction and (c) XX/YY directions. (d) Equivalent stress-strain curves are computed from the RVE model.

To validate the mechanical models and generate a sufficient dataset, we conducted mechanical tests of two types of testing samples, including stacked-layer samples and single-cell samples. Representative mechanical loading conditions, including compression, indentation, and bending, were selected (Fig. 10). The stacked-layer samples were used to validate the mechanical RVE model and to generate the training dataset of jellyroll (Fig. 11a). For cylindrical cell stacks (32 layers), we conducted indentations in the axial direction (Figs. 18a and b). For pouch cell stacks (24 layers), sphere indentation tests with four sizes were designed (Fig. 18c).

The single-cell samples were mainly used to validate the cell mechanical model to generate the testing dataset and part of the training dataset (cross template prediction

among loading conditions). The single-cell samples are prepared by a cycler. The cells were fully discharged and then charged to the target State of Charge (SOC) = 0.3 and 0.6, respectively. For cylindrical cells, six loading conditions were designed, including 0%- and 50%-offset compression (Figs. 18d and e), 0- and 45-degree indentation (Figs. 18f and g), as well as 50mm- and 40mm-span three-point bending conditions (Figs. 18h and i). For pouch cells, out-of-plane compression and 20mm-radius sphere indentation were designed (Figs. 18j and k). All experiments were repeated 5 times to ensure repeatability. The FE model accurately predicts the mechanical response at various conditions (Fig. 19). Note that even if some points in the force-displacement curves have some discrepancy to the testing data, the effect on the overall accuracy of predicted safety risk is limited. Because in this study, the ML model is used to predict if the short circuit battery occurs (i.e., short circuit possibility) at a specific loading condition (deformation/strain). Thus, the training samples (points in the force-displacement curves) within the vicinity of the ISC triggering point (*e.g.*, 5mm-7mm in Fig.19, short circuit possibility  $Y$  increase from 0 to 1) weigh much more in the output  $Y$ . Thus, for the data samples in the early stage, *e.g.*,  $Y$  is zero (or close to zero), the deviation in load-displacement affects the results little.

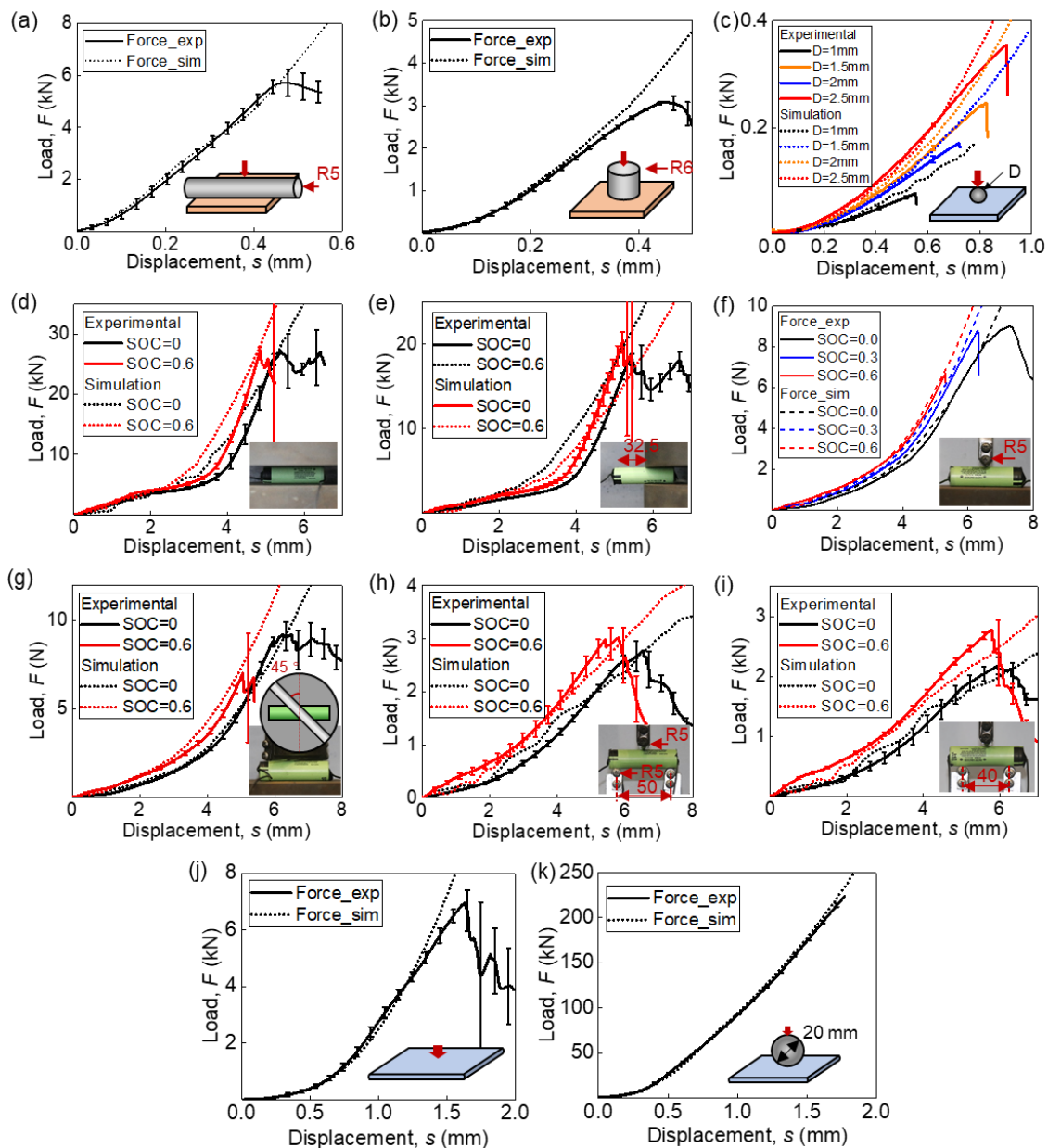


Figure 18 Experimental designs and test results. Experimental results of stacked-layer samples: (a) cylinder radial indentation; (b) cylinder axial indentation of cylindrical cells, and (c) particle indentation of pouch cells. Experimental results of single-cell samples: (d) 0%-offset compression, (e) 50%-offset compression, (f) 0-degree indentation, (g) 45-degree indentation, (h) 50mm-span three-point bending, and (i) 40mm-span three-point bending of cylindrical cell; (j) out-of-plane compression, and (k) 20mm-diameter sphere indentation of pouch cells.

Considering nonlinearity, complexity, and uncertainty of the safety behaviors of LIBs, the safety risk, defined as the probability of the triggering of ISC, is set as  $Y$ . In terms of

feature selection (FS), the most important goal is to select a group of the most representative features based on the original data <sup>115</sup>. In the mechanical stress-driven scenarios, ISC is expected to be highly dependent on the deformation of cells or the component materials. Thus, the most representative feature is the strain state of the battery that can be expressed as a strain field variable  $\boldsymbol{\varepsilon}(x, y, z)$ , a six-dimension vector. Thus, without loss of generality, the argument vector  $\mathbf{X}$  should be a high-dimensional vector that describes the feature of the strain state of the battery. Considering that the strain field cannot be directly obtained from experiments, the finite element simulation described above is used to assist the data generation.

For a specific loading condition (Fig. 19a), the strain field  $\boldsymbol{\varepsilon}(x, y, z)$  of the jellyroll can also be written as the function of displacement  $s$ , i.e.,  $\boldsymbol{\varepsilon}(x, y, z) = f(s)$ , where  $\boldsymbol{\varepsilon}$  is a six-dimensional vector. The six dimensions are six strain components, i.e.,  $\varepsilon_{xx}, \varepsilon_{yy}, \varepsilon_{zz}, \varepsilon_{xy}, \varepsilon_{yz}$ , and  $\varepsilon_{zx}$ . According to the periodicity and continuity of the jellyroll, we ignore the position information and map the strain state  $\boldsymbol{\varepsilon}(x, y, z)$  of all points (or elements) into a six-dimensional space  $\mathbf{R}^6$  (visualized by two  $\mathbf{R}^3$  spaces in Fig. 19a). The region formed by the mapping represents the current strain state of the jellyroll (black dot line in Fig. 19a). Standardize the components by the equation:

$$\varepsilon'_i = \frac{\varepsilon_i - \varepsilon_{i,\min}}{\varepsilon_{i,\max} - \varepsilon_{i,\min}}, \quad (18)$$

where  $\varepsilon_{i,\min}$  is the minimum value and  $\varepsilon_{i,\max}$  is the maximum value for all points (or elements), and discretize the space by a step of 0.1. The area can be expressed by a six-

dimensional matrix  $\boldsymbol{\varepsilon} \rightarrow h_{iklmn}(i, j, k, l, m, n = 0, 1, 2 \dots 10)$ . It satisfies:

$$h_{iklmn} = \begin{cases} 1, & (\text{area } [i, j, k, l, m, n] \text{ is covered (red cube)}) \\ 0, & (\text{area } [i, j, k, l, m, n] \text{ is not covered (blank)}) \end{cases} \quad (19)$$

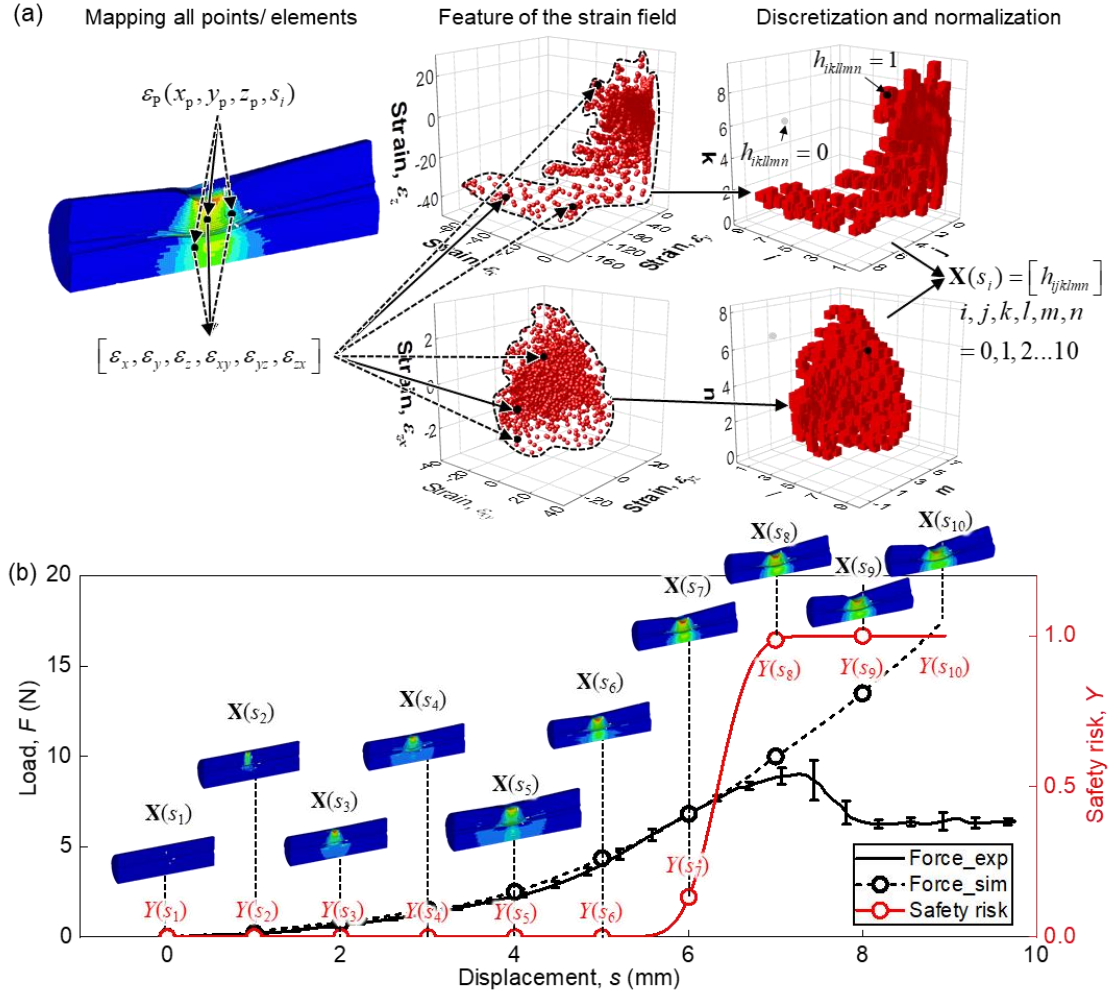


Figure 19 Generation methodology of the argument vectors and their mapping relationship. (a) the generation of argument vector  $\mathbf{X}$ , (b) the mapping relationship between  $\mathbf{X}$  and  $Y$ .

$h_{iklmn}(i, j, k, l, m, n = 0, 1, 2 \dots 10)$  is finally transferred to the argument vector  $\mathbf{X}$  with a dimension of  $10^6$  (compress all dimensions to one dimension):

$$\mathbf{X}(s_i) = [h_{0,0,0,0,0,0}, h_{1,0,0,0,0,0}, \dots, h_{10,0,0,0,0,0}, \dots, h_{10,10,0,0,0,0}, \dots, h_{10,10,10,10,10,10}] \quad (20)$$

To improve calculation efficiency, we use the Principal Component Analysis (PCA)

before feeding the data. Thus, along the force-displacement curve, several training samples can be generated,  $\mathbf{X}$  and  $Y$  can be bridged by  $s$  (Fig. 19b):  $(\mathbf{X}_i, Y_i) = (\mathbf{X}(s_i), Y(s_i))$ ,  $s_i = s_0, s_1, s_2 \dots s_T$ , where  $s_i$  can be selected as an arithmetic progression and  $s_T$  is the loading terminal displacement in simulation. The same method is also applied to other cases (Figs. 12–16), and the samples are obtained and summarized (Table 4).

Table 4 Summary of all the generated training samples.

| Cell types       | Sample types   | Cases  | Group No.                             | Sample Numbers |     |
|------------------|----------------|--|---------------------------------------|----------------|-----|
| Cylindrical cell | Stacked-sample | Cylinder radial direction indentation, 0%SOC | 1                                     | 70             |     |
|                  |                | Cylinder axial direction indentation, 0%SOC  | 2                                     | 70             |     |
|                  | Cell           |  | 0%-offset radial compression, 0%SOC   | 3              | 140 |
|                  |                |  | 0%-offset radial compression, 60%SOC  | 4              | 140 |
|                  |                |  | 50%-offset radial compression, 0%SOC  | 5              | 140 |
|                  |                |  | 50%-offset radial compression, 60%SOC | 6              | 140 |
|                  |                |  | 0-degree indentation, 0%SOC           | 7              | 180 |
|                  |                |  | 0-degree indentation, 30%SOC          | 8              | 180 |
|                  |                |  | 0-degree indentation, 60%SOC          | 9              | 180 |
|                  |                |  | 45-degree indentation, 0%SOC          | 10             | 180 |
|                  |                |  | 45-degree indentation, 60%SOC         | 11             | 180 |
|                  |                |  | 50mm-span bending, 0%SOC              | 12             | 180 |
|                  |                |  | 50mm-span bending, 60%SOC             | 13             | 180 |
|                  |                |  | 40mm-span bending, 0%SOC              | 14             | 180 |
|                  |                |  | 40mm-span bending, 60%SOC             | 15             | 180 |
| Pouch Cell       | Stacked-sample | 1mm-particle indentation, 0%SOC              | 16                                    | 80             |     |
|                  |                | 1.5mm-particle indentation, 0%SOC            | 17                                    | 100            |     |
|                  |                | 2mm-particle indentation, 0%SOC              | 18                                    | 110            |     |
|                  |                | 2.5mm-particle indentation, 0%SOC            | 19                                    | 120            |     |
|                  | Cell           |  | 20mm-particle indentation, 0%SOC      | 20             | 200 |
|                  |                |  | Out-of-plane compression, 0%SOC       | 21             | 220 |

### 3.2.2 Machine learning approach and safety risk prediction.

The safety risk prediction consists of both offline and online processes (Fig. 20). During the offline process, the dataset is generated, and a data-driven safety risk prediction model is developed. Here, the SVR with RBF kernel from the open-source library scikit-learn is used because it is memory efficient, versatile, and effective in high dimensional spaces<sup>116</sup>. In the online processes, the boundary conditions and loading displacement will be input into the mechanical model. After the calculation of the FE model and the data processing, the strain state vector  $\mathbf{X}_p$  is calculated and fed into the safety risk prediction model. The model then will return the safety risk  $Y_p$ . Four predictors are designed and trained to demonstrate the performance of the methodology (Table 5). 6-fold cross-validation is conducted to avoid over-fitting. The mean score and the standard deviation are also summarized (Table 5).

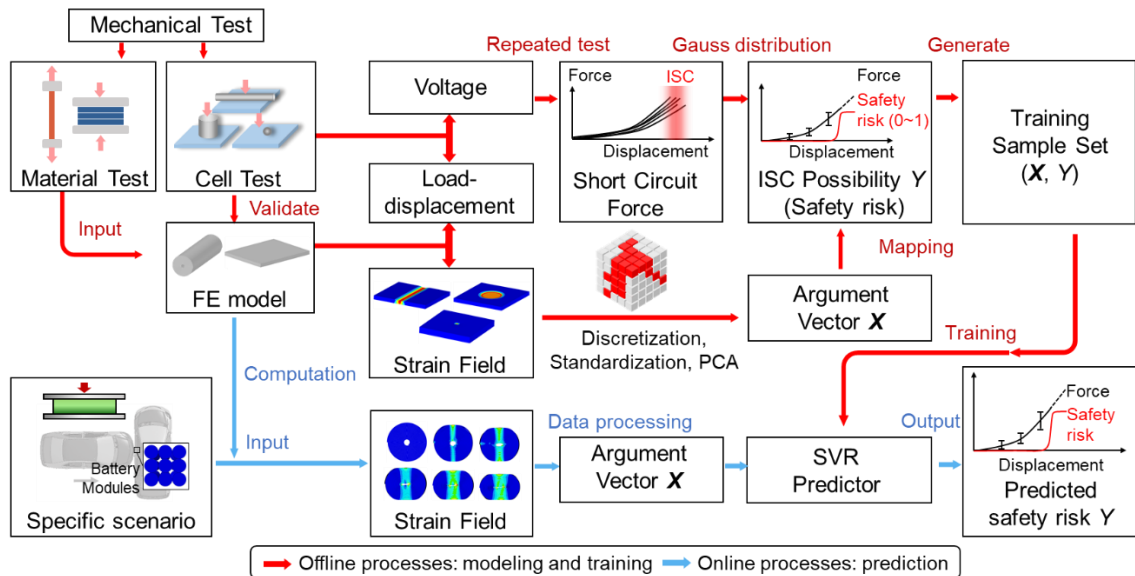


Figure 20 The flow chart of the offline training and online prediction processes.

Table 5 The training/ testing sample combinations and corresponding model parameters.

| Predictor | Battery types | Training samples | Hyper-parameters ( $C_{SVR}$ , $\gamma_{SVR}$ , $\epsilon_{SVR}$ ) | Cross-validation scores (mean value, standard deviation) | Training time (s) | Testing samples |
|-----------|---------------|------------------|--|--|-------------------|-----------------|
| 1         | Cylindrical   | 1, 2             | (1e3, 4.5e-3, 1e-3)  | (0.958, 0.009)   | 0.335             | 3, 7, 12        |
| 2         | Pouch         | 16-19            | (1e3, 1e-3, 1e-2)  | (0.933, 0.014)   | 1.570             | 20, 21          |
| 3         | Cylindrical   | 7, 9             | (5e2, 1e-3, 1e-2)  | (0.985, 0.004)   | 1.484             | 8               |
| 4         | Cylindrical   | 3,4,7,9,12,13    | (5e2, 1e-3, 1e-2)  | (0.987, 0.003)   | 9.545             | 5,6,10,11       |

Take the indentation of the cylindrical cell, for example. The loading  $F$  gradually increases, and the safety risk  $Y$  keeps zero at first when the battery is mechanically loaded (Fig. 21a). When the loading force or displacement is large enough,  $Y$  starts increasing and reaches 1 rapidly. According to the safety risk, the loading process can be divided into three main stages: (1) Stage I: Low risk, safety risk close to zero, indicating almost no ISC risk; (2) Stage II: Medium risk, safety risk increases drastically with displacement/force; and (3) Stage III: High risk, ISC will probably occur. Satisfactory prediction results can be observed for both the numerical simulation model for force-displacement curves and the ML model for the safety risks. Cells under other mechanical loading conditions show a similar safety risk trend, except for the three-point bending cases (Figs. 21a-c). Interestingly, the experiment showed that the ISC was not triggered upon three-point bending and the ML model is also capable of predicting the safety risk with low values, indicating no ISC will be triggered.  $R^2$  (coefficient of determination) regression score

function is employed to indicate the goodness of fit. Here, the dataset for 18650 cylindrical cells consists of 140 training samples obtained from two stacked-layer tests, cylinder radial direction indentation (Fig. 11a), and cylinder axial direction indentation (Fig. 11b). Similarly, the model for pouch cells trained by 410 samples obtained by the stacked-layer tests under several indentation loadings (Figs. 15a-d), also provides a satisfactory prediction of ISC risk (Figs. 21d-e). These results prove the good performance and the generality of the ML modeling method to predict the safety risk of lithium-ion batteries.

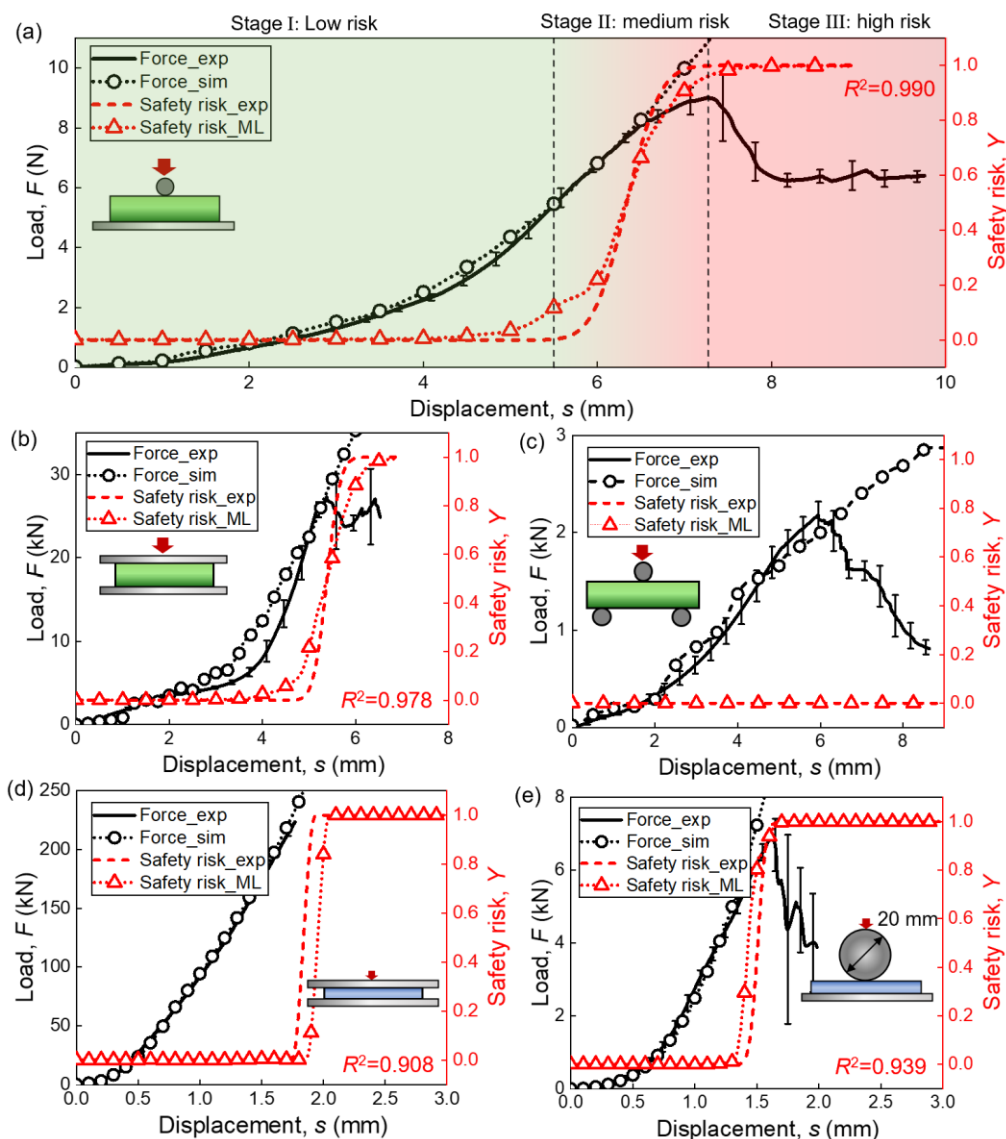


Figure 21 Safety risk evaluation of two types of cells under testing loading conditions. 18650 cylindrical cells under (a) radial compression loading, (b) indentation loading, and (c) three-point bending. And pouch cells under (d) compression loading, and (e) 20mm-diameter sphere indentation loading. (Predictor 1 for Cases a,b, c and Predict 2 for Cases d, e)

### 3.2.3 Generalization

In real-world engineering application scenarios, battery or vehicle designers may not have full access to the cell testing in various scenarios, *e.g.*, cells with various state-of-charges (SOCs) or upon different loading scenarios. In this case, the model established in

this work can also provide a satisfactory cross-template prediction by using the results of some available cell loading tests to evaluate the safety risk of batteries with different SOC's whose safety risks are unknown such as to further facilitate battery safety status monitoring during operation.

According to some previous work, SOC of cells would have an obvious impact on the mechanical responses and ISC behaviors<sup>29, 33, 34, 39</sup>. The indentation tests of the cylindrical batteries also indicate that with the increase of SOC, the force response increases, and the ISC occurs earlier (Fig. 22a). Here the results of 0%-SOC, 60%-SOC indentation tests (Figs. 12a, c) are used to generate the training dataset (360 samples) and then predict the safety risk of the 30%-SOC case. SOC, a real number with a value from 0 to 1, is considered as an additional feature in the input vector  $\mathbf{X}$ . The yield curves are considered proportional to SOC, written as

$$\sigma_{ii} = h(\varepsilon_{ii}, SOC) = k \cdot h(\varepsilon_{ii}, SOC = 0), \quad (21)$$

where  $k$  is a constant value. The results indicate that the model provides a good interpolation prediction of the 30%-SOC case (Fig. 22b).

Similarly, we can use some known loading test results to train the model and obtain an extrapolation prediction of cells under other target loading conditions. Here, the results of the 0%-offset radial compression tests (Figs. 12a-b) and 90-degree indentation tests (Figs. 13a, c) of the cylindrical cell at 0%/ 60% SOC is used to generate the data set and train the model (640 train samples). Then, the model is tested to evaluate the safety risk of

the cells under four testing cases, 50%-offset radial compression (0%/ 60% SOC) (Figs. 22c-d) and 45-degree indentation (0%/ 60% SOC) (Figs. 22e-f). Results demonstrate that the model can also provide satisfactory predictions for various mechanical abuse loading scenarios (Table 6).

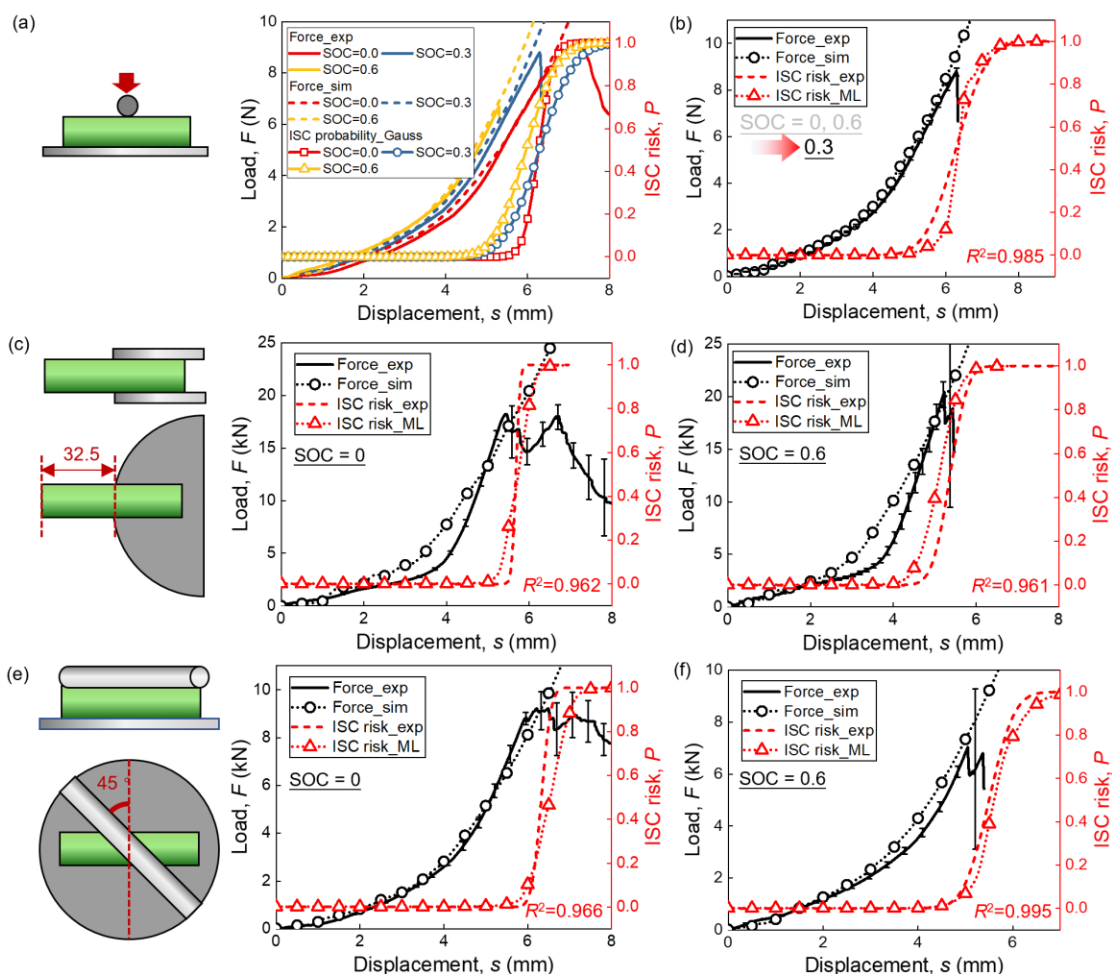


Figure 22 Safety risk prediction of cylindrical cells at different SOC levels and under different loading conditions. (a) Safety risks at different SOC levels, (b) interpolation prediction of safety risk of cells with 30%-SOC under radial compression loading. Extrapolation prediction of safety risk of cells under: 50%-offset radial compression at (c) 0%-SOC and (d) 60% SOC; 45-degree indentation at (e) 0%-SOC and (f) 60%-SOC. (Predicter 3 for Case b and Predicter 4 for Cases c-e)

Table 6 Comparisons of the ISC distance between experimental results and ML predictions.

| Predictors  | Test samples<br>(group<br>numbers) | ISC displacement (mm)<br>(average value $\pm$ standard<br>deviation) |                 | Relative Error<br>(%) |
|-------------|------------------------------------|--|-----------------|-----------------------|
|             |                                    | Experiment   | Simulation      |                       |
| Predictor 1 | 3                                  | $5.39 \pm 0.36$  | $5.40 \pm 0.47$ | 0.222                 |
|             | 7                                  | $6.34 \pm 0.48$  | $6.35 \pm 0.85$ | 0.220                 |
|             | 12                                 | -  | -               | -                     |
| Predictor 2 | 20                                 | $1.96 \pm 0.07$  | $1.84 \pm 0.08$ | 6.12                  |
|             | 21                                 | $1.51 \pm 0.08$  | $1.43 \pm 0.10$ | 5.30                  |
| Predictor 3 | 8                                  | $6.39 \pm 1.04$  | $6.35 \pm 0.53$ | 0.79                  |
| Predictor 4 | 5                                  | $5.68 \pm 0.11$  | $5.75 \pm 0.50$ | 1.32                  |
|             | 6                                  | $6.33 \pm 0.26$  | $6.60 \pm 0.63$ | 4.35                  |
|             | 10                                 | $5.38 \pm 0.51$  | $5.10 \pm 0.60$ | 5.12                  |
|             | 11                                 | $5.50 \pm 0.65$  | $5.25 \pm 0.10$ | 4.55                  |

### 3.2.4 Rationalization

#### 3.2.4.1 Advantages

Besides the versatility of the ML model established, a direct comparison of ISC prediction performance between the SVR predictor and a pure mechanical model based on the Mohr-Coulomb (MC) failure criterion is conducted (Fig .24) to demonstrate the effectiveness of the proposed model in this paper (for the sake of fairness, ML output  $Y$  here is defined as the fracture possibility). A homogenous FE model is also developed for the MC failure criterion (the same as Ref. <sup>5, 45</sup>). Three validation cases (training cases for the predictor, radial compression, indentation, and 50-mm three-point bending) and three testing cases (50%-offset radial compression, 45-degree indentation, and 40-mm three-point bending) are selected. The homogenous FE model is validated by the three validation cases (Simulation 2 in Fig. 23a-c). Based on the suggested methodology in Ref. [7e], the

fracture criterion (line), i.e.,  $\sigma_1 = 0.226\sigma_3 + 0.0277$  (GPa) is determined (Fig. 24a). The MC criterion cannot well predict the ISC displacement of all the cases simultaneously (Fig, 24b). We may notice that the MC criterion-based model can well predict Cases 2, 4, 5, but the relative errors of Cases 1, 3, 6 are huge and unacceptable. The relative errors of the MC criterion range between 10.1%~35.2% for the three prediction cases and up to 36.2% for the validation cases. On the contrary, the SVR predictor not only fits the training cases very well but also provides satisfactory predictions of the unknown testing cases (Fig. 24b). The relative errors are 2.5%~4.3% in our model for the prediction cases and 0% difference in the validation cases. Such results from a direct comparison manifest the superiority of our model.

Previously, the ISC criteria or failure criteria is a criterion that uses a linear combination of stress-components or strain-components to predict the ISC. In this case, when the value of the function is larger than a critical value, the ISC or material failure happens. However, there is a major limitation of the traditional ways: the criterion already contains pre-set stress or strain pattern. It works well on some simple materials or structures while may not on some complicated structures like batteries. Take the MC-based ISC criterion, for example. The principal stress is calculated by the equation  $\sigma_{eq} = \sigma_1 - \alpha\sigma_3$ , where  $\sigma_1, \sigma_3$  are principal stresses calculated from stress components and  $\alpha$  is a constant<sup>5</sup>,  
<sup>45</sup>. Considering the mechanisms of mechanically triggered ISC and limitations of traditional ISC prediction approaches, in this paper, ML method is used to substitute the

criterion. Generally, the mechanically triggered ISC is produced by direct contact between anode and cathode or deformation of the separator reaches a critical state. Thus, the direct reason is the mechanical failure of deformation of the separator. Also, based on the periodical layer structure of cells, that cathode, anode, and separator are always layered together, the deformation of the separator is often corresponding to the deformation of other layers or the overall deformation of the cell. In essence, the deformation can be characterized by the intrinsic strain field of the cell. Thus, the ML features come from the transformation of the strain field of the cell at the short circuit moment.

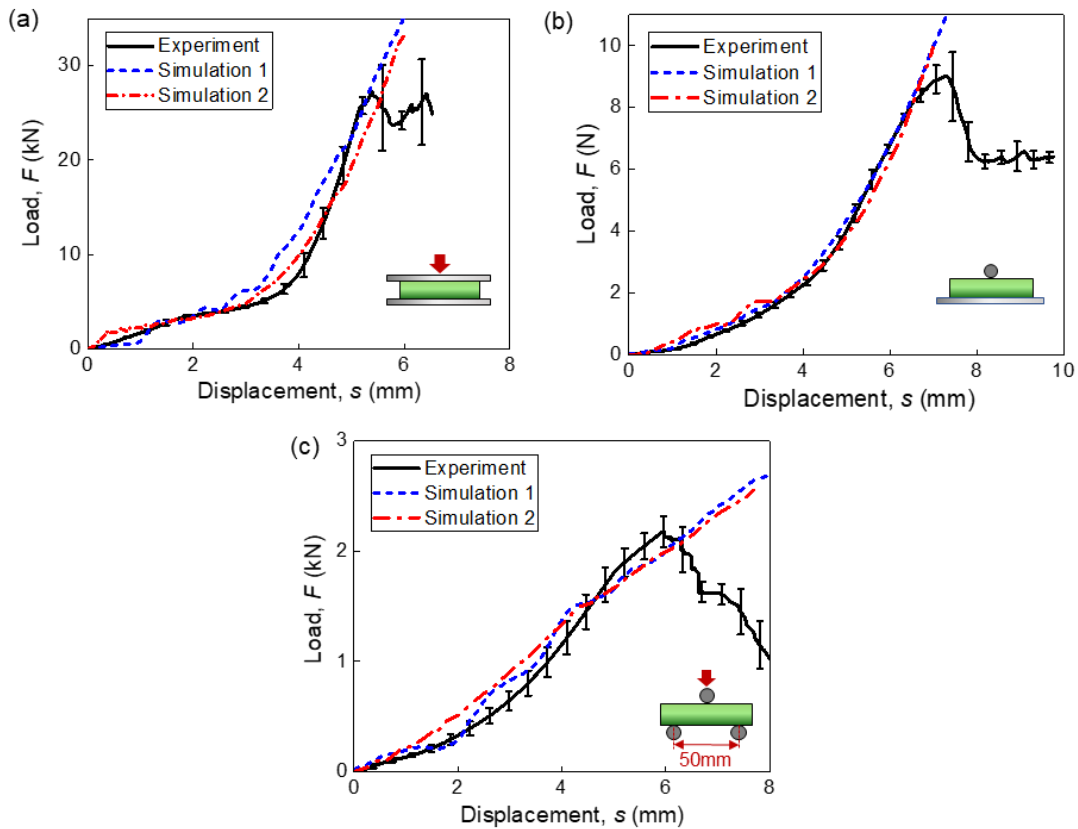


Figure 23 Validation of the FE model for the MC criterion. The model is validated by two typical loading conditions (a) radial compression, (b) indentation, and (c) 50-mm three-point bending (Simulation 1: the FE model developed in this paper; Simulation 2: the homogenous model developed for MC failure criterion from Ref. <sup>5, 45</sup>).

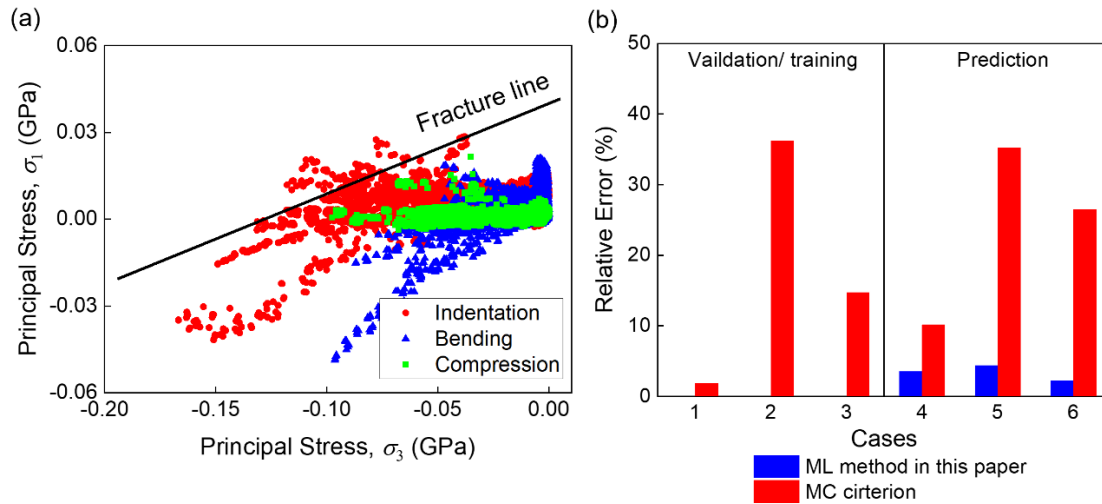


Figure 24 Comparison between the SVR predictor and the Mohr-Coulomb failure criterion. (a) Determination of the fracture line. (b) Comparison of ISC displacement prediction between the SVR predictor and the MC criterion (average value for experiment and the SVR predictor). Case 1: radial compression; case 2: indentation; case 3: 50-mm three-point bending; case 4: 50%-offset radial compression; case 5: 45-degree indentation; case 6: 40-mm three-point bending.

### 3.2.4.2 Pre-conditions and Limitations

Due to the underlying principles, it is worthy to note that good performance is established based on the following pre-conditions.

(1) In the experiment design aspect, the dataset should contain samples generated from loading conditions. In the meantime, the designed mechanical tests should cover as many representative strain or stress combinations as possible, which requires a good understanding of mechanics. In this case, the model can fully capture the strain state features with a highly confident safety risk probability.

(2) In the testing sample and operation aspect, the selected sample batteries are preferable to have good uniformity, and the designed mechanical is better to have good repeatability such that the distribution of the ISC forces or the displacements can be

estimated more accurately.

(3) A high quality of the numerical model is necessary. We demonstrate that the RVE-based method works cost-effectively and accurately because it can significantly reduce the calculation cost while maintaining a reasonable accuracy in terms of the mechanics model computation<sup>117</sup>. More importantly, the RVE-based model can be more general where it can describe various battery formats using basic representative units.

In the meantime, this methodology has the following limitations:

(1) The method is only suitable for mechanically triggered ISC because we suppose that the triggering of ISC is only related to the strain state (or stress state) of the structures where the material coordinates are not considered as features.

(2) The FE model may introduce possible modeling and computational errors, which will be further accumulated in the ML model. It is difficult for the FE model to perfectly predict the stress or strain value at each point. Thus, to avoid these errors to the greatest extent, the selected features of the ML model should be comprehensive descriptions of the strain/ stress field rather than several representative points.

(3) This trained model can predict the ISC risk under mechanical loading of various types of batteries (cylindrical, pouch, and prismatic cells) with the same constituent materials. However, if the constituent materials change, the data set should also be updated accordingly.”

(4) The ISC triggering under mechanical behaves in probabilistic ways for many

unknown reasons, such as inconsistency of the battery samples. It is safe to use a probability to describe the ISC risk under mechanical loading only before its underlying mechanisms are clear.

(5) For future applications involving electrochemical (*e.g.*, Li dendrite/plating, particle cracking), and thermal (*e.g.*, separator melting) abuse caused battery safety issues, electro-chemo-mechanical models with proper criteria using intrinsic electro-chemo-mechanical features should be introduced<sup>1, 118, 119</sup>. In general, the materials or structures fail when their strain states satisfy one specific or several features.

### 3.3 Conclusions

Data-driven modeling based on the prior numerical modeling is a new promising way for predicting the safety risk of lithium-ion batteries with significantly reduced time-/cost-consuming and dangerous safety experiments. In this chapter, we firstly propose the concept of safety risk since, for a complicated and highly nonlinear system like the battery, the triggering of the internal short circuit contains stochastic factors and cannot be determined definitively. With the assistance of numerical simulation and experiments, we generate a sufficient number of datasets. We then establish an ML-based model to describe and predict the internal short circuit risk of a single cell upon mechanical abusive loading. The coefficient of determination  $R^2 > 0.90$  for the entire safety risk curve for both cylindrical cells and pouch cells was observed. The relative error of the average ISC prediction is less than 6.2%. Furthermore, the generalizability of the ML-based safety risk predictor was

demonstrated by extending the scenarios for cells with various SOC's and loading conditions. The success of the model manifests that the strain field should be a dominant factor for the mechanical stress-induced internal short circuit. Our model is proven to substitute current time-consuming numerical simulation models and high-risk experiments and enables fast prediction and monitoring for possible safety risks. This work highlights the promise of combining the physical model with a data-driven model and streamlines the methodology for understanding energy storage systems.

## CHAPTER 4 SAFETY RISK LEVELS UPON STRESS-DRIVEN INTERNAL SHORT CIRCUIT

In this chapter, we first define four safety risk levels according to the multiphysics behavior of cells under mechanical abusive loading and develop a safety risk level classification model that can accurately and quickly predict the safety risk level of the LIB cells during the charging/ discharging. Decision Tree and Support Vector Classifier (SVC) are used to construct the model and realize the cell state classification. The classification is only based on a short period of voltage and current signals. To generate as much training samples as possible, a multiphysics surrogate model is developed.  $\sim 3 \times 10^5$  training samples are generated, covering SOC from 10% to 100%, short circuit resistance from  $10^{-1} \Omega$  to  $10^3 \Omega$ , and C-rate from 0.1 to 2. The prediction results show that the classifiers have a good performance (F1 scores  $> 0.93$ ) and robustness (F1 scores  $> 0.87$  when a voltage error of 0.1 mV is introduced). The prediction results show that the models have a good performance and robustness.

### 4.1 Methods

#### 4.1.1 Experimental designs and typical results.

Two typical scenarios can cause/exhibit battery safety issues, *i.e.*, cycling test and abusive testing. The experimental designs are:

##### (1) Cycling tests

The short-term cycling tests (without obvious capacity loss) were conducted with the LANHE CT2001B battery test system. Several constant resistors were selected and

connected to the cell in parallel during charging/discharging to produce current leakage (Fig. 25a). The test samples are commercially used NCM pouch cells with a capacity of 3.6 Ah and dimensions of 97 mm×58 mm×4.5 mm. The cutoff voltages are 2.8 V/ 4.35 V. The experimental setup is summarized in Table 7. CC-CV charging/ discharging method was used. The minimum current at the CV stage was set as 1/20 C.

The batteries without resistance were used to represent normal batteries (L0). The battery works normally during charging and discharging (Fig. 25b). The batteries with external short circuit resistance were used to simulate the damaged batteries (L1). Due to current leakage, the voltage curves were slightly different from the curve of the normal battery: increase slower during charging and decrease quicker during discharge and cannot reach minimum current in CV stage when  $R=20\ \Omega$  (Fig. 25c).

## (2) ISC triggering tests.

The quasi-static mechanical loading tests were conducted to trigger the ISC of the cells (Fig. 25d). The tests were carried out with the INSTRON LEGEND 2386 universal testing machine. An 8-mm indenter moves downward with a speed of 1 mm/min till the ISC of the cell was triggered. During the loading, the voltage and surface temperature (Fig. 25d) were measured by HIOKI LR8431 high-speed data loggers. Cells with initial SOC from 0.1 to 1 were used. If TR will be triggered mainly depends on the initial conditions of the cell, such as initial SOC. For medium SOC (60%), the temperature rise was small and not enough to trigger the TR (L2, Fig. 25e). For high SOC (100%), the temperature

increased quickly, and TR was triggered (L3, Fig. 25f).

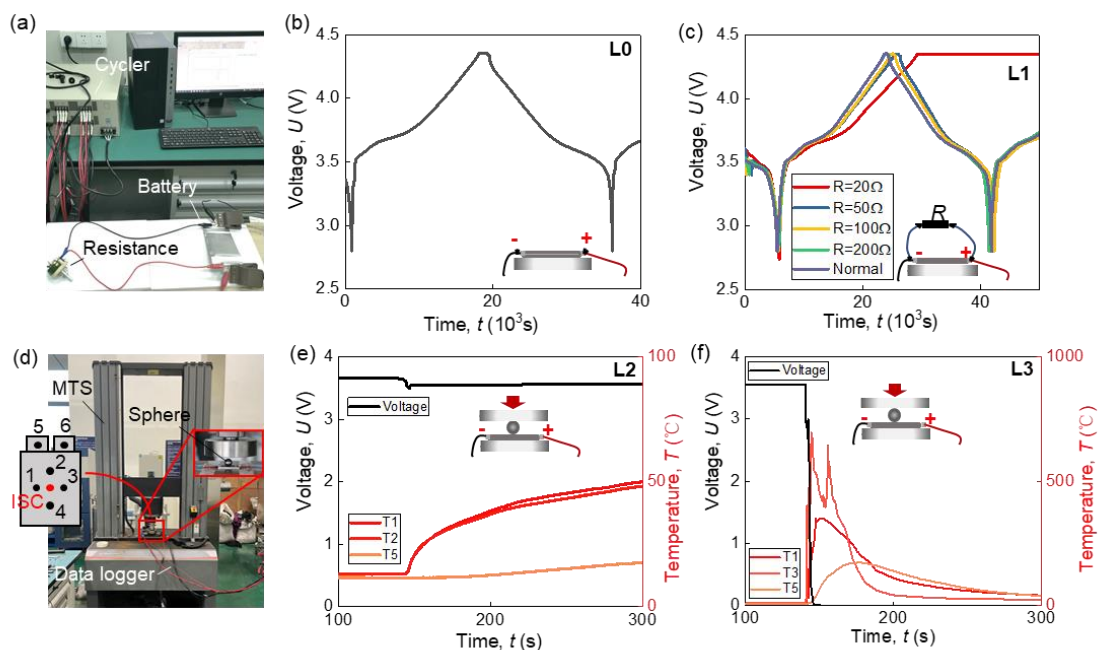


Figure 25 Classification of battery safety issues. (a) Cycling test experimental design and the typical behaviors: (b) L0 normal battery; (c) L1 damaged battery; (d) ISC triggering test experiment design and the typical behaviors: (e) L2 ISC is triggered but no TR; (f) L3 ISC is triggered, and TR will be triggered.

Table 7 Experimental setup of the cycling tests

| Resistance, $R$ (ohm) | C-rate              | Cycles for each combination |
|-----------------------|---------------------|-----------------------------|
| 500                   | 2, 1.5, 1, 0.5, 0.2 | 3                           |
| 200                   | 2, 1.5, 1, 0.5, 0.2 | 3                           |
| 100                   | 2, 1.5, 1, 0.5, 0.2 | 3                           |
| 50                    | 2, 1.5, 1, 0.5, 0.2 | 3                           |
| 20                    | 2, 1.5, 1, 0.5, 0.2 | 3                           |

#### 4.1.2 Multiphysics model development.

The multiphysics surrogate model was developed to aid the data generation. The model has four sub-models (Fig. 26): (1) Battery model; (2) Short circuit model; (3) Heat

transfer model; (4) Thermal runaway model.

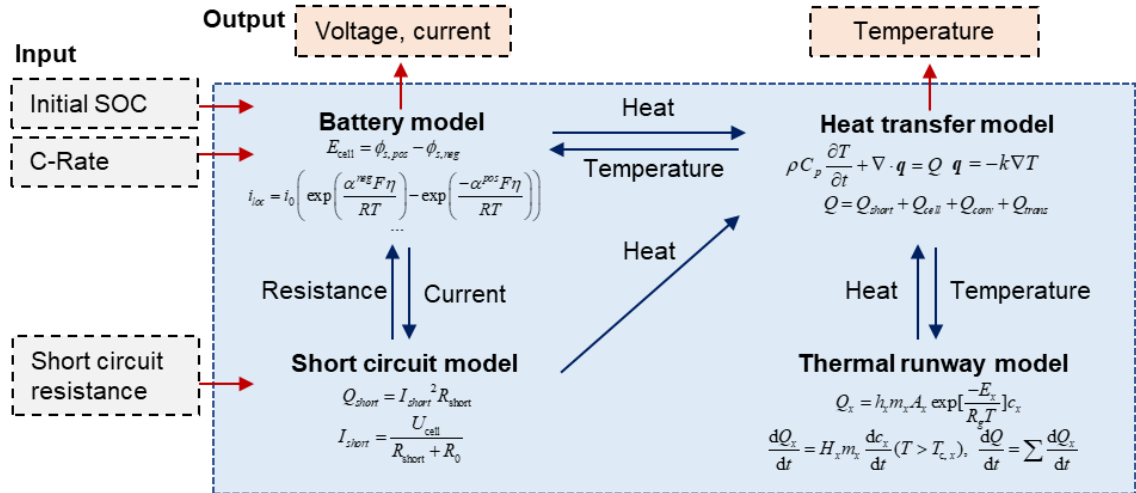


Figure 26 Framework of the multiphysics modeling.

Detailed equations and model setups are described in APPENDIX B. The multiphysics model is developed in the COMSOL Multiphysics software and validated by experimental data. Firstly, the battery model is validated by cycling tests under CC-CV setup at various C-rates. The simulation voltage curves match the voltage curve from experimental data at different C-rates (Figs. 27a-d). Secondly, the coupling model is validated by the ISC triggering tests. The simulation results can predict the voltage drop, corresponding temperature increase, and thermal runaway triggering behaviors (Figs. 27e-h).

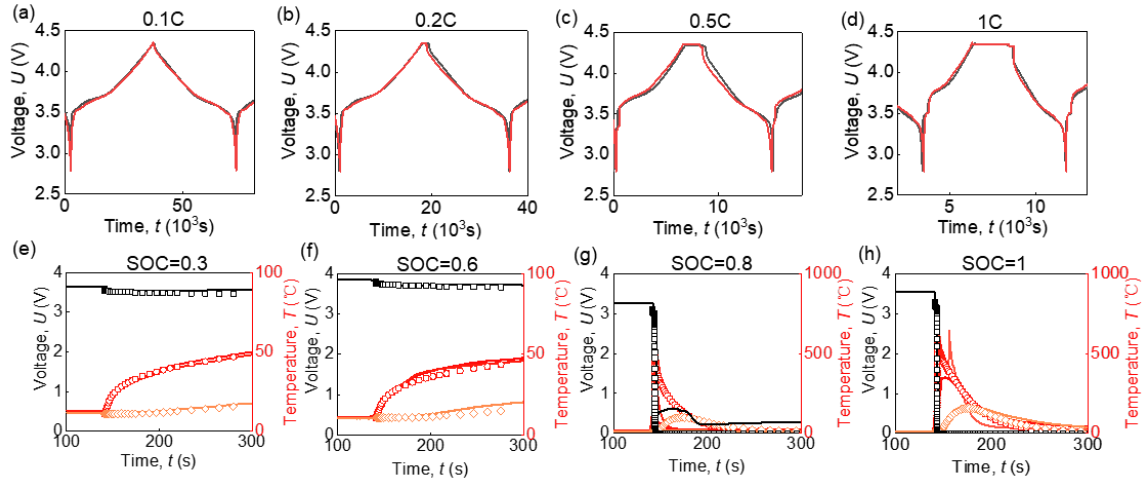


Figure 27 Multiphysics model validation. Validation of the battery model at different C-rates: (a) 0.1C; (b) 0.2C; (c) 0.5C; (d) 1C. Validation of the thermal transfer model at different SOC: (e) 0.3SOC; (f) 0.6SOC; (g) 0.8SOC; (h) 1.0SOC.

#### 4.1.3 Machine learning model development.

The Decision Tree (DT) and Support Vector Classifier (SVC) from the open-source library “scikit-learn” is used. According to training results, the classifiers C0 and C2 are DT based and the classifier C1 is SVC. For C0 and C2, The “gini” criterion is used. Considering that sample numbers from different groups are very different, a balanced class weight is used. For C1, regularization parameter is set as  $10^{-4}$  while kernel coefficient is set as  $10^{-4}$ . The hyperparameters were selected by 5-fold cross-validations to avoid overfitting. The training dataset contains samples that cover various cases with different short circuit resistances (Fig. 28).

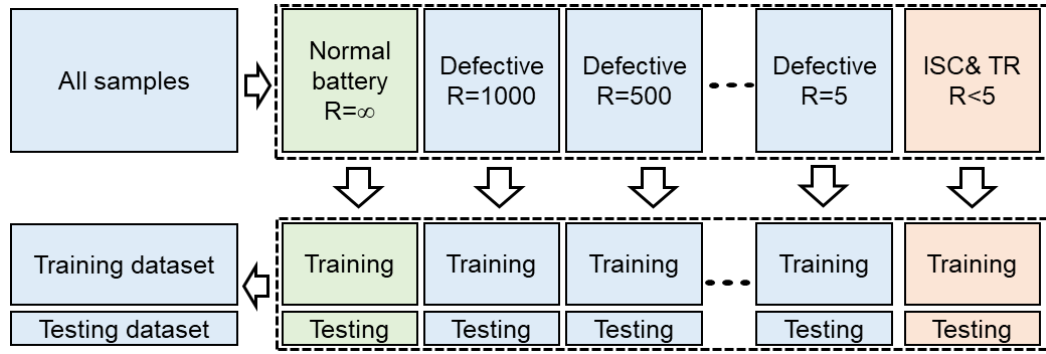


Figure 28 Datasets regroup process

## 4.2 Data generation and model development

### 4.2.1 Data generation process

Numerical calculation results are used in data generation. A numerical surrogate model was developed and was calibrated by the experimental tests (Fig. 29). The ISC triggering tests and cycling tests under different conditions are conducted to obtain the experimental data (detailed description see 4.1.1). The numerical model is then used to conduct the parameter sweep and generate the dataset that contains voltage and current series. According to the level of the safety risk, the cell states in this dataset were divided into four types: (1) Normal cells (L0); (2) Defective cells (L1); (3) Shorted cells without possible thermal runaway (TR) risk (L2); (4) Shorted cells with possible thermal runaway (L3). Based on the group definitions, argument vectors  $\mathbf{X}$  with labels  $Y \in \{G0, G1, G2, G3\}$  were generated via dividing and transferring the segments of the curves from the dataset. Features in  $\mathbf{X}$  were obtained from voltage/ current segments within a period (detailed description see 3.2.3). The training/ testing samples contain all generated samples ( $\mathbf{X}, Y$ ).

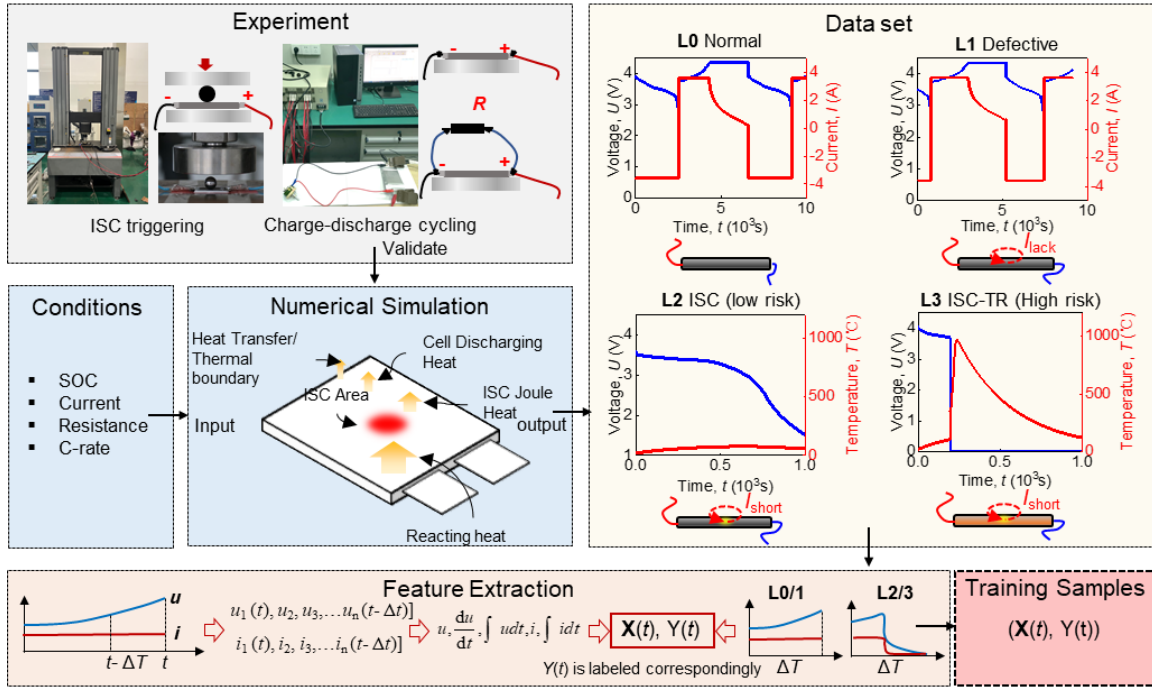


Figure 29 Data generation process.

#### 4.2.2 Multiphysics surrogate model and parametric calculation.

The numerical surrogate model is developed based on the multiphysics modeling technique (Fig. 26). The multiphysics model is validated by experimental data (Fig. 27). A parameter sweep is conducted to produce a sufficient amount of data. Initial SOC  $SoC_0$ , C-rate  $C_{rate}$ , and short circuit resistance  $R_{short}$  are set as inputs, while voltage-, current-, and temperature- time curves are outputs. For CC-CV charging/discharging cycling condition, the parameters change in the domain as:

$$\begin{cases} R_{short} = [10^6, 500, 200, 100, 50, 20, 10, 5] \Omega \\ C_{rate} = [2, 1.5, 1, 0.8, 0.6, 0.4, 0.2, 0.1] \end{cases}, \quad (22)$$

Here,  $R_{short} = 10^6 \Omega$  represents the normal case (L0). For each case, three CC-CV cycles is calculated (Fig. 30a). For short circuit triggering cases, the parameters are set as:

$$\begin{cases} SoC_0 = [1, 0.9, 0.8, 0.7, 0.6, 0.5, 0.4, 0.3, 0.2, 0.1] \\ C_{\text{rate}} = [2, 1.5, 1, 0.8, 0.6, 0.4, 0.2, 0.1, 0] \\ R_{\text{short}} = [5, 2, 1, 0.5, 0.2] \Omega \end{cases}, \quad (23)$$

For each case, the computation proceeds till the TR is triggered, or the temperature starts to decrease. (Fig. 30b).

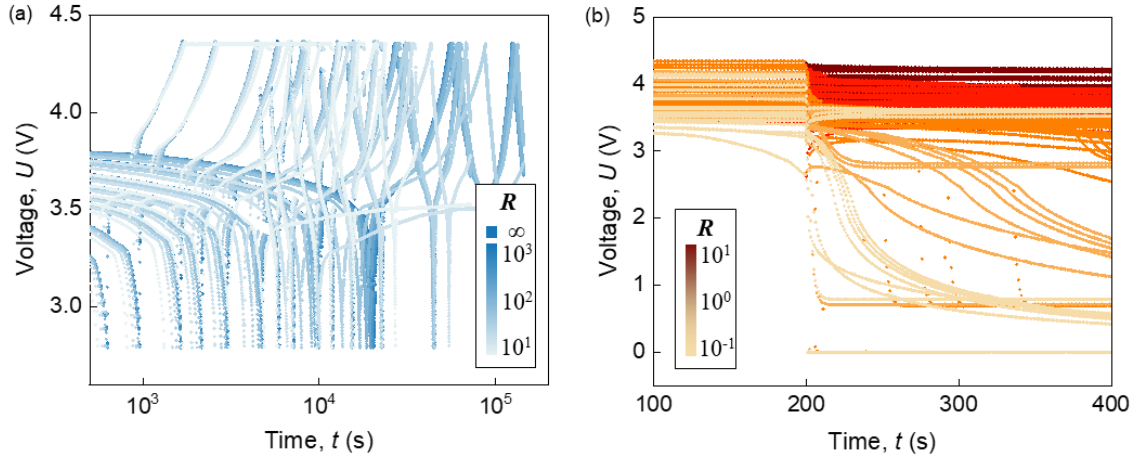


Figure 30 Parametric calculation results. (a) Results of the battery model at different C-rates and short circuit resistance; (e) Results of the coupling model at different initial SOC and short circuit resistances (dots represent data points).

#### 4.2.3 Feature selection and model structure design

The ML model should classify cell states into the defined four groups (L0~L3) based on features extracted from quantifiable parameters of the cell, such as voltage  $u$ , current  $i$ , temperature  $T$ , and inner pressure  $P$ . Among them,  $u$  and  $i$  can be measured accurately while  $T$  is very sensitive to boundary conditions, such as environmental temperature and the position of the sensor.  $P$  is only available in some cylindrical and prismatic batteries pack. Also, the abnormal cells can only be detected by their state (contains  $u$ , and  $i$ ) change rather than a single point. Thus, the model input should be features obtained from voltage  $u(t)$  and current sequence  $i(t)$  within a period  $\Delta t$ , where  $t$  is time. A general input matrix

is composed of  $u(t)$  and  $i(t)$ , along with their time derivative sequences  $\left. \frac{du}{dt} \right|_{t=t_i}$ ,  $\left. \frac{di}{dt} \right|_{t=t_i}$  and time integration sequences  $\int_{t_0}^{t_n} u dt$ ,  $\int_{t_0}^{t_n} i dt$ , where  $t_i, i = 0, 1, 2, \dots, n$  arithmetic progression and  $\Delta t = t_n - t_0$  (considering that the second derivative or integral is very sensitive to input error, only the first order is considered here):

$$X = \begin{bmatrix} u(t_0), u(t_1), \dots, u(t_n), \left. \frac{du}{dt} \right|_{t=t_0}, \left. \frac{du}{dt} \right|_{t=t_1}, \dots, \left. \frac{du}{dt} \right|_{t=t_n}, \int_0^{t_0} u dt, \int_0^{t_1} u dt, \dots, \int_0^{t_n} u dt, \\ i(t_0), i(t_1), \dots, i(t_n), \left. \frac{di}{dt} \right|_{t=t_0}, \left. \frac{di}{dt} \right|_{t=t_1}, \dots, \left. \frac{di}{dt} \right|_{t=t_n}, \int_0^{t_0} i dt, \int_0^{t_1} i dt, \dots, \int_0^{t_n} i dt \end{bmatrix}. \quad (24)$$

However, there is repeated information in the current input in Eq. (24) because the abnormal signal can be detected based on the state change between only two points. The maximum difference happens when the battery changes from the start state at  $t=t_0$  to the end state at  $t=t_n$ . Thus, the intermediate states are ignored. Also, constant current charge/discharge segments during the cycling are selected as input (for non-constant current cycling conditions, there are also many constant current segments.). In this case,  $\left. \frac{di}{dt} \right|_{t=t_i}$  ( $= \text{const} = 0$ ) terms are removed from the input. Thus, the input is rewritten as:

$$X = [u(t_0), u(t_0 - \Delta t), i(t_0), i(t_0 - \Delta t), \left. \frac{du}{dt} \right|_{t=t_0}, \left. \frac{di}{dt} \right|_{t=t_0 - \Delta t}, \int_{t_0 - \Delta t}^{t_0} u dt, \int_{t_0 - \Delta t}^{t_0} i dt], \quad (25)$$

where  $t_0$  is the current time and  $\Delta t$  is the selected period ( $t_0 - \Delta t$  is defined as the initial state,  $t_0$  is defined as the end state).

The voltage/ current sequences will be smoothed by a filter before feature extraction to avoid possible data noises (Savitzky-Golay is selected for tests, it can be replaced by

other efficient algorithms in a real application). Considering that obviously different value ranges between cases L0/1 and L2/3, while limited differences between L0 and L1 cases; therefore, a two-step classification structure with three classifiers is designed (Fig. 31). Here, the cells will be classified into L0/1 and L2/3 by classifier 0 (C0 judges if a short circuit occurs during  $\Delta t$ ). For L0/1, the battery states will be classified into L0 and L1 by Classifier 1 (C1 judges if the battery has damage). For L2/3, the battery safety states will be classified into L2 and L3 by Classifier 2 (C2 judges if a TR will happen under the current conditions). Note that two input vectors ( $\mathbf{X}_s(t)$  and  $\mathbf{X}_l(t)$ ) are generated at different time points (defined as Eq.25). Since parametric value differences between L2 and L3 or L0/1 and L2/3 are significant, it requires the determination of a possible short circuit to be quick. Thus,  $\mathbf{X}_s(t)$  is generated within a short period  $\Delta t_s$  and used for C0 and C2 (e.g., set as 1 min). On the contrary, the differences between L0 and L1 are trivial, and the differences need to be accumulated till they can be accurately detected. Thus,  $\mathbf{X}_l(t)$  is generated within a long period  $\Delta t_l$  and is only used for C1. Set as  $\Delta t_l=5$  min. It is worthy to note that  $\Delta t$  is not equal to the lag time of the prediction which means that the system needs a reference state at  $\Delta t$  before the current time point. As such,  $\Delta t$  can also be regarded as the necessary data collection time before the model can work. The lag time  $t_{lag}$  is dependent on the measuring frequency (1 Hz frequency in this study and 1s lag time in theory). Here, 293,990, 46,600, and 180,768 samples were generated and used in the training of C0, C1, and C2, respectively.  $\Delta t_s$  and  $\Delta t_l$  were selected as 1 min and 5 min. All four groups were

covered. The distributions of the selected features show that the value ranges of the two target groups are almost the same (Figs. 32-34). Thus, those classification problems cannot be solved based on a single threshold of one of the features.

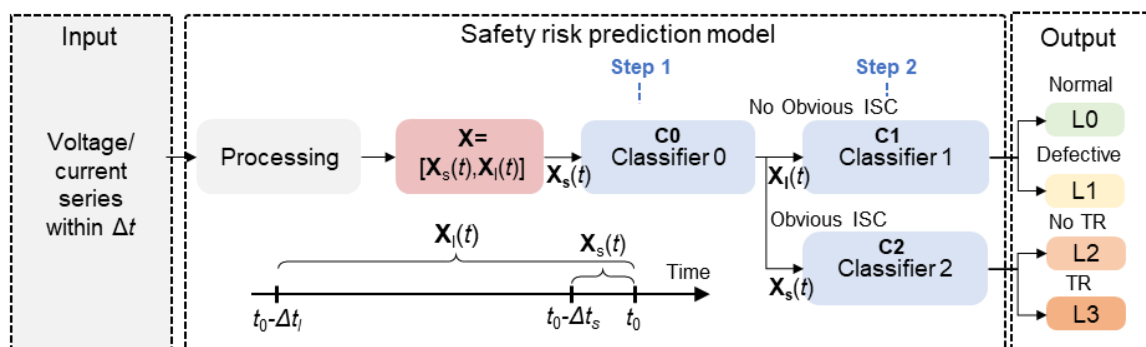


Figure 31 Fundamental model structure and training process of the ML classification model.

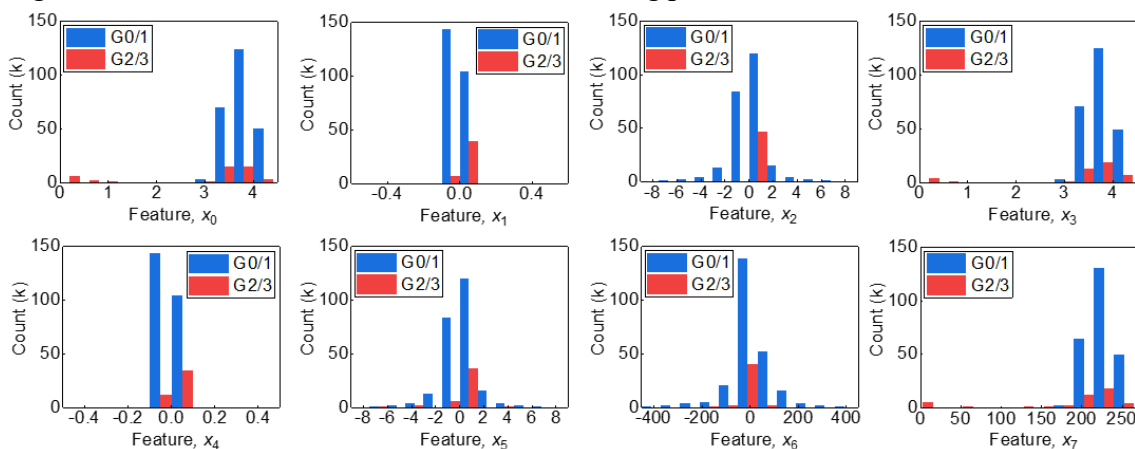


Figure 32 Feature distribution for C0

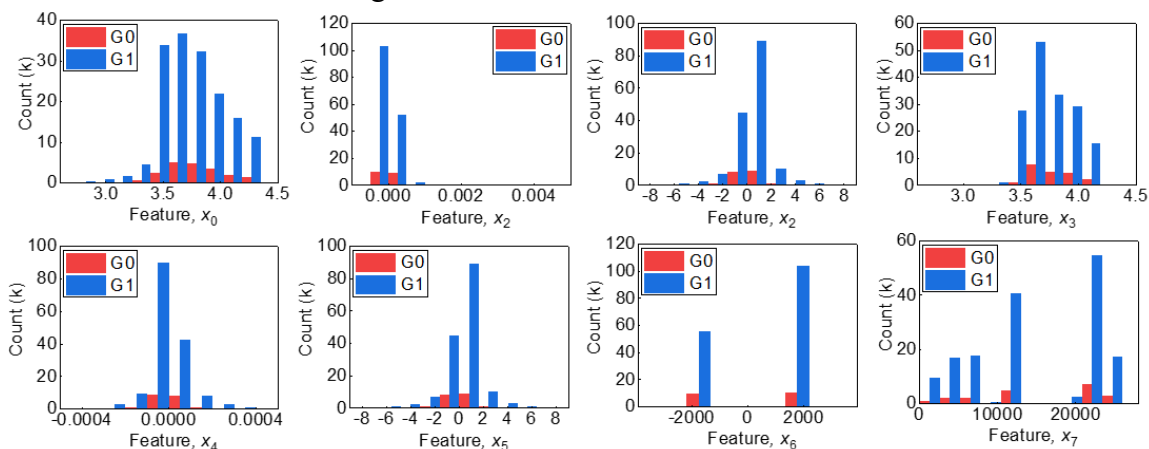


Figure 33 Feature distribution for C1

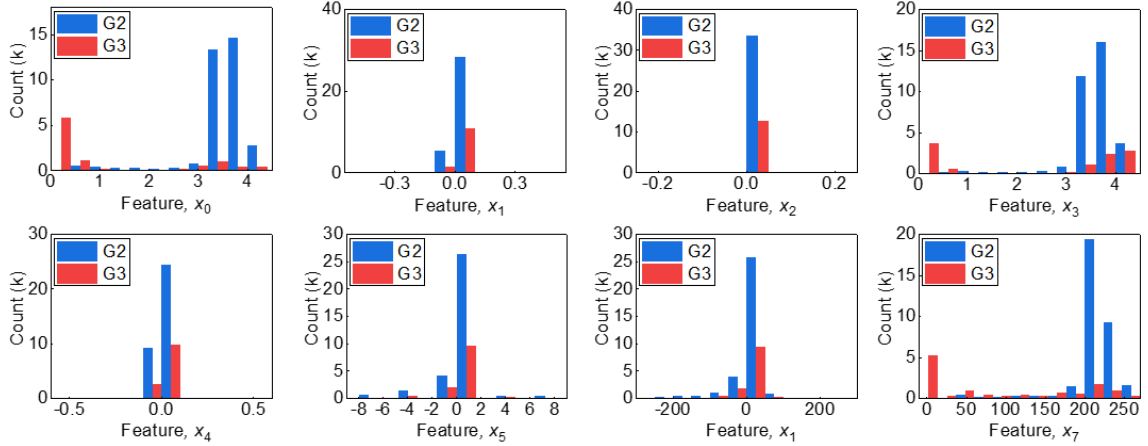


Figure 34 Feature distribution for C2

### 4.3 Predictive performance

#### 4.3.1 Model variants and computing setup.

For the three classifiers C0~C2, simple If/ else rule (expert heuristics), logistics regression (linear classification), k-Nearest Neighbors (k-NN) (non-linear classification), SVC, DT (tree-base), and Random Forest (RF) classifier selected as the candidate models. The models were developed based on python with the open-source library “scikit-learn”. For each classifier, 5 % of the samples will be used as test samples. The models were trained via 5-fold cross-validation based on Intel(R) Core (TM) i7-8550U CPU @ 1.80GHz, 2.00 GHz computing platform. The F1 score (calculate metrics for each label and find their unweighted mean) is used to indicate the classification performance. 5 random splits were conducted to obtain the mean prediction score and the corresponding deviation (Table 8). The mean value of F1 for each model indicates that the simple if/ else rule or linear classification model is not suitable. Thus, the safety risk state prediction is a classification problem. In this case, the selected feature is generally applicable to most nonlinear ML

models, such as Decision Tree, and RF. To achieve better performance and efficiency, DT was chosen for C0 and C2 while SVC was chosen for C1.

Table 8 Comparison between different classification models.

| Model                             | F1 score              |           |                    |           |                    |           |
|-----------------------------------|-----------------------|-----------|--------------------|-----------|--------------------|-----------|
|                                   | C0                    |           | C1                 |           | C2                 |           |
|                                   | Mean                  | Deviation | Mean               | Deviation | Mean               | Deviation |
| If/ else role<br>(baseline)       | 0.789161<br>( $x_2$ ) | 0.0001    | 0.566<br>( $x_1$ ) | 0.0004    | 0.884<br>( $x_0$ ) | 0.0002    |
| Logistic Regression<br>(baseline) | 0.818532              | 0.0027    | 0.469              | 0.0063    | 0.857              | 0.0034    |
| k-NN                              | 1.000                 | 0.0000    | 0.713              | 0.0052    | 0.986              | 0.0018    |
| Support Vector<br>Classifier      | 1.000                 | 0.0000    | 0.949              | 0.0038    | 0.985              | 0.0023    |
| Decision Tree                     | 1.000                 | 0.0000    | 0.931              | 0.0013    | 0.994              | 0.0019    |
| Random Forest                     | 1.000                 | 0.0000    | 0.934              | 0.0016    | 0.998              | 0.0005    |

#### 4.3.2 Performance of the classifiers.

The confusion matrix was used to evaluate the accuracy of classification (Table 9, Figs. 35a-c). In binary classification, the matrix consists of four elements: true negatives (TN), false negatives (FN), true positives (TP), and false positives (FP), where “positive” and “negative” represent the prediction results, and “true” and “false” represent whether that prediction is right. First of all, C0 can divide battery states into L0/1 and L2/3 without any deviation due to the obvious characteristics between ISC triggered and non-ISC cases (Table 9). For ISC cases, they usually have a voltage drop and current decrease accordingly. These differences can be easily detected by features such as  $u(t_0)$ ,  $u(t_0 - \Delta t)$  or  $i(t_0)$ ,  $i(t_0 - \Delta t)$ . C1 and C2 can also accurately classify non-ISC cases into L0 and L1 and classify ISC cases into L2 and L3, respectively (Table 9). For C2, the defective cells have a slightly

lower voltage or voltage slope due to the existence of current leakage. For C3, the case with thermal runaway (TR) always has certain distinctive features, such as high SOC, small short circuit resistance. Those differences reflect on the selected features (Detailed discussion see section 4.3.2). The accuracy of C1 is lower than the other two classifiers due to the small difference between L0 and L1. Receiver operating characteristic (ROC) curves can show the classification performance of the classifiers (Figs. 35d-f). In the meantime, the area under the curve (AUC, 0~1) can also be used to indicate the performance of the classifier. The AUC of C1 is almost 1 (Table 9). The AUCs of C1 and C2 are 0.99, very close to 1 (Table 9). Such results manifest satisfactory classification prediction results of the model.

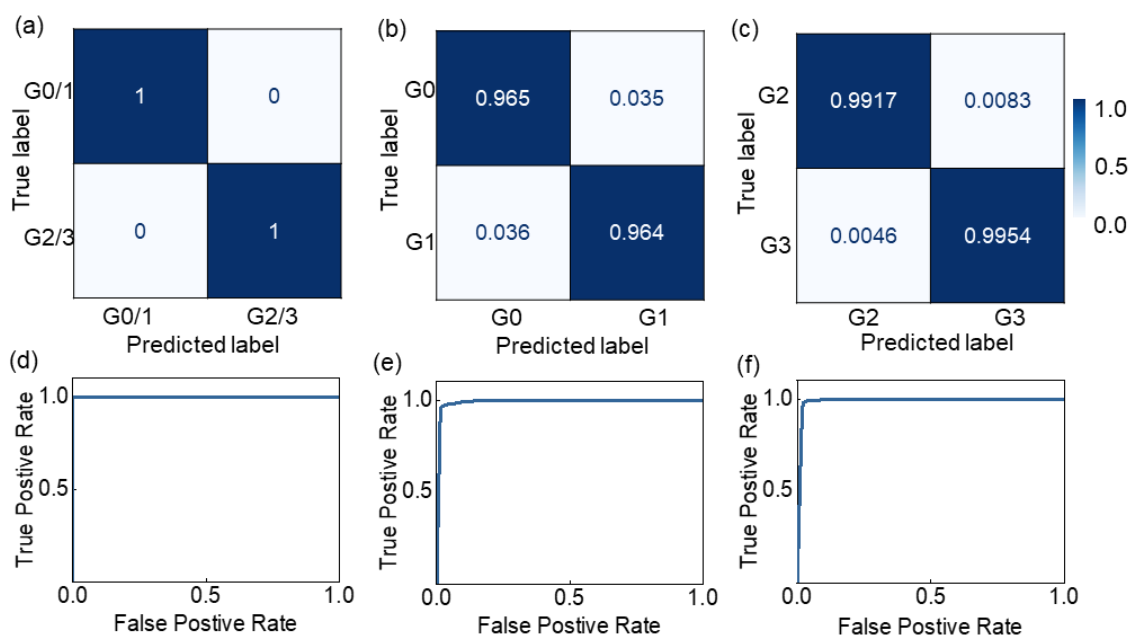


Figure 35 Validation and performance of the classification models. Confusion matrix of (a) C0;(b) C1; (c) C2 (horizontal labels represent prediction results, vertical labels represent their true labels, elements in the matrix present the ratio of samples with the predicted label in their true group). Receiver operating characteristic (ROC) curves (d) C0;(e) C1; (f) C2;

Table 9 Performance of the classification models.

| Classifier       | C0   |            |      | C1   |            |       | C2   |            |        |
|------------------|------|------------|------|------|------------|-------|------|------------|--------|
|                  | True | Prediction |      | True | Prediction |       | True | Prediction |        |
|                  |      | G0/1       | G2/3 |      | G0         | G1    |      | G2         | G3     |
| Confusion matrix | G0/1 | 1          | 0    | G0   | 0.965      | 0.035 | G2   | 0.9917     | 0.0083 |
|                  | G2/3 | 0          | 1    | G1   | 0.036      | 0.964 | G3   | 0.0046     | 0.9954 |
| F1 Scores        |      | 0.999      |      |      | 0.980      |       |      | 0.992      |        |
| AUC              |      | 1          |      |      | 0.991      |       |      | 0.995      |        |

Four typical scenarios were used to present the safety risk prediction process (Figs. 36): (1) Case 1: normal cell during 1C charging/discharging; (2) defective cell during 1C charging/discharging (cell with  $R = 60 \Omega$ ); (3) ISC is triggered during 0.1C charging (SOC=0.8,  $R = 2.2 \Omega$ , no TR); (4) ISC is triggered during 0.1C charging (SOC=0.9,  $R = 1.8 \Omega$ , TR). The model started collecting data when the charging or discharging started. After  $\Delta t_s$ , C0, C2 started working, the safety risks of those cases were L-1 (unknown). After  $\Delta t_s$ , C1 started working. The risk levels of all cases changed to from L-1 to L0 (the default level is L0 until a defect or a short circuit is detected). After  $\Delta t_i$ , the risk level of case 1 changed from L1 to L0, and the risk level of case 2 changed from L-1 to L0. The ISC of cases 3 and 4 were mechanically triggered at  $t=200s$ . Thus, the safety risk level of case 3 changed and is stable at L2, and the risk level of case 4 also changed from L0 to L3 before the TR triggering.

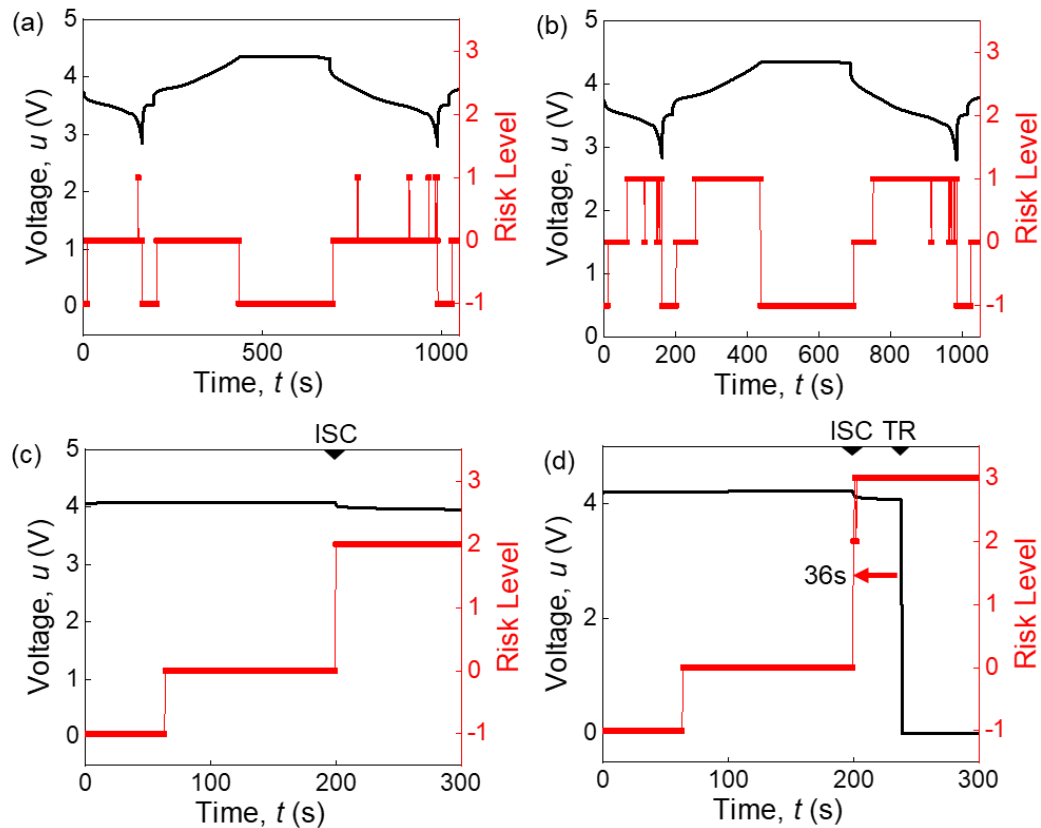


Figure 36 Prediction process demonstration. Prediction process of four scenarios: (a) L0, normal cell during 1C discharging; (b) L1, defective cell during 1C discharging; (c) L2, ISC is triggering during 0.1 C charging (TR is not triggered) (d) L3, ISC is triggering during 0.1 C charging (TR is not triggered) (Level=-1 means risk level is unknown).

Some typical methodologies of battery cell safety risk prediction are summarized and compared (Table 10). Among them, models for ESC detection have higher accuracy and lower response time because the short circuit current will directly influence the total current, which is directly measured by the sensor. Thus, the models have more information to make the decision. In terms of ISC detection, the theoretical/ empirical models can predict ISC in a reasonable accuracy with a short response time when  $R$  is relatively small; however, a longer preparation time is needed to achieve higher accuracy. The emerging ML models

can well predict cells with a larger resistance range, but the features are obtained from a complete cycle. This significantly limits the flexibility of the model prediction since the prediction can only be provided in a cycle-by-cycle manner. Our proposed model here uses a uniformed input to predict both ISC cells and defective (leakage) cells. Meanwhile, the model achieved a sweet spot of prediction accuracy and speed (short preparation time and response time).

Table 10 Comparison between typical methodologies of battery cell safety risk prediction.

| Methodologies                 | Refs                           | Principles   | Input/feature   | Output/Indicator  | Performance/Accuracy  |
|-------------------------------|--------------------------------|--|---|---|---|
| Theoretical / empirical model | Feng, X. et al. <sup>109</sup> | Equivalent circuit model (ECM) and recursive least squares (RLS) | $U, I, T$   | $R_2, C$ in ECM   | Good when $R \leq 20\Omega$   |
|                               | Seo, M. et al. <sup>120</sup>  | RC model and switching model method (SMM)                        | $U, I$  | $R$   | Relative error $\leq 14.2\%$ when $5\Omega \leq R \leq 50\Omega$  |
|                               | Xia, B. et al. <sup>121</sup>  | Empirical model  | $U, I, T$   | $dT/dt, U, I$   | Well detect ESC and 10% error in surface temperature  |
| Machine learning model        | Chen, Z. et al. <sup>122</sup> | SVM and lumped parameter model                                   | $C_d, T$  | $T_{max}$   | Accuracy $>76.7\%$ (after 10s) or 100 % (after 33s)   |
|                               | Yang, R. et al. <sup>123</sup> | RF (to enhance the RMSE threshold)                               | $C_d, T_{max}$  | leakage/ no leakage   | Well detect leakage of four cases   |
|                               | Naha, A et al. <sup>99</sup>   | RF and ECM   | $SOC_{max}, V_{cmin}, T_{cv}, E_L, Slope_{ocv}, a_1, R_i$ | leakage/ no leakage   | Accuracy $>99.2\%$ ( $150\Omega \leq R \leq 500\Omega$ )  |
|                               | Our method                     | RF, SVC, ECM and FE model  | $U, I, dU/dt, \int U dt, \int I dt$                       | Safety levels (Normal, damaged/ leakage, ISC (no TR or TR)) | For defective/ normal: accuracy $>93\%$ ( $5\Omega \leq R \leq 500\Omega$ )<br>For TR/ no TR accuracy $>99.8\%$ |

Continue

| Methodologies                 | Refs                           | Preparation time   | Response time  | Solved problems                  |
|-------------------------------|--------------------------------|--|--|----------------------------------|
| Theoretical / empirical model | Feng, X. et al. <sup>109</sup> | Depends on threshold selection, $10^2 \sim 10^3 \text{s}^*$  | $10^{-2} \text{s} \sim 10^0 \text{s}^*$<br>(Direct compare)    | ISC                              |
|                               | Seo, M. et al. <sup>120</sup>  | Depends on threshold selection, $10^2 \sim 10^3 \text{s}^*$  | $10^{-2} \text{s} \sim 10^0 \text{s}^*$<br>(Direct compare)    | ISC                              |
|                               | Xia, B. et al. <sup>121</sup>  | $10^{-1} \text{s}^*$   | $10^{-1} \text{s}$ for ESC;<br>$10^2 \text{s}$ for temperature | ESC                              |
| Machine learning model        | Chen, Z. et al. <sup>122</sup> | $10^2 \text{s}$  | $10^{-2} \text{s} \sim 10^0 \text{s}^*$                        | ESC                              |
|                               | Yang, R. et al. <sup>123</sup> | $10^2 \text{s}^*$<br>(to capture $T_{\max}$ )  | $10^{-2} \text{s} \sim 10^0 \text{s}^*$                        | ESC                              |
|                               | Naha, A et al. <sup>99</sup>   | 1 cycle ( $10^3 \text{s} \sim 10^4 \text{s}$ )   | $10^{-2} \text{s} \sim 10^0 \text{s}^*$                        | ISC                              |
|                               | Our method                     | For damaged/ normal classification:<br><b><math>10^2 \sim 10^3 \text{s}</math></b> ; For TR/ no TR classification: <b><math>10^1 \sim 10^2 \text{s}</math></b> . | $1.5 \times 10^{-2} \text{s}$                                  | Safety levels (both ISC and ESC) |

### 4.3.2 Feature importance analysis

Feature importance indicates how useful the selected features are in a predictor. Permutation importance was used to analyze the feature importance of group L0/1 (C1) and group L2/3 (C2) (Fig. 37). The permutation importance is a general approach that reflects the feature importance in the decrease in prediction score when each feature value is randomly shuffled. For C1, most of the features contribute to the final prediction results. We discover that voltage slope  $du/dt|_{t=t_0}$ ,  $du/dt|_{t=t_0-\Delta t}$ , voltage  $u(t_0)$ ,  $u(t_0 - \Delta t)$ , and voltage integration  $\int_{t_0-\Delta t}^{t_0} u dt$  have larger feature importance since they are highly related to leakage current or leakage capacity (Fig. 37a and 37b) (APPENDIX C). For C2:  $u(t_0)$  and  $du/dt|_{t=t_0}$  exhibit larger feature importance (Fig. 37c and 37d). Those features contain the information of initial *SOC* (or voltage) and *R* which determines the short circuit current  $i_{short}$  (APPENDIX C). Thus, for defective cell detection (C1), voltages/ voltage slopes from both the initial state ( $t_0 - \Delta t$ ) and the end state ( $\Delta t$ ) have significant contributions, which means voltage measurement accuracy should be satisfied (further discussed in Section 4.3.3). For the prediction of TR cases (C2), the key to the problem is to capture the voltage/ voltage slope after the voltage drop.

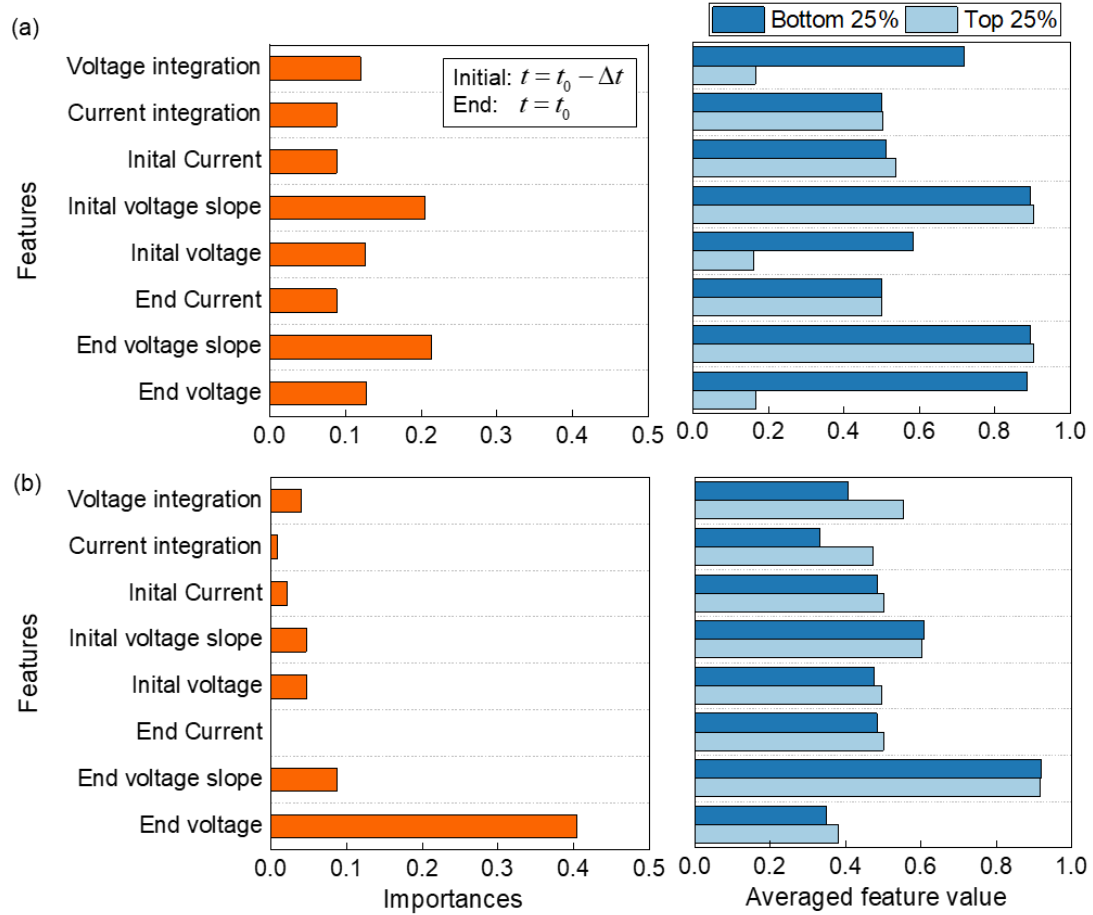


Figure 37 Feature importance analysis of classifiers C1 and C2. Feature importance based on permutation method and crosstab for selected features under top 25% sample (averaged feature values of  $X$  in tests samples with top or bottom 25% possibility given by the classifiers): (a) C1 (b) C2.

#### 4.3.3 Robustness analysis.

We consider the current and voltage measurement deviations to analyze the robustness of the model. Here, the deviations are described as Gaussian white noises (the input curve is unsmooth). The results indicate that the prediction score (weighted F1 score) is almost insensitive to the current error  $i_e$  (Fig. 38a). The score starts to decrease slightly only when the deviation is larger than  $10^2$  mA. In terms of voltage deviations  $u_e$ , the prediction

score drops drastically when  $u_e$  is larger than  $10^{-1}$  mV (Fig. 38b). Such phenomena can be explained by analysis of the order of magnitude (APPENDIX C). However, the score is still greater than 0.9 when  $u_e$  is  $10^0$  mV. For current error, the accuracy will only be affected when the order of magnitude of  $i_e$  is close to  $i$ . For current error, the accuracy will be significantly affected when the order of magnitude of  $u_e$  is larger than about  $10^{-5}$  V (  $10^{-2}$  mV). Because of the filter and multiple features, the accuracy can remain satisfactory till  $u_e = 10^{-3}$  V ( $10^0$  mV).

#### 4.3.4 Impact of input period and short circuit resistance range.

According to the feature importance analysis and the order of magnitude of the important features, we know that the model prediction accuracy is related to  $\Delta t$  selection and short circuit resistance range  $[R_{\min}, R_{\max}]$  (mainly for the maximum resistance).  $R$  is dominated by the ISC mode. A minor ISC (usually leads to defects) does not include Cu-Al contact (may only include Cu (Cu collector)-An (Anode), Al (Al collector)-Ca (Cathode) or An-Ca contact), the area resistance  $RA \in [122, 300] \Omega \cdot \text{mm}^2$ . A major ISC (usually leads to instant non-recoverable voltage drop) includes Cu-Al contact,  $RA \in [4, 50] \Omega \cdot \text{mm}^2$ . Considering a common contact area  $A$  ranges from  $10^0$  to  $10^1 \text{ mm}^2$ , thus  $R$  for a minor ISC is  $\in [12, 300] \Omega$  while for a major ISC  $\in [0.4, 50] \Omega$ <sup>19</sup>. Here, C1 is taken as an example, and  $\Delta t_i$  from 1 min to 20 min was used, and  $R_{\text{short}}$  from  $10^0 \Omega$  to  $10^3 \Omega$  (for the defective cells, covers the range for minor ISC) are selected. In terms of different  $\Delta t_i$ , the results show that an extended  $\Delta t_i$  can effectively improve the

prediction score, especially for cases with larger voltage error (Fig. 38c). This is because the difference  $\delta$  is positively related to  $\Delta t_l$  (APPEBDIX C). Furthermore, the prediction score decreases when  $R_{\max}$  increases (Fig. 38d) because  $\delta$  is also proportional to  $1/R$  according to Eq. C10. So the increase of  $R$  shrinks the difference between the normal state and the damaged state. These results reveals that defective cells with a relatively large short circuit resistance are still detectable even with a certain degree of measurement error.

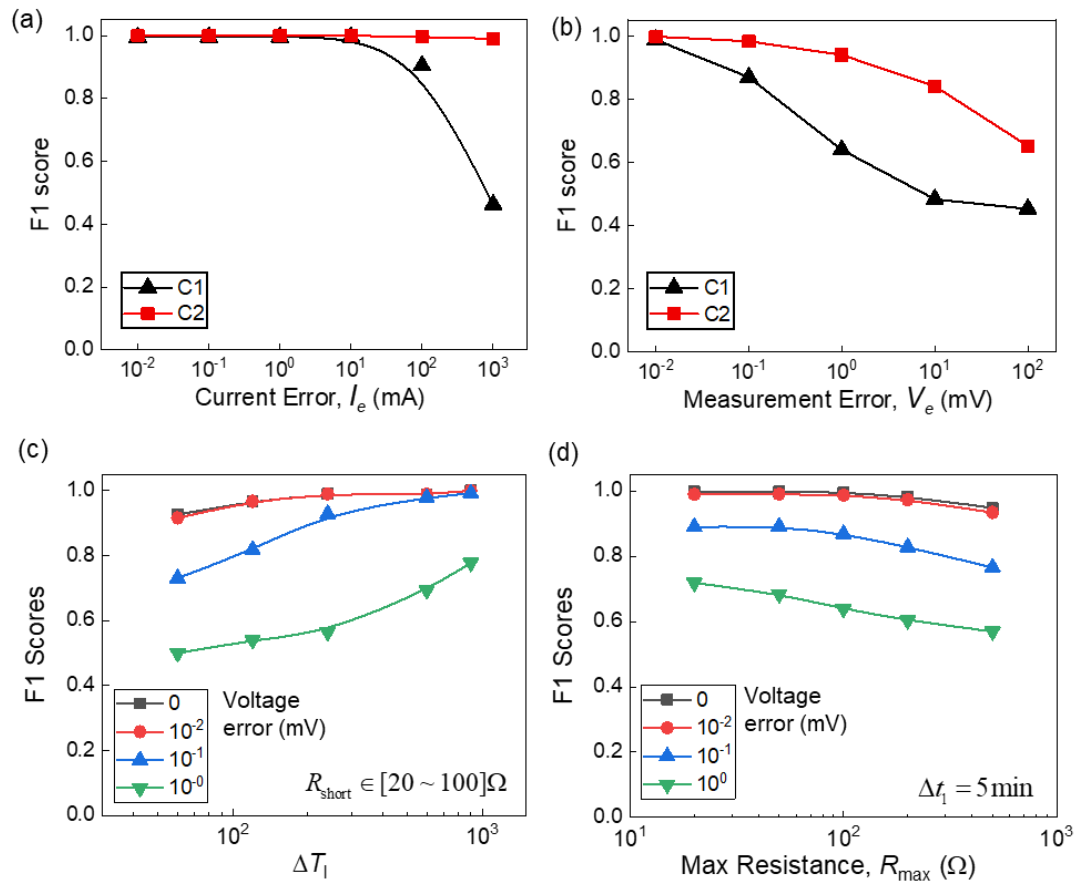


Figure 38 Performance analysis of classifiers. Robustness: Prediction score of classifiers C1 and C2 with (a) current error ( $u_e=0$  mA) and (b) voltage error ( $i_e=0$  mA).  $\Delta t_s$  is set as 1 min and  $\Delta t_l$  is set as 5 min; Effects of period selection and resistance range on

prediction accuracy: Prediction scores when (c) normalized period increase and (d) max resistance of damaged batteries increases.

#### 4.4 Conclusions

Online safety risk evaluation of LIBs cell is a proactive methodology to minimize and mitigate possible losses due to battery safety issues. Here, we defined four safety risk levels according to experimental results and developed a machine-learning battery safety risk classification model. Our proposed method can accurately predict the safety risk level of the LIBs during cycling conditions in an efficient fashion. With the assist of numerical simulation, about  $3 \times 10^5$  training samples have been generated, covering common SOC, short circuit resistance, and C-rate ranges. The model demonstrated a satisfactory performance (F1 score  $> 0.93$ ) and robustness (prediction scores  $> 0.87$  with a voltage error of 0.1 mV). From the feature importance analysis of the model, we found that the initial voltage slope and the initial voltage slope have relatively larger importance in normal/detective cells classification and the end voltage has larger importance in TR/ non-TR cells classification. From the robustness analysis, we discovered that voltage error has a larger impact on prediction accuracy. Further parametric analysis indicates that the prediction accuracy would decrease when the maximum short circuit resistance increases and would be improved when the period  $\Delta t$  is extended. The methodologies were validated by pure experimental data. The model achieves the expected accuracy in simulation analysis.

The limitation of current ML model is that we do not consider the capacity loss since the variables increase significantly due to the coupling of features caused by capacity loss

and safety issues. In addition, consideration of the capacity loss may require at least one prior complete cycle data which is impossible for short-time prediction.

The simplicity of the proposed ML architecture makes it possible to implement it in hardware as a smart battery monitoring system. In principle, a cell can be instrumented with readily available voltage/current sensors and related signal conditioning hardware to provide a time series of measurements to a microprocessor. The microprocessor can be programmed to numerically differentiate and integrate these signals and then pass them through a (trained) neural network model with known weights. Last, a sensor interface protocol could be established to output the classified battery state and other relevant information (*e.g.*, via serial communication) to a downstream display or other devices. Our results showcase the power of the machine-learning classification model and provide an innovative solution for the identification of the battery safety risks and next-generation online battery safety monitoring system.

## CHAPTER 5 SAFETY RISKS OF MECHANICAL DEFECTIVE LITHIUM-ION BATTERIES

In this chapter, we focus on the safety issues of defective batteries, especially aiming at the electrochemical performance, thermal safety, and mechanical integrity of the battery. Inspired by real-world smartphone maintenance accidents, i.e., a screw penetration method is used to introduce the defect where a small screw is placed sideways on, and pressed into the face of a prismatic cell. Such a phenomenon is also representative of possible foreign object penetration for batteries in electric vehicles or other mechanical systems. The defect batteries are then characterized both electrochemically and mechanically to discuss the consequent ISC and thermal runaway triggering behaviors and modes. Safety risks of defective batteries that do not undergo thermal runaway are evaluated by comparing their electrochemical and thermal behavior with normal batteries and discussed to demonstrate the underlying mechanism. Furthermore, possible defective battery detection and identification methodologies are developed and summarized.

### 5.1 Methods

#### 5.1.1 Manufacture of a defective battery.

One of the most common battery defect/damage is the foreign object intrusion during working or repairing. Herein, the screw indentation is employed as a way to “fabricate” defective batteries. Such mechanical abusive loading is an effective methodology to introduce a local short-term short circuit in a more controllable and experimentally

repeatable way and can represent all sorts of scenarios that cause the same local short circuit cases, *e.g.*, small particles penetrating the battery layers during assembling. A widely available screw with a head size of 2 mm and a total length of 3 mm was used (Fig. 39). The screw was laid horizontally on a pouch cell with a size of 84×64.5×3.5 mm. The basic information of the battery is presented in Table 11. Inside the Al plastic film battery pouch, 12 layers of the cathode (collector with active material on both sides), 12 layers of the anode (collector with active material on both sides), and 24 layers of separator are rolled into a jellyroll. The 1C CC-CV curves of three batteries agree well with each other for the chosen batteries (Fig. 40). A flat indenter on the mechanical testing machine INSTRON 2345 applied to push force to indent the screw into a cell with SOC=0.5 at a speed of 6 mm/min.

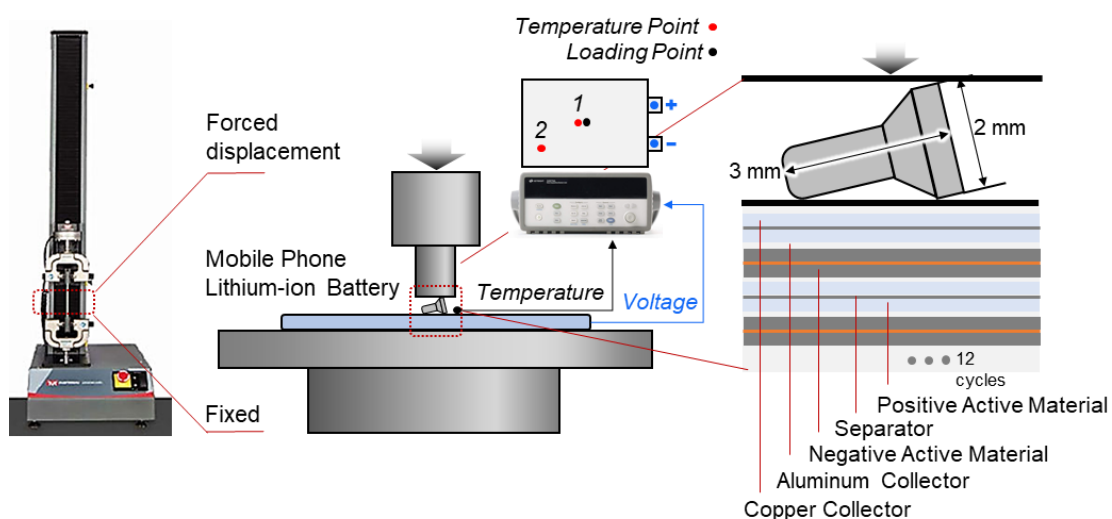


Figure 39 Schematic diagram of the screw indentation experiment.

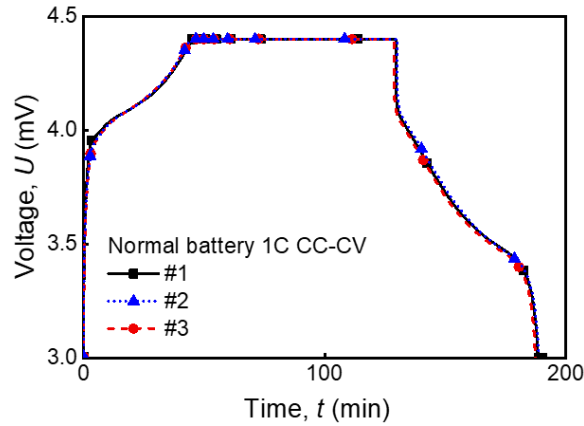


Figure 40 1C CC-CV voltage-time curve for cell used during the screw indentation.

Table 11 Basic information about battery samples.

| Parameters                 | Value              |
|----------------------------|--------------------|
| Nominal capacity           | 3.350 Ah           |
| Charging cutoff voltage    | 4.4 V              |
| Discharging cutoff voltage | 3.7 V              |
| Cathode material           | LiCoO <sub>2</sub> |
| Anode material             | LiC <sub>x</sub>   |
| Separator material         | PP                 |
| Cathode collector material | Al                 |
| Anode collector material   | Cu                 |
| Al plastic film            | Al plastic film    |
| Layer number               | 24                 |

### 5.1.2 Electro-chemo-thermal coupling model.

The defect introducing process is simplified into a local short-circuit, electrochemical-thermal coupling process. An Electro-chemo-thermal coupling model was established to numerically analyze the underlying behaviors of defective batteries. The model consists of a 1-D lithium-ion battery model<sup>83-85</sup>, short-circuit model thermal model<sup>43, 87, 88</sup>, and chemical reaction model<sup>48</sup>. The coupling strategies are shown in Fig. 41a. The battery model verified by discharging voltage-time curves at different rates from 0.1C to 2C is

used to calculate battery potential. The simulation results match the experimental voltage curves well (Fig. 42a). To simulate the short-circuit and recovery processes, a short-circuit resistance – time relationship is set as:

$$R_{\text{short}}(t) = \begin{cases} R_{\text{short}0} & (t \leq 0) \\ R_{\text{short}1} & (0 < t < t_1) \\ R_{\text{short}2} & (t_1 < t) \end{cases}, \quad (26)$$

where  $R_{\text{short}0}$  should be an infinite large short-circuit resistance to represent the state that short circuit has not triggered) (here it is set as  $10^5 \Omega$ ),  $R_{\text{short}1} = 0.08 \Omega$  is the transient short-circuit resistance before the voltage recovery, and  $R_{\text{short}2} = 700 \Omega$  is the stable short-circuit resistance after the voltage recovery. The resistance  $R_{\text{short}1}$  is estimated by the equation:

$$R_{\text{short}1} = \frac{U_1}{U_0 - U_1} R_0, \quad (27)$$

where  $U_0$  is the initial open-circuit voltage (OCV),  $U_1$  is the voltage during the discharging, which can be considered as a constant due to the short discharging duration, and  $R_{\text{short}0}$  is the internal resistance (can be considered as ohm internal resistance). The resistance  $R_{\text{short}2}$  is estimated by the leakage current of the defective battery without external loading, written as

$$R_{\text{short}2} = U_{\text{ocv}}(t) \left( \frac{\Delta C(U_{\text{ocv}}(t))}{\Delta t} \right)^{-1}, \quad (28)$$

where  $U_{\text{ocv}}(t)$  is the OCV,  $\Delta C/\Delta t$  is the leakage current. The short-circuit joule heat and battery internal resistance joule heat is set as two heat sources for the model. The joule heat is calculated by Ohm's law and Joule's law. The chemical reaction and material phase

change are calculated based on the Arrhenius equation shown in Table 12. The constant values used are summarized in Table 16. Meanwhile, an axisymmetric 2-D model is developed to take advantage of the symmetry (Fig. 41b). The battery components are modeled in detail. A 10-mm radius area around the short-circuit point is considered. The heat source and boundary conditions setup are shown in Fig. 41b. The thermal convection and thermal radiation are considered on the upper surface of the battery domain. The model is calibrated by experimental results (voltage and temperature curves in Fig. 42b).

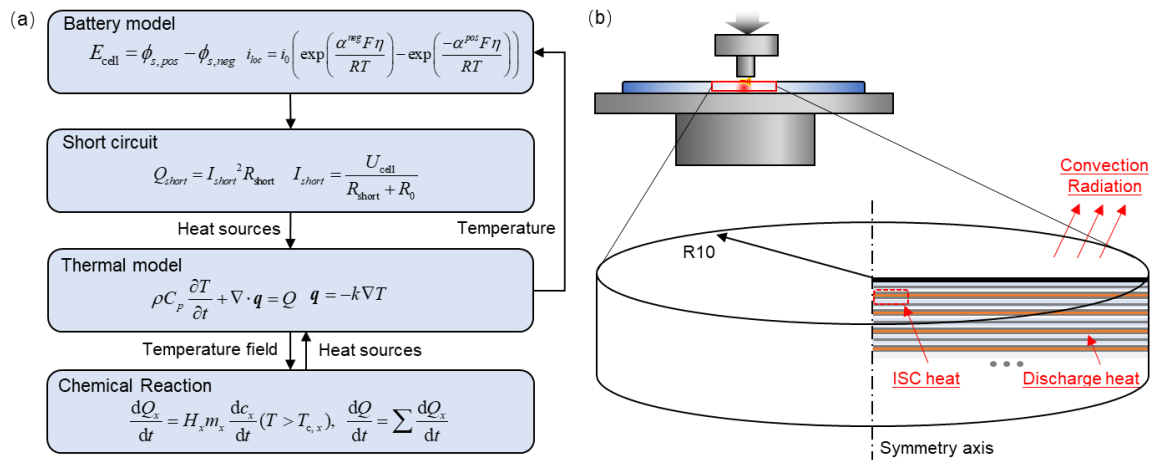


Figure 41 Modeling of the multi-physics model. (a) Coupling strategies. (b) geometry, boundary conditions, and heat source setting of the model. The ISC heat is produced by ISC resistance, the discharging heat is produced by the internal resistance. The convection cooling is considered.

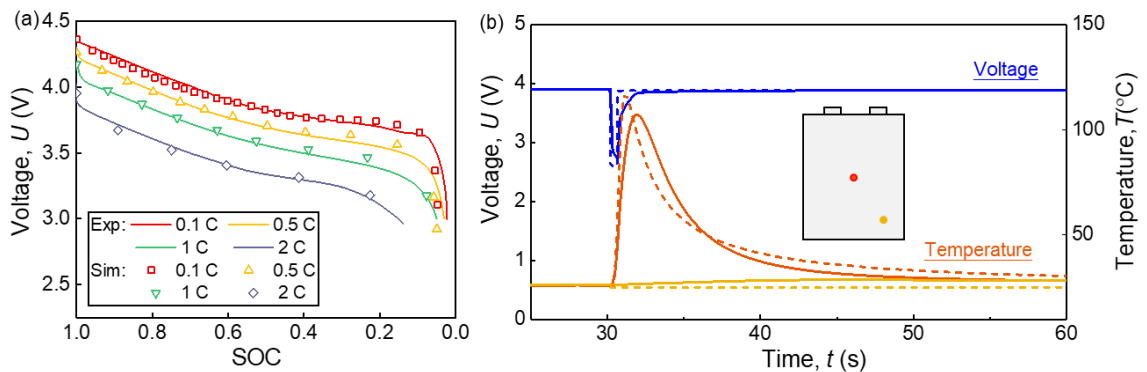


Figure 42 Validations of the sub-models within the multiphysics coupling model. (a)

Battery model. Comparison of discharging voltage curves at different rates between simulation and experiment; (b) Electrochemical-thermal coupling model. Comparison of voltage, temperature curve after the onset of the ISC during the screw penetration loading.

Table 12 Equations for chemical reaction and phase change.

| Reaction/ phrase change                        | Equations   |
|--|---|
| SEI decomposition                              | $Q_s = h_s m_a A_s \exp\left(\frac{-E_s}{R_g T}\right) c_s$ $\frac{dc_s}{dt} = -A_s \exp\left(\frac{-E_s}{R_g T}\right) c_s$ $\frac{dc_a}{dt} = -A_a \exp\left(\frac{-z}{z_0}\right) \exp\left(\frac{-E_a}{R_g T}\right) c_a$ |
| Anode–electrolyte reaction                     | $Q_a = h_a m_a A_a \exp\left(\frac{-z}{z_0}\right) \exp\left(\frac{-E_a}{R_g T}\right) c_a$ $\frac{dz}{dt} = -A_a \exp\left(\frac{-z}{z_0}\right) \exp\left(\frac{-E_a}{R_g T}\right) c_a$                                    |
| Cathode–electrolyte reaction                   | $Q_c = h_c m_c A_c \alpha_c (1 - \alpha_c) \exp\left(\frac{-E_c}{R_g T}\right)$ $\frac{d\alpha_c}{dt} = A_c \alpha_c (1 - \alpha_c) \exp\left(\frac{-E_c}{R_g T}\right)$  |
| Electrolyte decomposition reaction             | $Q_e = h_e m_e A_e \exp\left(\frac{-E_e}{R_g T}\right) c_e$ $\frac{dc_e}{dt} = -A_e \exp\left(\frac{-E_e}{R_g T}\right) c_e$  |
| Melting of the separator and current collector | $\frac{dc_s}{dt} = -A_s \exp\left(\frac{-E_s}{R_g T}\right) c_s$ $\frac{dc_{cc}}{dt} = -A_{cc} \exp\left(\frac{-E_{cc}}{R_g T}\right) c_{cc}$   |

Table 13 Values used in the equations for chemical reaction and phase change.

| Parameters | Value                        |
|------------|------------------------------|
| $A_c$      | $6.667 \times 10^{13}$ (1/s) |
| $A_e$      | $5.14 \times 10^{25}$ (1/s)  |

|               |                              |
|---------------|------------------------------|
| $A_s$         | $1.667 \times 10^{15}$ (1/s) |
| $A_a$         | $2.5 \times 10^{13}$ (1/s)   |
| $A_{sep}$     | $2.5 \times 10^{28}$ (1/s)   |
| $A_{cc}$      | $2.5 \times 10^{30}$ (1/s)   |
| $c_{s0}$      | 0.15                         |
| $\alpha_{c0}$ | 0.04                         |
| $c_{a0}$      | 0.75                         |
| $c_{e0}$      | 1                            |
| $c_{sep0}$    | 1                            |
| $c_{cc0}$     | 1                            |
| $z_0$         | 0.033                        |
| $E_a$         | $1.35 \times 10^5$ (J/mol)   |
| $E_c$         | $1.39 \times 10^5$ (J/mol)   |
| $E_s$         | $1.35 \times 10^5$ (J/mol)   |
| $E_e$         | $2.74 \times 10^5$ (J/mol)   |
| $E_{cc\_cu}$  | $7.2 \times 10^5$ (J/mol)    |
| $E_{cc\_al}$  | $5.1 \times 10^5$ (J/mol)    |
| $E_{sep}$     | $2.5 \times 10^5$ (J/mol)    |
| $h_a$         | 1714 (J/g)                   |
| $h_c$         | 400 (J/g)                    |
| $h_s$         | 257 (J/g)                    |
| $h_e$         | 155 (J/g)                    |
| $m_c$         | 610.4 (kg/m <sup>3</sup> )   |
| $m_a$         | 1221000 (kg/m <sup>3</sup> ) |
| $m_e$         | 406.9 (kg/m <sup>3</sup> )   |

---

### 5.1.3 Mechanical test for safety evaluation.

Three types of common mechanical tests, including local compression, bending, and free-drop, were designed to evaluate the mechanical safety level of defected lithium-ion batteries (Fig. 43) along with normal batteries for comparison. During the loading process, the OCV and surface temperature of batteries were measured *in-situ*. For compression tests, the battery was placed on the platen of the material test machine Instron 2345, a 10 mm diameter cyclical indenter moved downward at a speed of 6 mm/min (Fig. 43a). In the

three-point bending test, the battery was placed on the fixture with a span of 60 mm. A 10-mm-diameter cyclical upper anvil moved downward with a speed of 6 mm/min (Fig. 43b). For the free-drop test, a drop test machine was used to conduct the test (Fig. 43c). The initial height was set as 1.6 m.

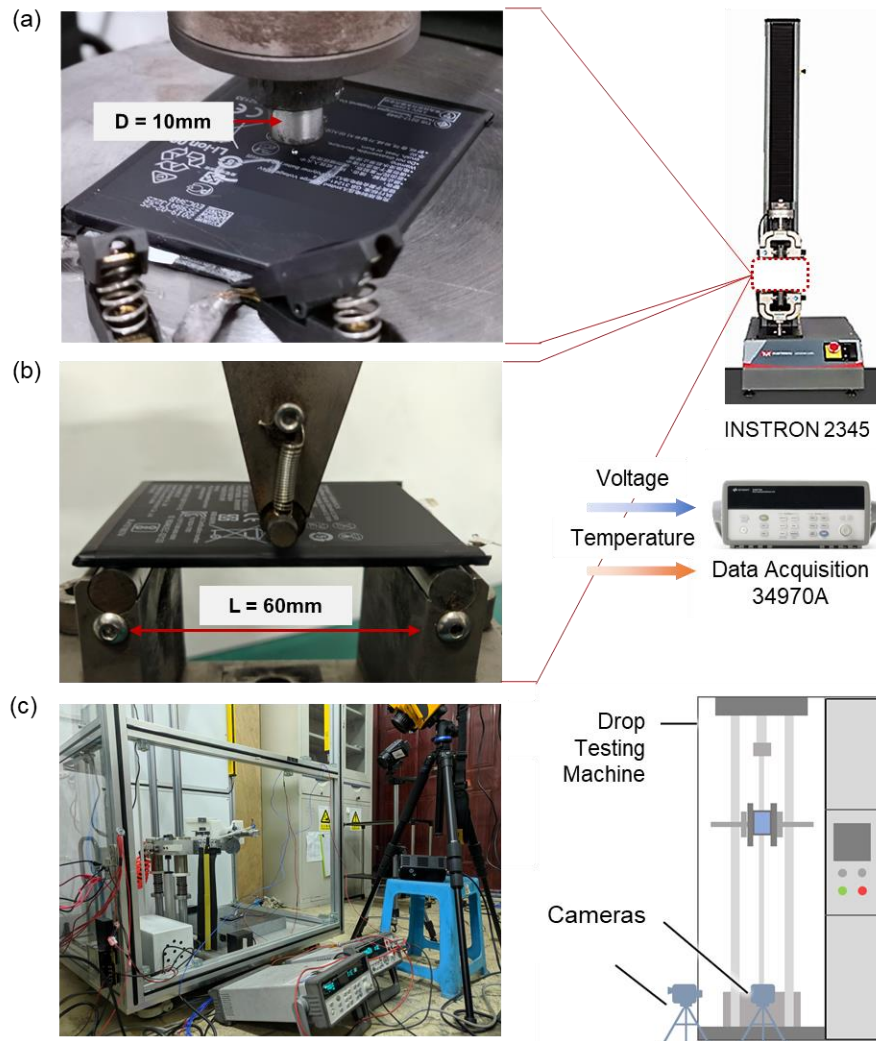


Figure 43 Experiment Methods. (a) Particle indentation, the diameter of the indenter is 10 mm, the loading rate is 2 mm/min; (b) 3-point bending, the span is 60 mm, the loading rate is 2mm/min. The indentation and 3-point bending experiment were conducted on an INSTRON 2345. (c) 160 mm free drop, a smartphone drop test machine was used. The voltage (OCV) and temperature (K-type thermocouple) signals are measured by a 34970A data acquisition.

#### 5.1.4. Mechanical finite element model.

The FE mechanical model is developed based on ABAQUS. The battery is homogenized into a cuboid. Through the compression test and three-point bending test of normal batteries, the elastic modulus and material constitutive of the battery material is characterized (Fig. 44). The out-of-plane elastic modulus  $E_{33} = 580$  MPa is obtained by the compression test and the in-plane elastic modulus  $E_{11} = E_{22} = 2370$  MPa. The plastic is set as isotropic. The nominal stress-plastic strain curve is calculated by the force-displacement curve of the compression test. The yield stress is set as 1MPa. The boundary conditions and loadings are identical to the experimental design, including compression (Fig. 45a), three-point bending (Fig. 45b), and free-drop test (Fig. 45c). The screw is simplified into the combination of two cylinders. According to the experiment, the geometry of the defective battery equals the cuboid subtracts part of the screw. The embedding depth is about 1 mm (Fig. 45d). Considering the elastic modulus of the screw is orders-of-magnitude larger than the battery, it is then considered as a rigid body. The screw and the battery are fixed together. The numerical calculation results show that the model simulates the mechanical behaviors of both defected and normal batteries under various loadings well (Fig. 46).

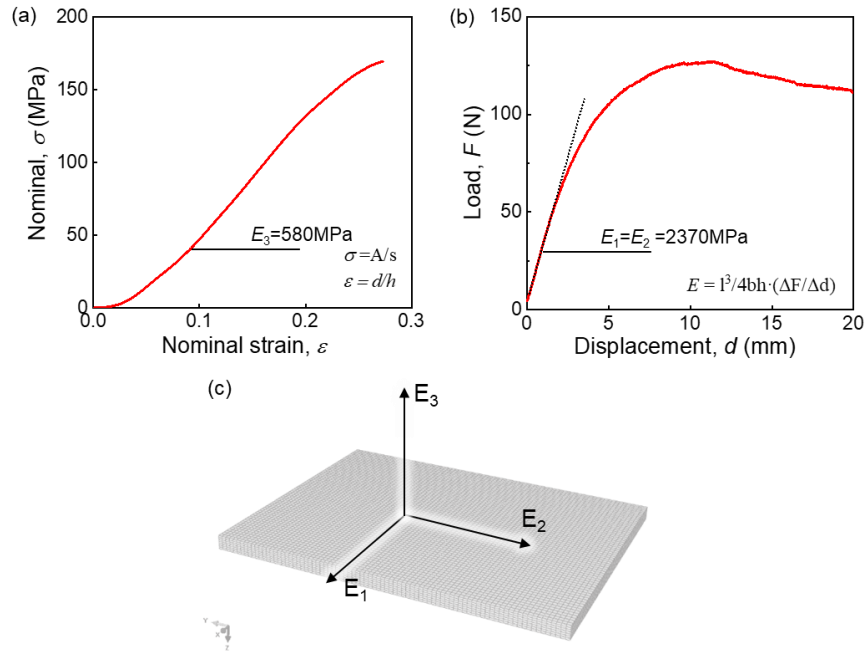


Figure 44 Material properties for the battery model. The model used here is an anisotropic elastoplastic homogenous model. (a) Constitutive relationship obtained by out-of-plane compression test; (b) In-plane elastic modulus estimated by three-point bending; (c) Material coordinate system definition.

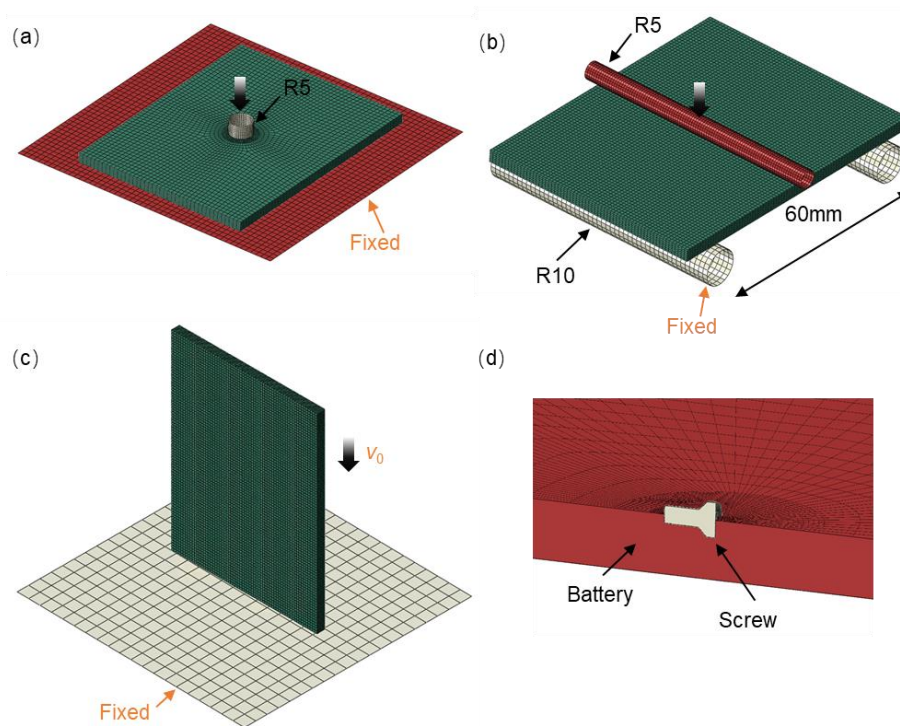


Figure 45 Geometries and boundary conditions of the FE mechanical model. (a) Local compression loading; (b) Three-point bending; (c) Free drop loading; (d) Modeling of defected area.

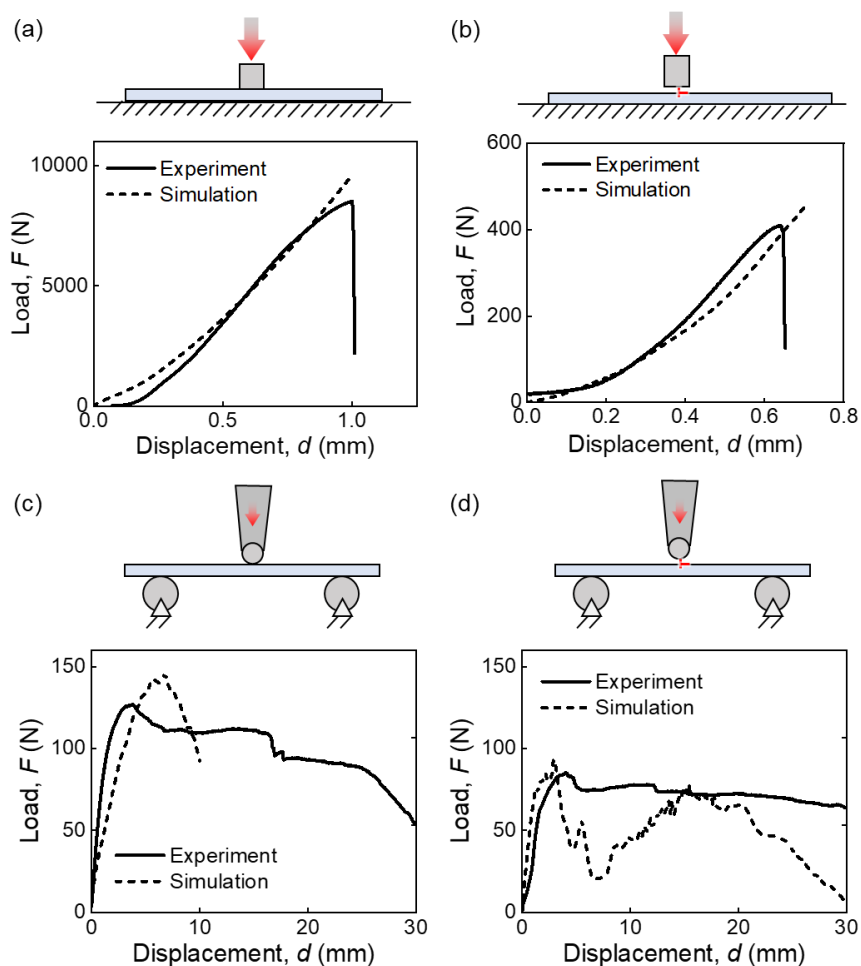


Figure 46 Validation of the finite element model. (a) normal battery indentation; (b) defected battery indentation. (c) normal battery 3-point bending. (d) defected battery 3-point bending.

## 5.2 Results

### 5.2.1 Characterization of defective batteries

Due to the anode-separator-cathode layered structure of the battery, as the loading force increased during screw indentation, short circuits and thermal runaway across the respective layers occurred in sequence, which was observed in real-time by Finegan et al<sup>42</sup>. using high-speed radiography during nail penetration. Once the cathode and anode contacted directly, ISC was then triggered. Subsequently, due to the partial voltage

distribution of ISC resistance (an equivalent resistance), the measured open-circuit voltage dropped immediately to 2.51V in this case. The short circuit current flowing through the short circuit area produced Joule heat and led to the measured surface temperature at point 1 increasing to about 130°C. Interestingly, the voltage recovered to almost the original value with a very trivial decrease, i.e.,  $U_d = U_0 - U_1 = 0.046$  V (initial voltage  $U_0 = 3.883$ V, recovered  $U_1 = 3.837$ V) after 0.8s, and at that time the temperature also started to decrease. The corresponding reason is that the melting of the collector (local area near the ISC point) cut off the short circuit such that the voltage became normal again<sup>19</sup>. However, due to the previous minor ISC, a trivial part of energy was consumed such that the recovered voltage was ~3% less than the original one. After a few seconds, the battery voltage profile went back to normal. Due to the relatively small electrochemical energy release during the short, the critical failure heat produced by short-circuit current only affected a local region within the battery, as demonstrated by the fact that temperature at point 1 in Fig. 47a increased by ~93°C while point 2 only increased by ~5°C. The pictures of a disassembled battery (Fig. 47b) show that most parts of the battery components looked intact except a local area around the indent where a burnt mark was present for the first three electrode layers from the cell's surface. The area of the burnt mark and indentation hole decreased as the layer number increased. The area of the hole in the first layer of the separator was relatively large, which indicated that the collapse of the separator occurred locally.

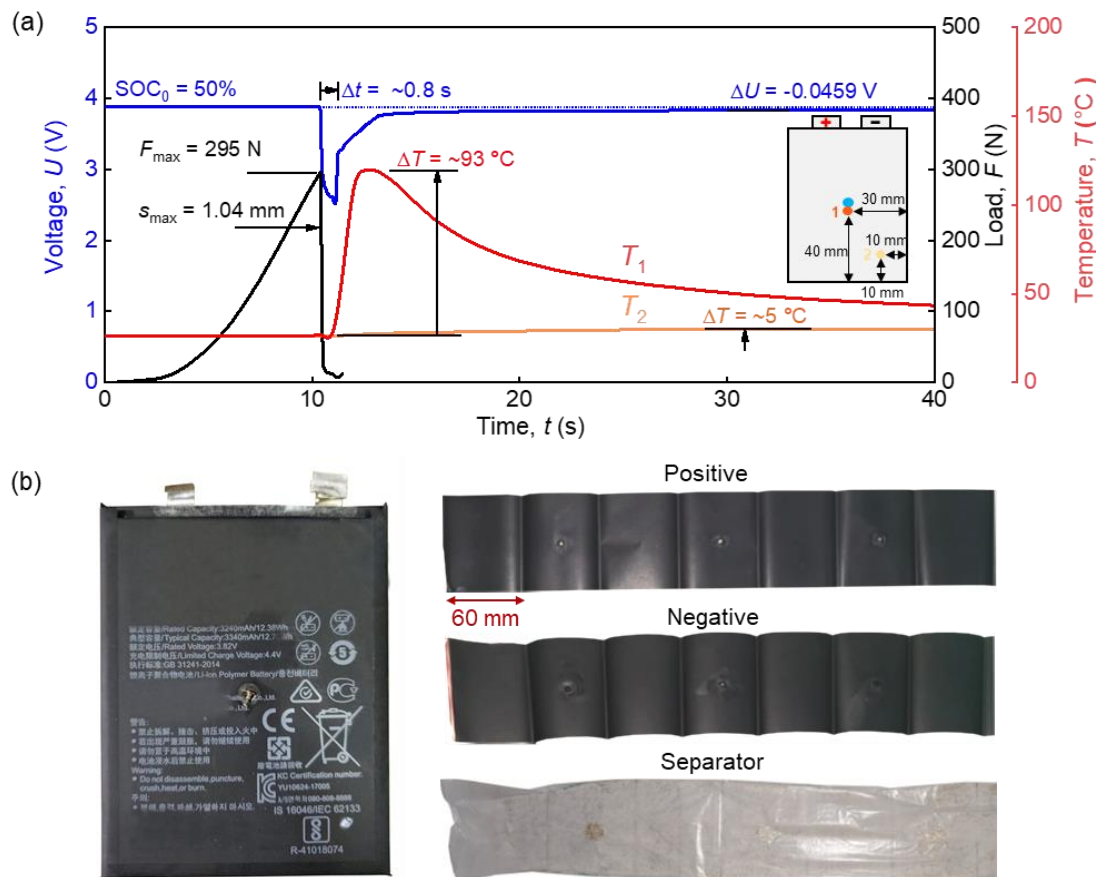


Figure 47 Cell behaviors during mechanical indentation. (a) Force, voltage, and temperature responses of the battery during the loading; (b) Schematic diagram of the battery's physical appearance.

To demonstrate the fundamental differences between defected and normal batteries in terms of electrochemistry, cycling tests, and Electrochemical Impedance Spectroscopy (EIS) tests were used to characterize the defective batteries. A comparison of 1C constant current (CC)-constant voltage (CV) cycling curves between a normal battery and defective battery shows that the defective battery almost works as normal (Fig. 48a). The major differences are the capacity in the CV stage within  $\Delta t_2$ . The capacity loss,  $C_s$ , of the defective battery was about 130 mAh according to the capacity curves (Fig. 49a). In the meantime, the extension of  $\Delta t_2$  is mainly caused by a relatively small leakage current  $I_s$

appears after the recovery, which can be estimated as 44 mA based on the cycling curve. This leakage current slowed down the charging process.  $I_s$  decreases as the cycling number increases and gradually approaches a stable value ( $\Delta t_2$  which is positively correlated with the leakage current, decreases slightly in Fig. 49b), i.e., the value is estimated as 5 mA after about 7 cycles. The soft-short can also prolong the CC charging time  $\Delta t_1$  (with a leakage current of 44mA). However, in the meantime, the capacity loss will shorten the charging time (130mAh). Overall,  $\Delta t_1$  is shorter than the original status.

The capacity loss could be produced by increased internal resistance, reduced total active materials or both. However, the EIS test proved that the reason can only be the reduction of total active materials because there was little change in the ohm internal resistance  $R_0$  and the polarization resistance  $R_{ct}$  of defective batteries (Fig. 48b). The open-circuit voltage (OCV) curve of a defective battery without external working load proved that the current leakage is caused by a soft short-circuit (Fig. 48c). Thus, we propose an equivalent circuit for defective batteries as shown in Fig. 48c. Once the cell is short-circuited, a short-circuit resistance connects to the battery equivalent circuit in parallel. Since this resistance (about  $10\sim 10^2\Omega$ ) is at least 3~4 orders of magnitude greater than the battery internal resistance ( $\sim 10^{-2}\Omega$ ), it is hard to measure any change in the total resistance of the circuit. Thus, capacity loss,  $C_s$ , and leakage current,  $I_s$ , are the only two major parameters that can be detected to differentiate defected and normal cells.

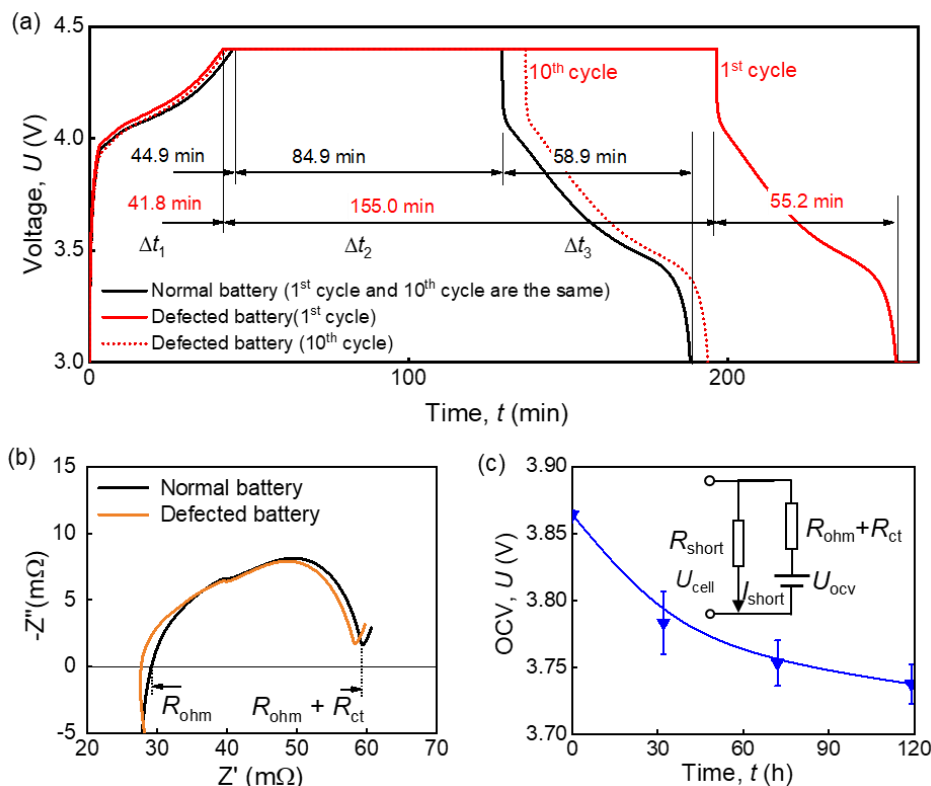


Figure 48 Differences of electrochemical characteristics between defective batteries and normal batteries. (a) Comparison of 1C CC-CV cycling curve, charging cutoff voltage is 4.4V, discharging cutoff voltage is 3.7V, cutoff rate of CV charging is set as 1/50 C; (b) Comparison of the impedance spectroscopy curve, the ohmic internal resistance and polarization resistance changes little; (c) The self-discharging phenomenon indicates a micro ISC.

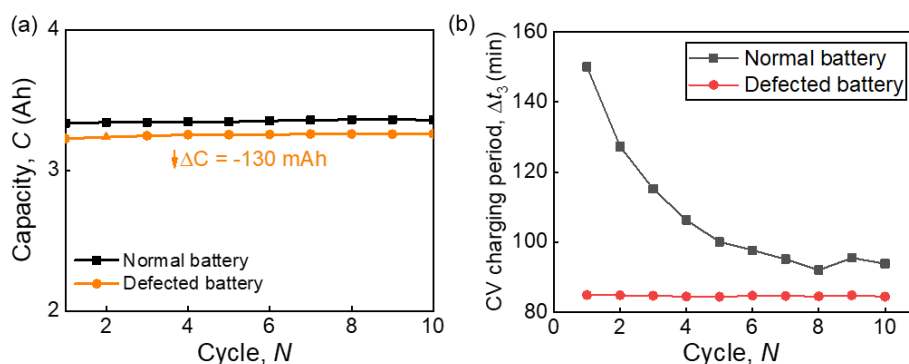


Figure 49 Changes in electrochemical characteristics of the defective battery. (a) comparison of 1C CC-CV cycling capacity curves between the defective battery and the normal battery; (b) Comparison of CV stage period-cycle curve.

Currently, it is experimentally impossible to *in-situ* or *ex-situ* observe the electro-

chemo-thermal behaviors within battery during the defect introduction process and the status. A multi-physics model is thus established to provide more detailed information. This model uses the numerical method to calculate the thermal field during the ISC process and further estimate the damaged area of each material. Based on this model, the damaged area and spatial distributions of the introduced defects for material layer is estimated (Fig. 50a), including SEI decomposition ( $S_{sei} = 42 \text{ mm}^2$ ), separator collapse ( $S_m = 81 \text{ mm}^2$ ), electrolyte decomposition ( $S_e = 22.5 \text{ mm}^2$ ), cathode-electrolyte reaction ( $S_{ce} = 21 \text{ mm}^2$ ) and anode-electrolyte reaction ( $S_{ae} = 9 \text{ mm}^2$ ). These results indicate that the separator melting area is larger than the decomposition reaction areas. These results indicate that the separator melting area is larger than the decomposition reaction areas. In the meantime, the collapse of the separator causes anode-cathode contact with active materials available, generating a leakage current after the voltage recovery, and  $i_{short} = g(S_m - \max(S_{ae}, S_{ce}, S_e)) = g(S_m - S_e)$ . The decompositions of anode, cathode, and electrolyte lead to capacity loss, and  $C_{loss} = f(\max(S_{ae}, S_{ce}, S_e)) = f(S_e)$ . Thus, the short circuit evolution process during the defect introduction can be divided into three stages (Fig. 50b).

- Stage 1, the battery works normally;
- Stage 2, internal short circuit is triggered by the penetration of the screw. The

ISC current flows through the cathode collector, screw and anode collector with a huge amount of heat released in the local area; and

- Stage 3, collector melts, electrode materials decompose, and separator fails due to generated high temperature. The current path across the collectors is cut-off while the current path produced by the contact between active materials is rebuilt.

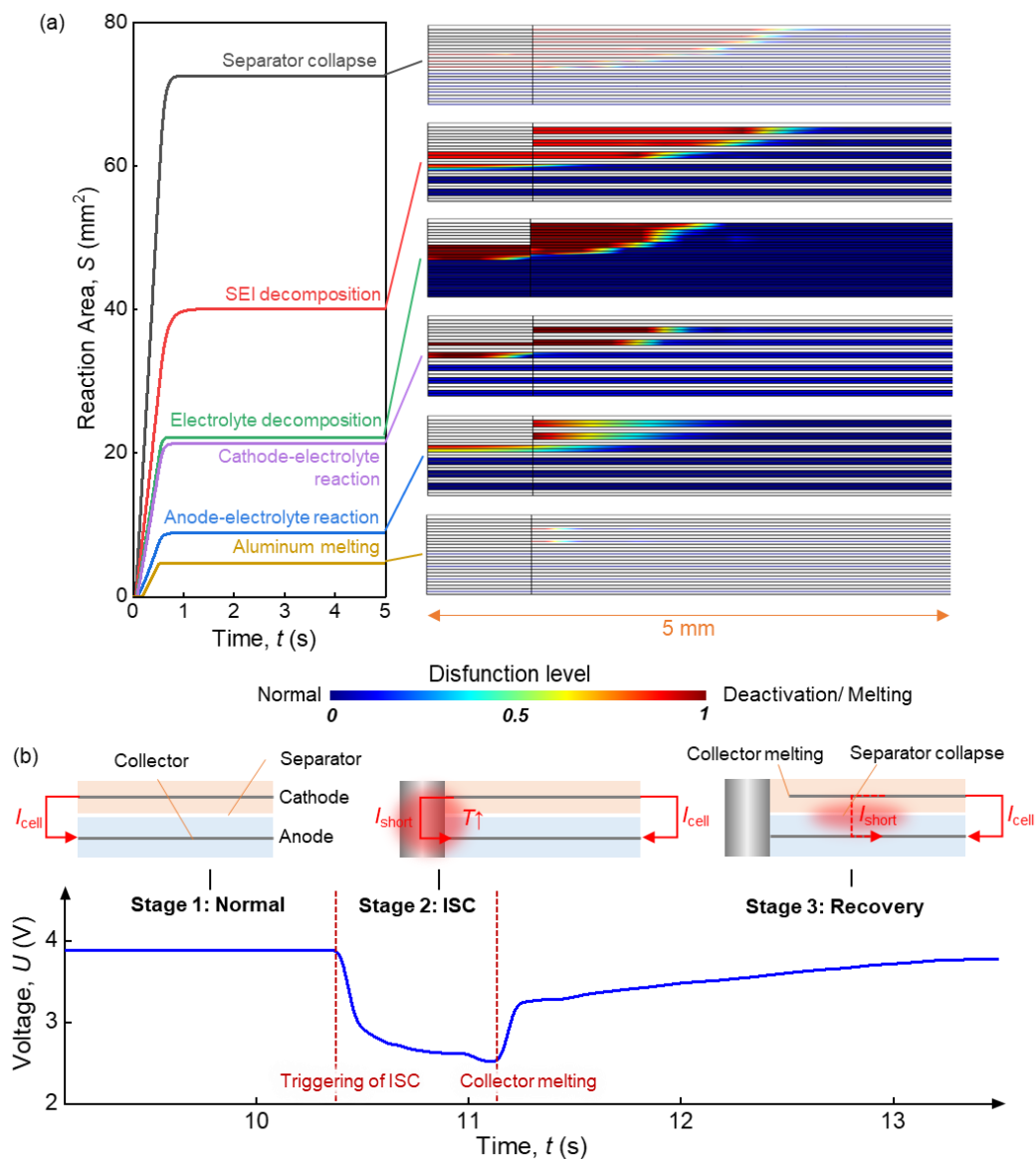


Figure 50 The defect producing process and the internal change of the battery. (a) The damaged area and its distribution of each reaction within the defective battery. The first 10 layers are shown here. Note that the thickness of the collector and separator are small such that the displayed colors look light. (b) Schematic diagram of short-circuit evolution.

### 5.2.2 Effect of defect at different sizes and positions.

It is interesting to note that defect sizes and penetration positions are two important factors that affect capacity loss and leakage current (Figs. 51a and b). Essentially, the defect size and the defect positions determine ISC current  $I_{\text{short}}$ , discharging period  $t_d$ , the discharging capacity  $C_d$  or total released heat  $Q_d$ , and further determine the reaction area  $S_e$  and melting area  $S_m$  (Table. 17), where  $R_{\text{short}} = R_0(U_0 - U)/U$ ,  $I_{\text{short}} = U_0 / (R_0 + R_{\text{short}})$ ,  $C_d = \int I_{\text{short}} dt$ ,  $Q_d = \int I_{\text{short}}^2 R_{\text{short}} dt$ . For the defect size, larger sizes lead to larger capacity loss and current leakage. Larger defect area corresponds to a larger ISC area and a slower voltage recovery speed (Fig.52a). Correspondingly, the separator melting area and battery constituent material damaged areas will be larger (Table. 14). However, the leakage current of  $L = 1$  mm case is slightly larger than the  $L = 1.5$ mm case. This is because the ISC resistance of  $L = 1$ mm case is too large for the joule heat produced by ISC resistance to melt the collector and cut off the short circuit (green line in Fig. 52a and Table. 14). Thus, the separator melting area tends to be larger. In terms of the defect position on the surface of the cell, the center-positioned defects produce smaller capacity loss and leakage. When the ISC point was closer to the edge of the battery, the heat was dissipated more quickly thus voltage recovery would have been slower due to the delayed short circuit cut off (Table 14, Fig. 52b). In this case, the separator melting area became larger, and the capacity loss and leakage current were correspondingly larger (Table. 14).

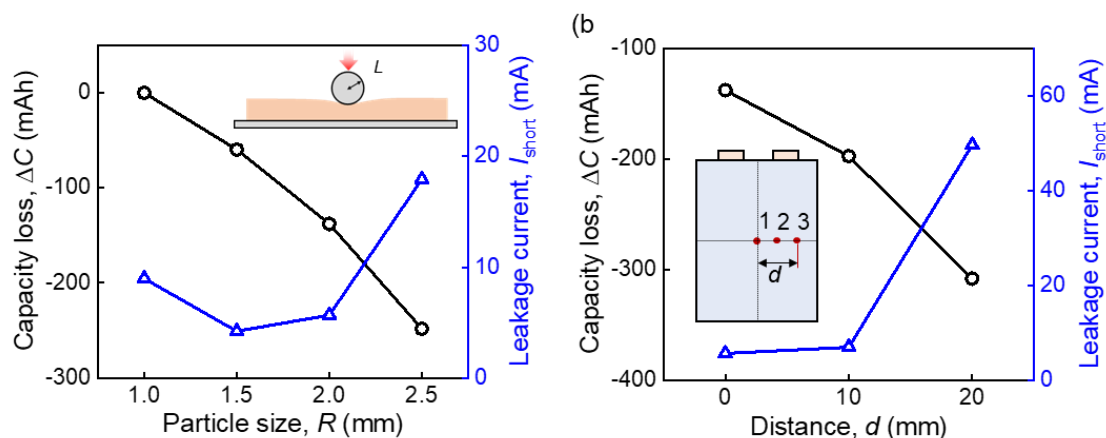


Figure 51 Effect of different defect areas and positions. (a) Capacity loss and leakage at different indenter size (center position); (b) Capacity loss and leakage at different positions (2mm defect).

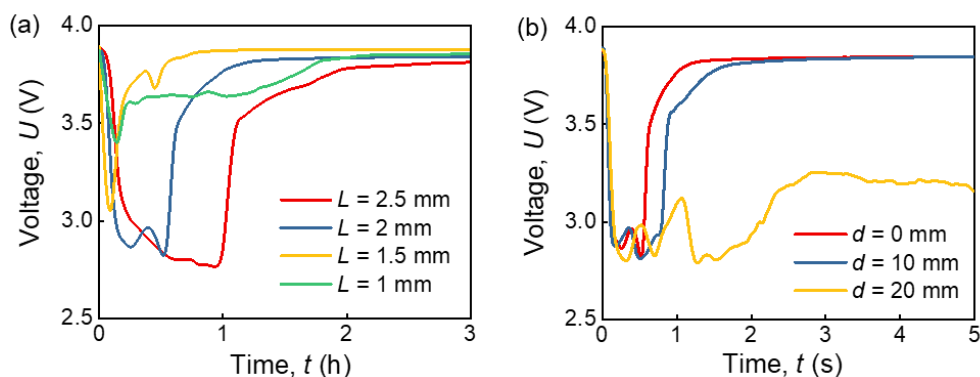


Figure 52 Effect of indenter sizes and indentation positions (1C CC cycling, sphere steel particle). (a) voltage response at different indenter size (from 1.0 mm to 2.5 mm diameter, center); (b) voltage response at different positions (0, 10, 20 mm from center, 2 mm).

Table 14 Estimation of characteristic parameters of the defects at different conditions

|          | $U$ (V)  | $t_d$ (s) | $R_{short}$<br>( $\Omega$ ) | $I_{short}$<br>(A) | $C_d$<br>(mAh) | $Q_d$ (J) | $S_e$<br>( $\text{mm}^2$ ) | $S_m$<br>( $\text{mm}^2$ ) |
|----------|----------|-----------|-----------------------------|--------------------|----------------|-----------|----------------------------|----------------------------|
| $L$ (mm) | $d=0$ mm |           |                             |                    |                |           |                            |                            |
| 1        | 3.33     | 1.05      | 0.36                        | 9.17               | 2.67           | 32.05     | 58.8                       | 108                        |
| 1.5      | 2.95     | 0.15      | 0.19                        | 15.50              | 0.65           | 6.86      | 7.56                       | 14.46                      |
| 2        | 2.85     | 0.55      | 0.17                        | 17.17              | 2.62           | 26.91     | 55.8                       | 89.4                       |
| 2.5      | 2.76     | 1.05      | 0.15                        | 18.67              | 5.44           | 54.10     | 125.4                      | 196.8                      |
| $d$ (mm) | $L=2$ mm |           |                             |                    |                |           |                            |                            |
| 0        | 2.87     | 0.55      | 0.17                        | 16.83              | 2.57           | 26.57     | 55.2                       | 88.8                       |
| 10       | 2.85     | 0.8       | 0.17                        | 17.17              | 3.81           | 39.14     | 87                         | 138.6                      |

|    |     |     |      |       |      |     |     |       |
|----|-----|-----|------|-------|------|-----|-----|-------|
| 20 | 2.8 | 2.5 | 0.16 | 18.00 | 12.5 | 126 | 318 | 492.6 |
|----|-----|-----|------|-------|------|-----|-----|-------|

### 5.3 Discussion

#### 5.3.1 Electrochemical-thermal safety evaluation of defective battery

The thermal stability of the battery deteriorates with cycles due to the current leakage. During a long-term working condition, at least one full charging-discharging cycle, the average temperature of the cell converged into a stable value, which is a steady-state value. Thus, it can be estimated theoretically based on the defective battery equivalent circuit and thermal dynamic equation as

$$\rho V C_p \frac{dT}{dt} = \dot{Q}_{\text{joule}} + \dot{Q}_{\text{conv}} + \dot{Q}_{\text{rad}}, \quad (29)$$

where  $C_p$  is the specific thermal capacity of the battery,  $\rho$  is the density of the battery,  $V$  is the volume of the battery,  $T$  is the battery temperature,  $\dot{Q}_{\text{joule}}$  is the joule heat power (as a function of the short circuit resistance, APPENDIX D),  $\dot{Q}_{\text{conv}}$  is the thermal convection power (as a function of the battery temperature  $T$  and the ambient temperature  $T_{\text{amb}}$ , APPENDIX D), and  $\dot{Q}_{\text{rad}}$  is the thermal radiation power (as a function of  $T$  and  $T_{\text{amb}}$ , APPENDIX D). The calculation methods of these three heat terms can be referred to APPENDIX D (calculation of steady-state temperature part). For steady-state condition  $dT/dt = 0$ ,

$$(T^4 - T_{\text{amb}}^4) \sigma \varepsilon S_{\text{cell}} + (T - T_{\text{amb}}) h_c S_{\text{cell}} - \frac{U + R_0 R_{\text{short}} I_d^2}{R_0 + R_{\text{short}}} = 0. \quad (30)$$

Solving the equations, we may obtain  $T = T_s$ . Thus, the increased joule heat  $\dot{Q}_j$  caused by leakage current may increase the working temperature of the battery and affect

whether the battery works safely. The thermal stability of a defective battery with a short circuit resistance  $R_{\text{short}}$  and environment temperature  $T_{\text{amb}}$  can be evaluated by  $T_s$ . In fact, the normal working temperature is between  $-20^\circ\text{C}$  and  $60^\circ\text{C}$ , decomposition reaction happens over  $90^\circ\text{C}$ , and separator collapse over  $130^\circ\text{C}$  (thermal runaway onset temperature<sup>124</sup>). Herein, we define the four temperature intervals as normal ( $-20^\circ\text{C}$ ,  $60^\circ\text{C}$ ), heated ( $60^\circ\text{C}$ ,  $90^\circ\text{C}$ ), chemical reaction ( $90^\circ\text{C}$ ,  $130^\circ\text{C}$ ), and thermal runaway ( $130^\circ\text{C}$ ,  $\infty$ ). The safety risk levels at various  $R_{\text{short}}$  ( $10^0\Omega \sim 10^3\Omega$ ) and  $T_{\text{amb}}$  are presented in Fig. 53. For room temperature ( $25^\circ\text{C}$ ), the  $T_s$  is more sensitive to  $R_{\text{short}}$ . The boundary of the heated area is very close to the thermal runaway area and the critical resistances distribute in  $1 \sim 10\Omega$ . If the ambient temperature is abnormal ( $>60^\circ\text{C}$ ),  $T_s$  is more sensitive to  $T_{\text{amb}}$  rather than  $R_{\text{short}}$ .

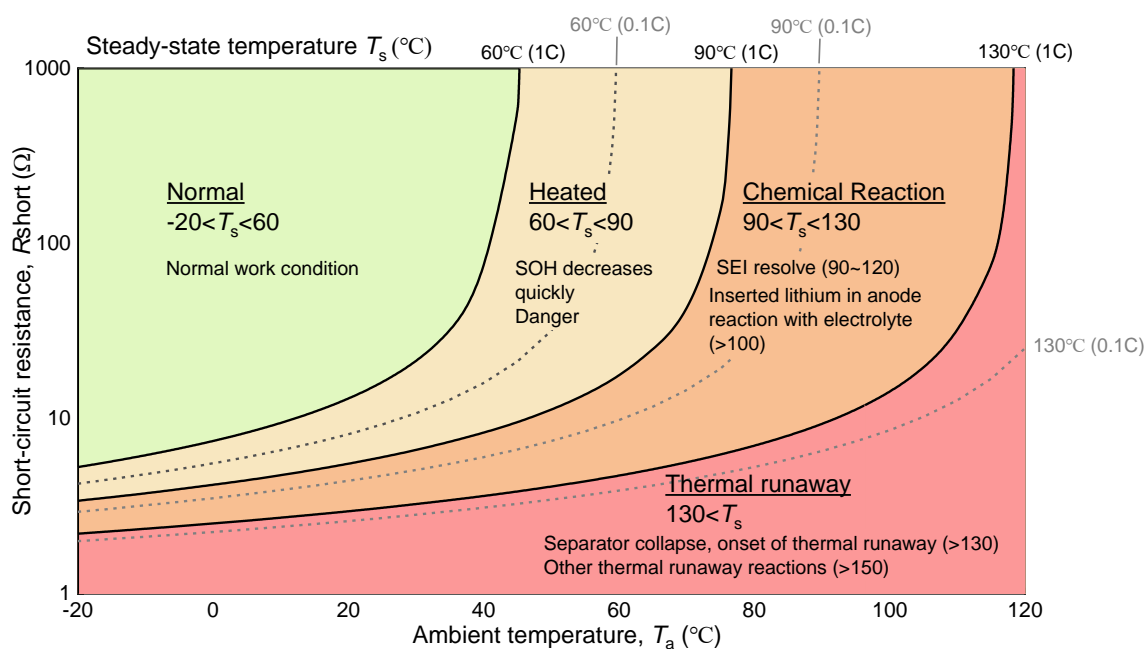


Figure 53 Cycling steady-state temperature at different short-circuit resistance and ambient temperature. Assessment of safety level based on average temperature.

### 5.3.2 Mechanical safety evaluation of defective battery

In addition to thermal issues, another hidden danger should be the mechanical integrity of the defected cells. Here, three representative mechanical abusive loading scenarios, i.e., compression, bending, and free-fall, were targeted to characterize and evaluate the mechanical safety of defective batteries. We observe that the load-bearing capacity before major ISC for the defective battery decreased significantly compared to its original counterpart. Particularly, the load-bearing capacity drops significantly from 9 kN to 0.4 kN in the out-of-plane compression scenario. Note that such a decrease cannot be produced by the heating because the short circuit occurred after the peak load. The temperature was nearly equal to the environment temperature before the decrease point. The short circuit of the battery is mainly caused by the failure of the separator and the contact between the anode and cathode. Thus, an important criterion used here is the strain of the battery in the out-of-plane direction  $\varepsilon_p$ . The strain distribution provided by the FE model is used to evaluate the mechanical safety levels of these three loadings.

During out-of-plane compression loading, the load increases at first and drops suddenly after a peak value (Fig. 54a). The peak point is the mechanical failure point (load drop), which also introduces the ISC (voltage drop). Experimental results indicated that the peak loading decreases from 9 kN to about 0.4 kN (Fig. 54a). The strain distributions estimated by the FE model shows that the maximum  $\varepsilon_p$  decrease from -0.4 to -0.7 (“-” sign means compression). Thus, the failure strain is estimated as -0.4. For the bending (Fig.

54b), the peak force of the defective battery is also lower than the normal battery. These peak points are caused by the bulking of the batteries during bending rather than mechanical failure. Thus, the ISC is not triggered. The results provided by the FE model show that  $\varepsilon_p$  in the defective battery case increases by two orders of magnitude, but it is still lower than the short circuit threshold. Similarly, both normal battery and defective batteries have no temperature increase and voltage drop for free drop loading (Fig. 54c). Because  $\varepsilon_p$  is very small under such loading condition. The small temperature fluctuation in the free drop test for the defective battery is considered as a noise signal due to the shock generated by the impact of the thermocouple sensor.

Overall, the defect deteriorates the mechanical integrity and increases the safety risk of the batteries.

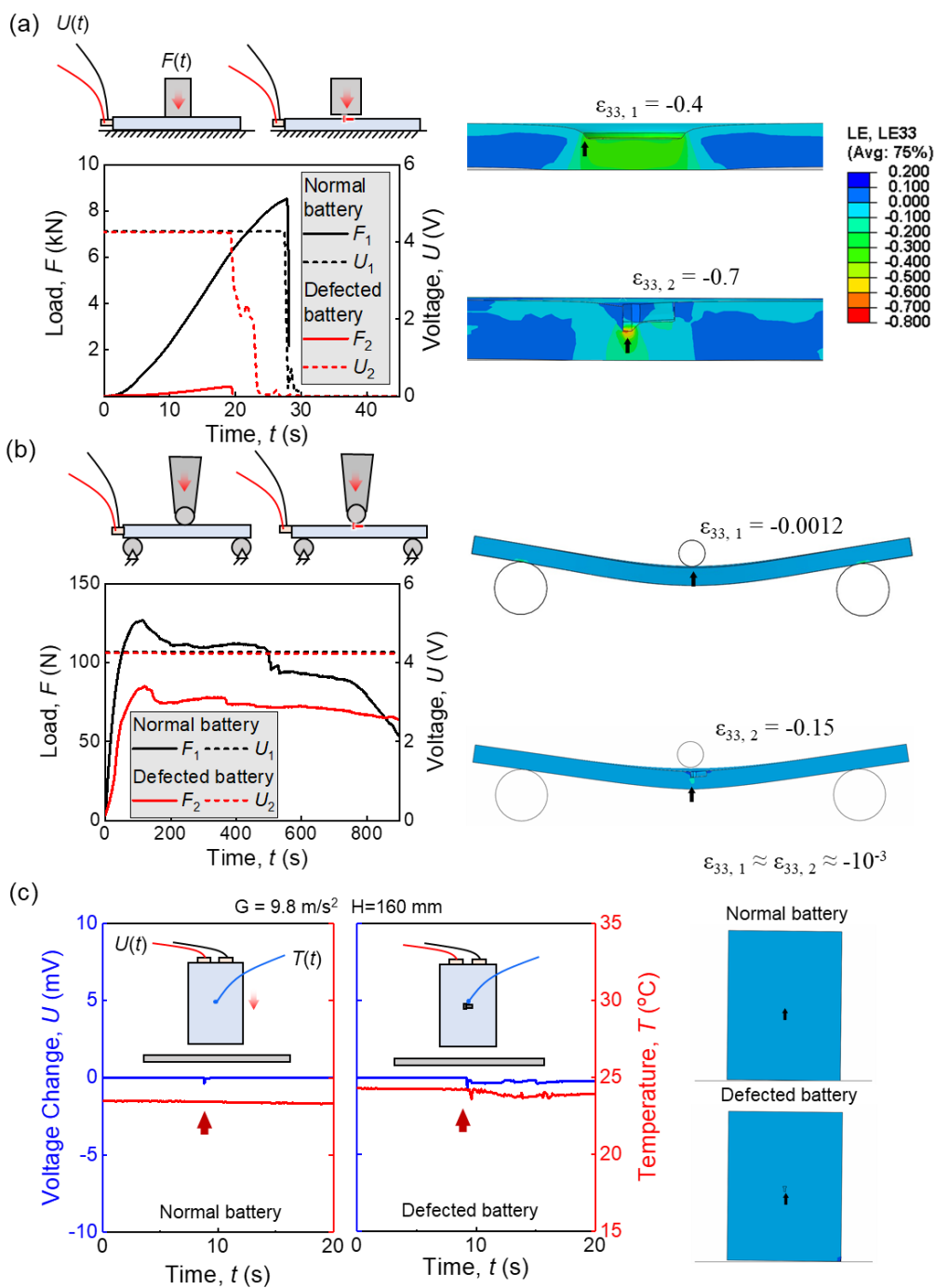


Figure 54 Mechanical safety of the defective battery. (a) Compression loading at 2 mm/min (screw, center), the critical failure force of defective battery has a significant decrease due to stress concentration; (b) 2mm/min 60mm span 3-point bending, no failure but a peak decrease for the defective battery; (c) 160 mm free drop, no failure, voltage, and temperature change.

### 5.3.3 Key features for early detection of defective batteries

According to the experimental results, several possible, detectable characteristics of the defective batteries are summarized in Table. 15. For transient variables during the defect introducing process, voltage decrease, temperature increase, and SOC loss after the process are three major parameters that are possible to be monitored or detected. ISC current and resistance cannot be used for detection because the short circuit occurs inside the battery and has little influence over the external circuit. These three characteristics are:

- ① voltage drops below its discharging cut-off voltage and recovery for a short time (0.1s~1s);
- ② SOC falls significantly within a short time, and
- ③ temperature at any point is above the normal value.

Due to the data collector frequency limit, the transient characteristics are difficult to be captured by BMS, although theoretically possible. A more feasible method is to monitor the steady-state variables, which can be measured after at least one cycle. Compared to the transient parameters, more steady-state variables could be measured, *e.g.*, cycling voltage-time curve, cycling period (for each stage), SOH, working temperature, and current leakage.

Those characteristics are:

- ① SOC decreases abnormally in standby conditions due to current leakage;
- ② Voltage-SOC curve changes due to capacity loss (the SOC decreases at the same voltage);

- ③ SOH decreases abnormally when compared to the last cycle;
- ④ Working temperature increase suddenly caused by leakage current;
- ⑤ CC charging or discharging period decreases, the CCCV charging period increases,  
and
- ⑥ Capacity calculation by time integral current is significantly larger or smaller than  
normal value caused by leakage current.

Surely, the ISC also cannot be detected by purely measuring internal resistance because the short-circuit resistance is much bigger than the original internal resistance and has little influence over internal resistance. The battery is suspected of having defects/minor damage when any of these conditions are satisfied. Detection accuracy depends on resolutions of the related sensors and the amplitudes of these changes. The amplitudes are determined by the defected area and position within the battery as we discussed above. Conservatively speaking, all the defective batteries that can be identified should be reported to users or replaced directly due to the significant increased thermal risk and the deteriorated mechanical integrity of defective batteries. The visibility of the defect is determined by the accuracy and sensitivity of the related sensors of battery BMS. Thus, the thresholds are mainly determined by the sensitivity of the related sensors beyond the scope of this research.

Table 15 Key features of defective batteries produced by the local foreign body intrusion.

|  |                          |  |
|--|--------------------------|--|
|  | <b>Transient</b> (1~3 s) | <b>Steady-state</b> (at least one cycle) |
|--|--------------------------|--|

|  | <ul style="list-style-type: none"> <li>• Voltage drop</li> <li>• Temperature increase</li> <li>• SOC loss</li> </ul> |  | <ul style="list-style-type: none"> <li>• Leakage current</li> <li>• Capacity Loss</li> </ul> |   |
|--|--|--|--|---|
| Variables  | Trend  | Reason/<br>Main features   | Trend  | Reason/<br>Main features  |
| Current  | ×  | Load resistance and short-circuit resistance are connected in parallel                     | ↗  | $10^0 \sim 10^2$ mA leakage current   |
| Voltage  | ↘ ↗  | Drops 0.5 ~1 V and lasts 0.1~1 s;<br>Voltage recover to ~40mV lower than the original one; | Change   | Cycling voltage-time curve changes due to the capacity loss                         |
| SOC  | ↘  | Decreases ~3 %   | —  |   |
| SOH  | —  |  | ↘  | ~ 4 % capacity loss<br>1C charging-discharging Capacity<br>↘ ~ $10^1 \sim 10^2$ mAh |
| Resistance   | ×  | Short circuit resistance (0.1~1Ω) but the period is too short                              | ×  | Short circuit resistance ( $10^0 \sim 10^3$ Ω) >> Internal resistance (~30 mΩ)      |
| Temperature  | ↗  | Local temperature increase ~ $10^2$ K  | ↗  | The steady-state increase depends on working condition                              |
| Cycle period   | —  |  | ↗ or ↘   | CC Charging ↘<br>CCV Charge ↗<br>CC Discharging ↘                                   |
| ↗ increase ↘ decrease × no change or almost no change (unable to identify) |  |  |  |   |

#### 5.4 Conclusion

Safety risk evaluation of defective battery cell remains an unsolved but pressing

problem. In this chapter, we proved that the introduction of minor defects could be undetected due to its quick voltage recovery and very local temperature increase during the intrusion/ penetration process. We discovered that capacity loss caused by deactivating components and current leakage caused by internal minor short-circuit are two major indicators for defective batteries. We demonstrated that the defect deteriorates the safety level of the cell due to the decreased thermal stability and decreased mechanical integrity. As such, the identification of such defective batteries becomes important. To this end, we also proposed several methodologies by using either transient or steady-state variables to detect the defective batteries which are applicable in BMS. The power of combined *operando* experiments and numerical modeling methodology provides fundamental safety risk understanding and insights of defective batteries, as well as develops methodologies for future defective batteries identification and risk evaluation.

## CHAPTER 6 THERMAL RUNAWAY PROPAGATION WITHIN A BATTERY PACK

In this chapter, we focus on the safety issue when the TR has been triggered: TR propagation within battery packs. The TR propagation behaviors of small-size packs are experimentally studied. An efficient yet accurate pack TR model is constructed based on theoretical analysis and the multiphysics modeling framework. The established model is validated by a series of mechanically triggering runaway propagation tests. The experimental and simulation results indicate that there are two major thermal spread modes. Their governing factors are also discussed. Therefore, the TR propagation mechanism is fully revealed to some extent.

### 6.1 Methods

#### 6.1.2 Experimental battery samples

The battery used in this study is a widely commercialized NCA 18650 lithium-ion battery, namely, the Panasonic NCR 18650-B, which possesses NCA/graphite as electrodes. The nominal capacity of this battery is 3350 mAh, and its charge/discharge cutoff voltages are 4.2 and 2.5 V, respectively. The cell mainly consists of a jellyroll, an inside winding nail, and a steel shell. The jellyroll consists of anode and cathode materials, separators, current collectors, and electrolytes. In general, the electrolyte is dissolved LiPF<sub>6</sub> salt in carbonate solvents<sup>125</sup>. All brand-new batteries are charged to full SOC by a BK6808AR rechargeable battery performance tester.

### 6.1.2 Thermal runaway propagation experiment design

TR propagation tests were performed in an explosion-proof fume hood fixed in a universal material test machine, namely, the SANS UTM5000 (Fig.55). The plastic outer skin of each battery was peeled away. Specific numbers of single batteries were tied by some slender copper wires and then painted by black high-temperature paint to form the battery pack used in this study. In some cases, the batteries of each pack were connected by nickel sheets in parallel. During the tests, one of the batteries in each pack was penetrated by a 2 mm diameter needle with a 6 mm/min loading rate. Simultaneously, a camera was used to record the experimental phenomena. An infrared thermal imager was used to measure the surface temperature distribution through an infrared transparent sapphire window on the explosion-proof fume hood. A multimeter Agilent 34970A was applied to collect the voltage data of the battery pack. K-type thermocouples were placed at the axial midpoints on the surface of batteries. The temperature contribution of each battery is assumed that satisfies the lumped model<sup>12</sup>. Therefore, the measured temperatures were the average temperatures of the batteries. The batteries were tied with copper wire with some pre-pressure. The battery numbers are defined as Fig. 55. In order to facilitate the establishment of the model, the battery pack in this paper is a kind of idealized battery pack, related fixed structures and other parts in battery modules are ignored. The contact relationship among batteries will be abstracted into several equivalent thermal resistances.



exothermic reaction heater source is calculated by an electrochemical model of a single cell jellyroll domain that is established using Arrhenius equations<sup>18, 88</sup>.

The equation of energy balance can be written as follows:

$$\rho C_{p,jr} dT_i/dt = \dot{Q}_{exo,i} + \sum_k \dot{Q}_{conv\_inner,i,k} + \dot{Q}_{joule,i}, \quad (31)$$

where the terms  $\rho_{jr}$  (kg/mm<sup>2</sup>),  $C_{p,jr}$  (J/K),  $T$  (K) are the average density, the total heat capacity and the average temperature of jellyroll, respectively.

The chemical reaction rates  $\dot{Q}_{exo,i}$  of a single cell jellyroll domain are calculated by using Arrhenius equations as follows<sup>18, 88</sup>:

$$dc_a/dt = -c_a \cdot A_a \cdot \exp(-E_a/k_bT) \cdot \exp(-z/z_0), \quad (32)$$

$$dz/dt = c_a \cdot A_a \cdot \exp(-E_a/k_bT) \cdot \exp(-z/z_0), \quad (33)$$

$$dc_s/dt = -c_s \cdot A_s \cdot \exp(-E_s/k_bT), \quad (34)$$

$$d\alpha_c/dt = \alpha_c \cdot (1 - \alpha_c) \cdot A_c \cdot \exp(-E_c/k_bT), \quad (35)$$

$$dc_e/dt = -A_e \cdot \exp(-E_e/k_bT), \quad (36)$$

$$dSoC/dt = -ISC_{cond} \cdot SoC \cdot A_{ec} \cdot \exp(-E_{ec}/k_bT). \quad (37)$$

Eqns. 32–36 describe the decomposition reaction.  $T$  is the average temperature of the cell.  $c_a$  and  $c_s$  represent the fractions of Li-ion present in the anode and solid electrolyte interphase (SEI), respectively.  $\alpha_c$  is the degree of conversion of the cathode.  $z$  is the SEI thickness according to the tunneling effect<sup>65, 128</sup>.  $c_e$  is the dimensionless concentration of the electrolyte. Eq. 37 estimates the SOC<sup>129</sup>. The term  $ISC_{cond}$  is used to control the triggering of the battery ISC. The ISC triggering condition is set as when the temperature of the jellyroll node reaches the separator melting point<sup>124, 130</sup> (165°C for the

chosen battery). The ISC of the first battery was triggered manually in the model ( $ISC_{\text{cond}} = 1$  for the first battery).

The exothermic reaction heater source  $\dot{Q}_{\text{exo},i}$  is defined as follows <sup>18</sup>:

$$\dot{Q}_{\text{exo},i} = \dot{Q}_a + \dot{Q}_c + \dot{Q}_s + \dot{Q}_e + \dot{Q}_{\text{ec}}, \quad (38)$$

$$\dot{Q}_a = -m_a h_a dc_a / dt, \quad (39)$$

$$\dot{Q}_c = m_c h_c d\alpha_c / dt, \quad (40)$$

$$\dot{Q}_s = -m_s h_s dc_s / dt, \quad (41)$$

$$\dot{Q}_e = -m_e h_e dc_e / dt, \quad (42)$$

$$\dot{Q}_{\text{ec}} = -h_{\text{ec}} dSoC / dt. \quad (43)$$

Eqns. 39–42 describe the heat release rate of decomposition reactions. Eq. 43 illustrates the heat release rate of electrical–thermal conversion during discharging. The enthalpies in Eqns. 39–42 have been given by references, as shown in the nomenclature. The enthalpy in Eq. 43 is given as follows <sup>18</sup>:

$$h_{\text{ec}} = 3600UC\eta, \quad (44)$$

where  $U$  is the nominal discharge voltage, and  $C$  is the nominal battery capacity.  $\eta$  is the efficiency factor that represents how much electrical energy is converted to thermal energy. In this model,  $\eta = 0.47$  was obtained by matching the peak temperature of the experiment. Thus, the exothermic reaction power is determined by the instantaneous SOC and Temperature.

The term  $\dot{Q}_{\text{joule},i}$  represents the joule heat during the discharge produced by the ISC

or ISC-triggered batteries in the same parallel connection module. The Joule heat can be calculation by Joule's law and Ohm's law <sup>17</sup>. For a parallel-connected battery system with several batteries (Fig. 56c). If the battery number is N, the short-circuit current can be written as follows:

$$I_{r0} = \sum_{i=1}^N I_{ri} , \quad (45)$$

$$I_{ri} = U / (N \cdot R_{\text{short}} + R_0) . \quad (46)$$

Furthermore, joule heats are calculated as follows:

$$\dot{Q}_{\text{joule},1} = (V / (N \cdot R_{\text{short}} + R_0))^2 \cdot (N^2 R_{\text{short}} + R_0) \cdot (1 - ISC_{\text{cond}}) , \quad (47)$$

$$\dot{Q}_{\text{joule},i} = (V / (N \cdot R_{\text{short}} + R_0))^2 \cdot R_0 \cdot (1 - ISC_{\text{cond}}) , i = 2, 3 \dots N , \quad (48)$$

where the term  $1 - ISC_{\text{cond}}$  means that if TR occurs and the separator starts melting, this mechanical ISC discharging would be terminated. Note that the additional thermal resistance brought by the wires is ignored.

For other nonparallel connected situations, the ISC-triggered battery has no electrical connection with surrounding batteries. Thus, the joule heat can be calculated by Eq. 50 in  $N=1$ . For the first battery, when  $SoC=0$ , the ISC heater  $\dot{Q}_{\text{joule},1}$  will be set as 0.

$\dot{Q}_{\text{conv\_inner},i,k}$  is the heat transfer between the jellyroll node  $i$  and the shell node  $k$  of battery  $i$ . Thermal resistance  $\theta_p$  is set among the jellyroll and shell nodes.  $\dot{Q}_{\text{conv\_inner},i,k}$  can be written as follows:

$$\dot{Q}_{\text{conv\_inner},i,k} = 2\pi h R_{\text{outer}} (T_i - T_{si,k}) / \theta_p , \quad (49)$$

where  $T_{si}$  is the shell node  $j$  temperature of battery  $i$ ,  $\theta_p$  is the thermal resistance between

the jellyroll and the battery shell. The thermal conductivity of separator is an order of magnitude smaller than other materials within the jellyroll <sup>12</sup>, thus,  $\theta_p$  can be estimated by the following equation:

$$\theta_p = t_{\text{sep}} / (2\pi h R_{\text{outer}} \lambda_{\text{sep}}), \quad (50)$$

where  $R_{\text{outer}}$  is the outer radius of the jellyroll,  $t_{\text{sep}}$  is the thickness of the separator, and  $\lambda_{\text{sep}}$  is the thermal conductivity of the separator.

For shell nodes, the energy equation considers the heat input (consisting of the quantity of heat transfer from jellyroll nodes to the shell nodes of thermal conduction), thermal conduction among the shell nodes and the heat output (consisting of the quantity of heat transfer from a battery to the circumstances of thermal conduction, thermal convection, and thermal radiation). It can be written as:

$$\rho_s C_{p,s} dT_{si,k} / dt = \sum_k (\dot{Q}_{\text{conv\_inner},i,k} + \dot{Q}_{r,i,k} + \dot{Q}_{f,i,k}) + \sum_j \dot{Q}_{\text{conv\_outer},i,j}, \quad (51)$$

where the terms  $\rho_{\text{shell}}$ ,  $C_s$ ,  $T_s$  are the average density, the total heat capacity, and the average temperature of battery shell, respectively. Based on the geometrical parameters of the batteries,  $C_{p,jr}$  and the average density  $\rho_{jr}$  can be estimated by the following equations:

$$C_{p,s} = c_{p,\text{shell}} \rho_{\text{shell}} V_{\text{shell}}, \quad (52)$$

$$V_{\text{shell}} = S_{\text{shell}} \times t_{\text{cell}}, \quad (53)$$

$$S_{\text{shell}} = 2\pi(R_{\text{outer}} + R_{\text{inner}})l_{\text{cell}} + 2\pi R_{\text{outer}}^2, \quad (54)$$

$\dot{Q}_{f,i,k}$  is the radiation power of shell point  $k$  of battery  $i$ .  $\dot{Q}_{\text{conv\_outer},i,j}$  is the heat

conduction power between battery  $i$  and battery  $j$ . Taking quadrilateral packing as an example. The related equations <sup>12</sup> are shown as follows:

$$\dot{Q}_{\text{conv\_outer},i,j} = -(T_{si,k} - T_{sj,l})/\theta_c, \quad (55)$$

$$\dot{Q}_f = -1/4h_{\text{conv}}(T_{si,k} - T_{\text{amb}})S_{\text{cell}}, \quad (56)$$

where  $T_{si,k}$ ,  $T_{sj,l}$  are the shell nodes temperatures of batteries  $i$ ,  $j$  respectively;  $k$ ,  $l$  represent specific nodes in battery shells.  $\theta_c$  represents the total equivalent thermal transfer coefficient between the two adjacent batteries (K/W). It is calculated by a FEM model (Fig. 57). In this model, two steel pillars of width  $h$  with a semi-cylindrical face in on end are placed close together. A 100 W input heater is set in one end and a temperature boundary condition  $T = T_{\text{amb}}$  in another end. The thermal resistance can be calculated by the equation shown in the Fig.57.  $h_{\text{conv}}$  is the convection coefficient.

$\dot{Q}_{r,i,k}$  is the thermal radiation power. The thermal radiation can be calculated by the equation <sup>12</sup>, as follows:

$$\dot{Q}_{r0,i,k} = \varepsilon\sigma(T_{si,k}^4 - T_{\text{amb}}^4)S_{\text{cell}}, \quad (57)$$

where  $\varepsilon = 0.3$  <sup>12</sup>, and  $\sigma_b = 5.67 \times 10^{-8} \text{ Wm}^{-2}\text{K}^{-4}$  is the Stefan–Boltzmann constant.  $S_{\text{cell}}$  is the surface area of the battery. According to the geometrical relationship, 1/6 of the thermal radiation heat can be absorbed by a neighboring battery based on the ideal assumption that the surface heat absorptivity of each battery is 1. For example, if  $60^\circ < \alpha \leq 90^\circ$  (Fig.56c), the rate of each node can be written as (consider the two-way effect of the radiation):

$$\dot{Q}_{r,i,k} = \dot{Q}_{r0,i,k} - 2/3 \cdot \dot{Q}_{r,j,l} \quad (58)$$

where  $\dot{Q}_{r0,i,k}$  refers to the origin radiant energy emitted of battery  $i$ , shell node  $k$  and  $\dot{Q}_{r,i,k}$  refer to the total radiant energy released after considering the two-way effect. are the surface temperatures of batteries  $i, j$  respectively;  $k, l$  represent specific nodes in battery shells.

The global ordinary differential and differential-algebraic equation component in software COMSOL Multiphysics are used to solve the model. The parameter setups are list in Table 16. The step time is set as adaptive. The relative tolerance is set by  $10^{-5}$ . The total calculation time is 30 min ~ 60 min (4 cores).

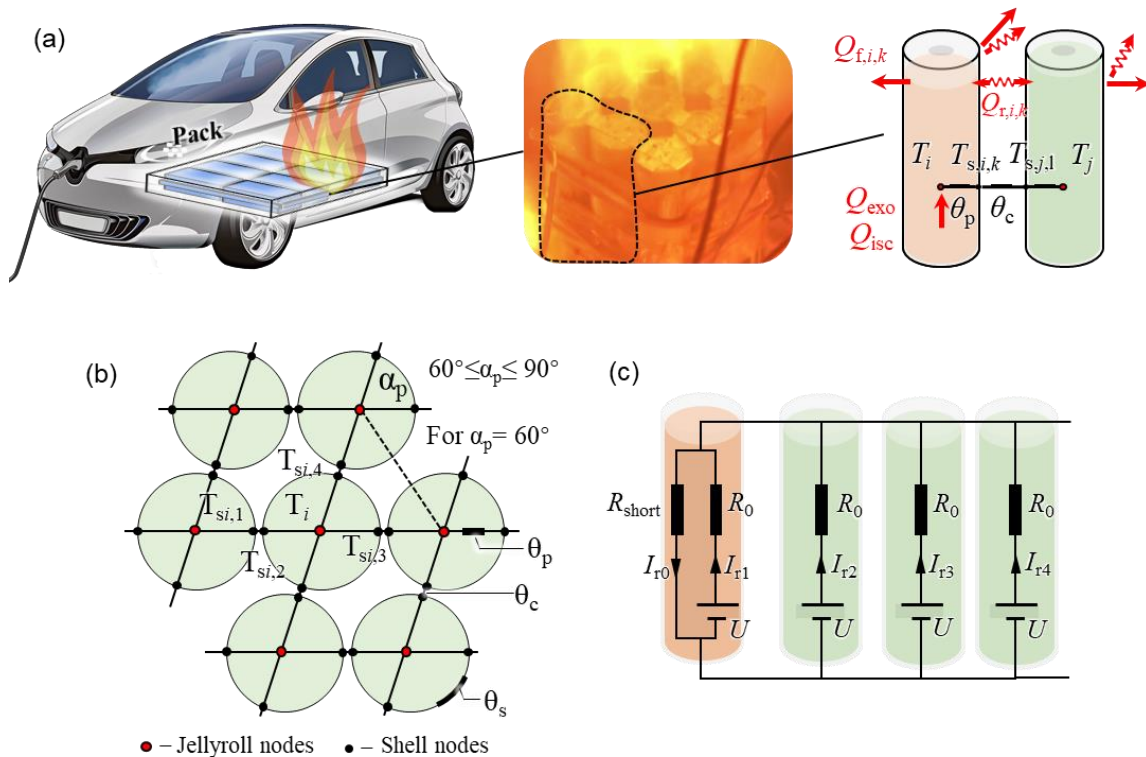


Figure 56 Schematic of the TR propagation model. (a) The thermal equivalent method of a single battery and links among cells; (b) Node division method; (c) Schematic of the electric connections.

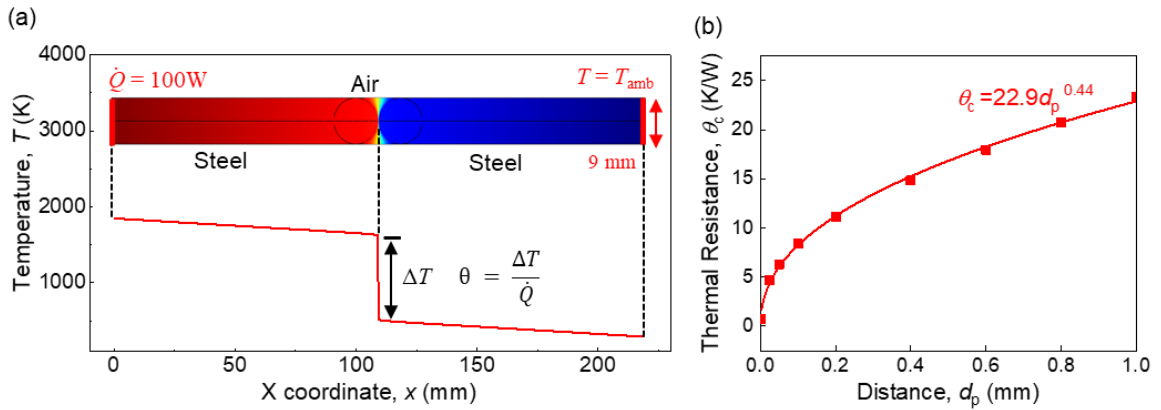


Figure 57 Schematic illustration of the cylindrical surface contact resistance measurement. (a) Numerical experiment setup and calculation method of equivalent resistance; (b) Calculation results, the relationship between spacing and thermal resistance.

Table 16 Parameter values and data sources.

| Parameter | Description                                     | Value                 | Unit             | Source             |
|-----------|---|-----------------------|------------------|--------------------|
| $A_a$     | Frequency factor for anode decomposition        | $2.5 \cdot 10^{13}$   | $\text{s}^{-1}$  | Ref. <sup>69</sup> |
| $A_c$     | Frequency factor for cathode decomposition      | $6.67 \cdot 10^{11}$  | $\text{s}^{-1}$  | Ref. <sup>69</sup> |
| $A_{ec}$  | Frequency factor for electrochemical reactions  | $3.37 \cdot 10^{12}$  | $\text{s}^{-1}$  | Ref. <sup>18</sup> |
| $A_s$     | Frequency factor for SEI decomposition          | $1.67 \cdot 10^{15}$  | $\text{s}^{-1}$  | Ref. <sup>69</sup> |
| $A_e$     | Frequency factor for electrolyte decomposition  | $5.14 \cdot 10^{25}$  | $\text{s}^{-1}$  | Ref. <sup>70</sup> |
| $C$       | Capacity of battery                             | 3.35                  | Ah               | Meas.              |
| $U$       | Nominal voltage of cell                         | 4.2                   | V                | Meas.              |
| $E_a$     | Activation energy for anode decomposition       | $2.24 \cdot 10^{-19}$ | J                | Ref. <sup>69</sup> |
| $E_c$     | Activation energy for cathode decomposition     | $2.03 \cdot 10^{-19}$ | J                | Ref. <sup>69</sup> |
| $E_{ec}$  | Activation energy for short circuit             | $1.58 \cdot 10^{-19}$ | J                | Ref. <sup>18</sup> |
| $E_s$     | Activation energy for SEI decomposition         | $2.24 \cdot 10^{-19}$ | J                | Ref. <sup>69</sup> |
| $E_e$     | Activation energy for electrolyte decomposition | $4.55 \cdot 10^{-19}$ | J                | Ref. <sup>70</sup> |
| $h_a$     | Enthalpy of anode decomposition reaction        | 1714                  | $\text{Jg}^{-1}$ | Ref. <sup>69</sup> |

|                    |  |                       |                   |                     |
|--------------------|--|-----------------------|-------------------|---------------------|
| $h_c$              | Enthalpy of cathode decomposition reaction     | 314                   | $\text{Jg}^{-1}$  | Ref. <sup>69</sup>  |
| $h_{ec}$           | Heat released by short-circuit                 | 10.17                 | $\text{kJ}$       | Calc.               |
| $h_s$              | Enthalpy of SEI decomposition reaction         | 257                   | $\text{Jg}^{-1}$  | Ref. <sup>69</sup>  |
| $h_e$              | Enthalpy of electrolyte decomposition reaction | 155                   | $\text{Jg}^{-1}$  | Ref. <sup>70</sup>  |
| $m_a$              | Mass of anode                                  | $8.1 \cdot 10^{-3}$   | $\text{kg}$       | Ref. <sup>131</sup> |
| $m_c$              | Mass of cathode                                | $18.3 \cdot 10^{-3}$  | $\text{kg}$       | Ref. <sup>131</sup> |
| $c_a$              | Fraction of Li in anode                        | $x_{a0}=0.75$         | 1                 | Ref. <sup>69</sup>  |
| $c_s$              | Fraction of Li in SEI                          | $x_{s0}=0.15$         | 1                 | Ref. <sup>69</sup>  |
| $\alpha_c$         | Initial degree of conversion of cathode        | $\alpha_{c0}=0.04$    | 1                 | Ref. <sup>69</sup>  |
| $z$                | Dimensionless measure of SEI thickness         | $z_0=0.033$           | 1                 | Ref. <sup>69</sup>  |
| $c_e$              | Dimensionless concentration of electrolyte     | $c_{e0}=0.033$        | 1                 | Ref. <sup>70</sup>  |
| $\eta$             | Efficiency factor                              | 0.45                  | 1                 | Fit.                |
| $\rho_{jr}$        | Density of jellyroll                           | 2580                  | $\text{kgm}^{-3}$ | Ref. <sup>69</sup>  |
| $\rho_s$           | Density of shell                               | 7800                  | $\text{kgm}^{-3}$ | Approx.             |
| $c_{p,jr}$         | Specific heat capacity of jellyroll            | 2580                  | $\text{kgm}^{-3}$ | Ref. <sup>69</sup>  |
| $c_{p,s}$          | Specific heat capacity of shell                | 7800                  | $\text{kgm}^{-3}$ | Approx.             |
| $V_{\text{cell}}$  | Volume of cell                                 | $1.663 \cdot 10^{-5}$ | $\text{m}^3$      | Calc.               |
| $R_0$              | Internal resistance of battery                 | 40                    | $\text{m}\Omega$  | Meas.               |
| $R_{\text{short}}$ | Equivalent resistance of short-circuit         | 90                    | $\text{m}\Omega$  | Fit.                |
| $R_{\text{inner}}$ | Inner radius of jellyroll                      | 1.125                 | $\text{mm}$       | Meas.               |
| $R_{\text{outer}}$ | Outer radius of jellyroll                      | 9                     | $\text{mm}$       | Meas.               |

|                   |   |        |                       |         |
|-------------------|---|--------|-----------------------|---------|
| $t_{\text{cell}}$ | Thickness of battery shell  | 0.11   | mm                    | Meas.   |
| $l_{\text{cell}}$ | Length of battery   | 65     | mm                    | Approx. |
| $\theta_c$        | Equivalent thermal resistance between two batteries               | $f(d)$ | K/W                   | Approx. |
| $\theta_p$        | Equivalent thermal resistance between battery shell and jellyroll | 0.0363 | K/W                   | Approx. |
| $h_{\text{conv}}$ | Convection heat dissipation coefficient                           | 10     | W/(K·m <sup>2</sup> ) | Approx. |

## 6.2 Results and discussion

### 6.2.1 Experimental results and calibration of the model

Four experiments are conducted in this research. At first, the single battery case is to calibrate the model parameters of the TR model. The result suggests that the convective coefficient is set as 10 W/(m<sup>2</sup>K) (Fig. 58a).

A two-battery experiment is conducted to show the typical process of thermal propagation (Fig. 58b). When the runaway reaction of the first battery is triggered, its temperature increases dramatically to approximately 850 °C. Then, the temperature decreases due to thermal convection, conduction, and radiation. The temperature of the second battery increases rapidly as soon as the runaway reaction of the first battery is triggered. Such a phenomenon indicates that the runaway of the battery can be triggered when thermal propagation occurs in the neighborhood battery. The time interval  $\Delta T$  between the two TR reactions of the cells is approximately 5 s. Based on the infrared signal, the details of the thermal propagation are presented, which mainly contains five major stages: (1) the internal short circuit of the first battery occurs; (2) the runaway reaction of

the first battery is triggered; (3) the flame produced by the first battery starts to heat the neighborhood batteries; (4) the overheat of the local area causes the short circuit of the second battery, and its temperature increases dramatically; and (5) the runaway reaction of the second battery occurs, and a large number of gas blasts the battery case. The battery shell fracture appears on the side near the neighboring battery due to the poor heat dissipation in the area between two batteries; thus, the accumulated thermal energy softens the battery case on the middle side.

When the size of the battery module is increased to  $3 \times 3$ , as shown in Fig. 58c, the duration of the thermal propagation is rather short, and the flame is also very intense. According to the temperature curves, the thermal propagation process is exhibited. The schematic diagram indicates that runaway reactions of two batteries occur at the same time in some stages. The flame produced by the TR reaction triggered batteries is larger enough to lead to the ISC of batteries on a larger scale rather than the adjacent batteries.

Simulation results indicate that this model can predict the triggering runaway reaction of each battery well within a pack. Because of vibration and displacement caused by the fire and explosion on thermocouples, the middle part of the experimental curves has some jitters. Thus, some simulation curves, such as #2 in Fig.58b, do not fit their experimental counterpart well. However, from the point of the onset of TR, the peak temperature, and the cooling process, the simulation results match the experimental results well (Table 17). For larger-scale battery packs, conducting the TR experiment is much more dangerous and

expensive. Thus, the numerical model has more merits and significances to understand the thermal propagation mode and estimate the propagation speed within large battery packs in which the runaway experiments are very difficult to be conducted.

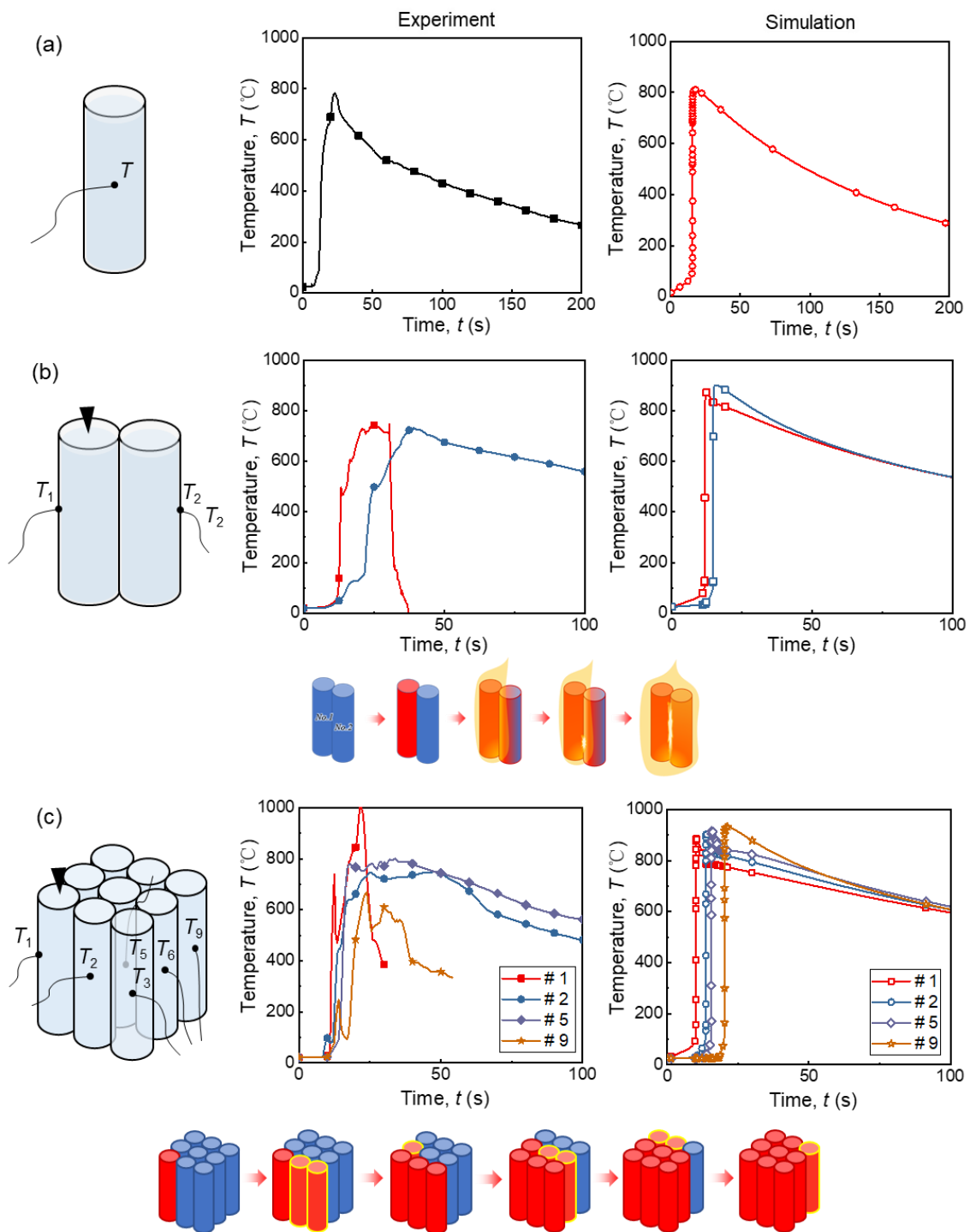


Figure 58 Typical results of experiments and comparison between experiment and simulation. (a) single battery TR; (b) 1×2 pack TR; (c) 3×3 pack TR.

Table 17 Comparison of triggering time and temperature rise between experimental results and simulation results.

| Case           | # | Triggering time (s) |        |                     | Temperature rise (°C) |        |                     |
|----------------|---|---------------------|--------|---------------------|-----------------------|--------|---------------------|
|                |   | Exp.                | Sim.   | Relative error rate | Exp.                  | Sim.   | Relative error rate |
| 2<br>batteries | 1 | 12.75               | 11.821 | -7.29%              | 721.61                | 846.18 | 17.26%              |
|                | 2 | 22                  | 14.761 | -32.90%             | 711.37                | 874.96 | 23.00%              |
|                | 1 | 11                  | 10.054 | -8.60%              | 980.71                | 860.75 | -12.23%             |
| 9<br>batteries | 2 | 12.5                | 13.618 | 8.94%               | 725.58                | 877    | 20.87%              |
|                | 5 | 14.5                | 15.57  | 7.38%               | 781.69                | 890.72 | 13.95%              |
|                | 9 | 18                  | 20.2   | 12.22%              | 725.2                 | 907.38 | 25.12%              |

### 6.2.2 Thermal runaway propagation of large pack under ideal conditions

Based on the established validated model, a 20×20 battery pack is discussed. Battery spacing  $d_p$  is set as 0 mm, the packing angle  $\alpha_p$  is 90°, the state of charge (SOC) is 100%, and the ambient temperature  $T_{amb}$  is 25 °C. The runaway reaction of the battery in the bottom left corner of a 20×20 battery pack is initially triggered. Approximately 86 s after the occurrence of the first runaway reaction, the TRs of all the batteries are triggered. Interestingly, the thermal propagation behaviors as a type of wave with a circular front during this process (Fig. 59a). Runaway reactions are propagated from each thermally triggered battery. The overall propagation front is their envelope. Simulation results also suggest that the speed of the front is approximately a const, defined as the spatial speed  $v_{TR}$ . And  $v_{TR}$  is a function of  $d_p$ ,  $T_{amb}$  and  $\alpha_p$ . Based on these two rules, a concise thermal propagation theory is established. Here, the number of the TR triggered batteries

is defined as  $N_{\text{TR}}$  and the quantitative speed of the thermal propagation  $\dot{N}_{\text{TR}}$  within a pack is defined as the increased number of runaway reactions triggered batteries per unit time from the onset of the first runaway reaction to the last. According to geometric conditions,  $N_{\text{TR}}$  can be written as

$$N_{\text{TR}} = 8\rho_p(v_{\text{TR}}/D_p)^2 t^2, \quad (59)$$

where  $\rho_p$  is the packing density. For  $d_p = 0$  mm,  $\rho_p = 0.785$ . Define  $v_n = v_{\text{TR}}/D_{\text{cell}}$  as the dimensionless propagation spatial speed. Thus, the dimensionless quantitative speed  $\dot{N}_{\text{TR}}$  can be written as

$$\dot{N}_{\text{TR}} = 16\rho_p v_n^2 t, \quad (60)$$

Based on the geometric relationship, the theoretical  $N_{\text{TR}}-t$  curve is calculated, as shown in Fig. 59b. Furthermore, a simple equation can be applied to estimate the total time of the thermal propagation:

$$t_{\text{total}} = \sqrt{(B_p - 1)^2 + (H_p - 1)^2} / v_n, \quad (61)$$

where  $B_p$  and  $H_p$  are the number of batteries in the width and length directions, respectively.  $D_{\text{cell}}$  is the diameter of the battery. The estimation equation can be written in a more universal manner, as follows:

$$T_{\text{total}} = L_n / v_n, \quad (62)$$

where  $L_n$  is the nondimensionalized distance (actual distance normalized by battery diameter) between the first TR-triggered battery and the final TR-triggered battery. For example, when the initial TR is set inside the pack, the  $L_n$  should be the distance between

the initial TR battery to the furthest battery within the pack (Fig. 59c). If the pack has an irregular shape, the TR propagation can be divided into several subprocesses. For example, the T-shaped battery pack's TR propagation can be divided into two subprocesses (Fig. 59d).

For different packing angles, the TR propagation mode does not change. The propagation fronts are round. From a quantitative point of view, the TR propagation of the  $\alpha_p = 60^\circ$  pack is the fastest, the  $\alpha_p = 75^\circ$  pack is the slowest (Fig. 59e). For packs with  $\alpha_p = 60^\circ$ , the TR propagation is slow at first but increases quickly and higher than packs with  $\alpha_p = 90^\circ$ . The reason for the first slow propagation and finally quickly increasing are the same, the thermal contacts are 3/2 time more than the other two types of packs. For battery packs with  $\alpha_p = 75^\circ$ , the thermal contact condition is the same as packs with  $\alpha_p = 90^\circ$ , however, their packing density is low, and the heat dissipation area is larger.

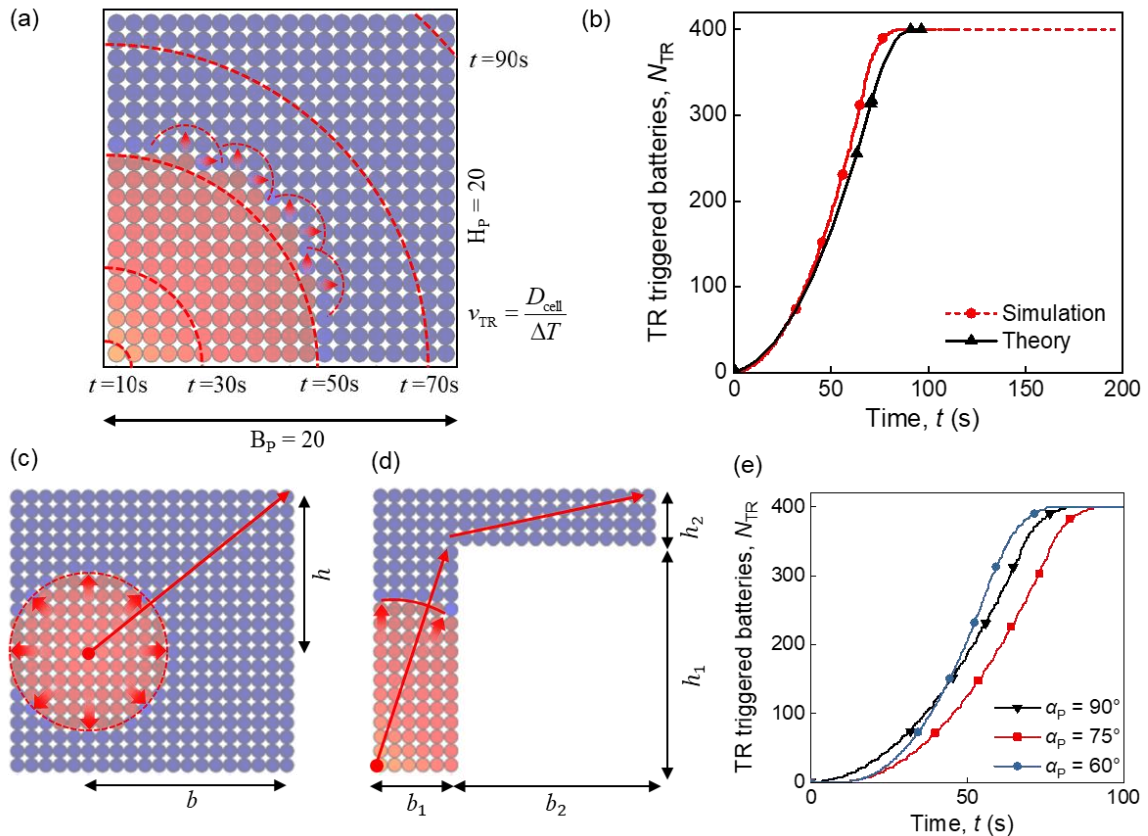


Figure 59 Typical results of the TR of a  $20 \times 20$  ideal thermal contact pack and the estimation method of the total TR propagation time. (a) propagation direction and speed; (b) comparison between theoretical curve calculated by the propagation theory and numerical calculation curve; (c) estimation method for the situation in which the first TR is triggered inside; (d) estimation method for T shape packs; (e) propagation speeds at different packing angles.

### 6.2.3 Propagation modes and speed.

Further research shows that battery spacing  $d_p$  affects the TR propagation speed significantly. Normally, the  $t_{\text{total}}$  of a two-battery pack at  $d_p = 0$  mm is approximately 3 s (Fig. 60a, mode I). For another case at  $d = 0.01$  mm, the  $t_{\text{total}}$  is prolonged to 18.2 s (Fig. 60b, mode II). The shape of the curves also changes. The essential difference between those two phenomena is their different  $\theta_c$  values. Thus, two modes of TR propagation exist, based on the value of  $\theta_c$ . The two modes are also found in experiments (the thermal

images). Mode I: low  $\theta_c$  leads to a local overheating in the battery surface. The surface temperature exceeds the melting point of the separator quickly. The melting of the separator produces a local short circuit. This early-triggered ISC further accelerates TR triggering. Mode II: high  $\theta_c$  prevents conductive heat from concentrating on the battery surface. The surface and jellyroll average temperatures converge over time. When the temperatures reach the  $T_{TR}$  (melting point of the separator), the TR will inevitably be triggered. The total time of TR propagation is significantly longer than that of Mode I. These results can be proven by the surface temperature curve (Fig. 60a). The simulation indicates that the threshold  $\theta_c = 0.89$  K/W. Based on Mode II ( $d$  is set as 0.01 mm,  $\theta_c = 2.94$  W/K), the TR propagation front tends to be quadrate in a  $90^\circ$  pack (Fig. 60b). In a  $60^\circ$  packing scenario, similar results are obtained by the model. The TR propagation front tends to be a hexagon (Fig. 60c).

For Mode II, batteries are mainly heated by the surrounding TR-triggered batteries before their TRs are triggered. In this case, the batteries inside are heated by two batteries at the same time. Their TRs are triggered more quickly along the direction perpendicular to the front compared with that along the front (Fig. 60b–c). However, for Mode I, batteries are heated by surrounding batteries and themselves due to their early-triggered ISC. Thus, the differences among the TR propagation speeds in all directions are not obvious in this case.

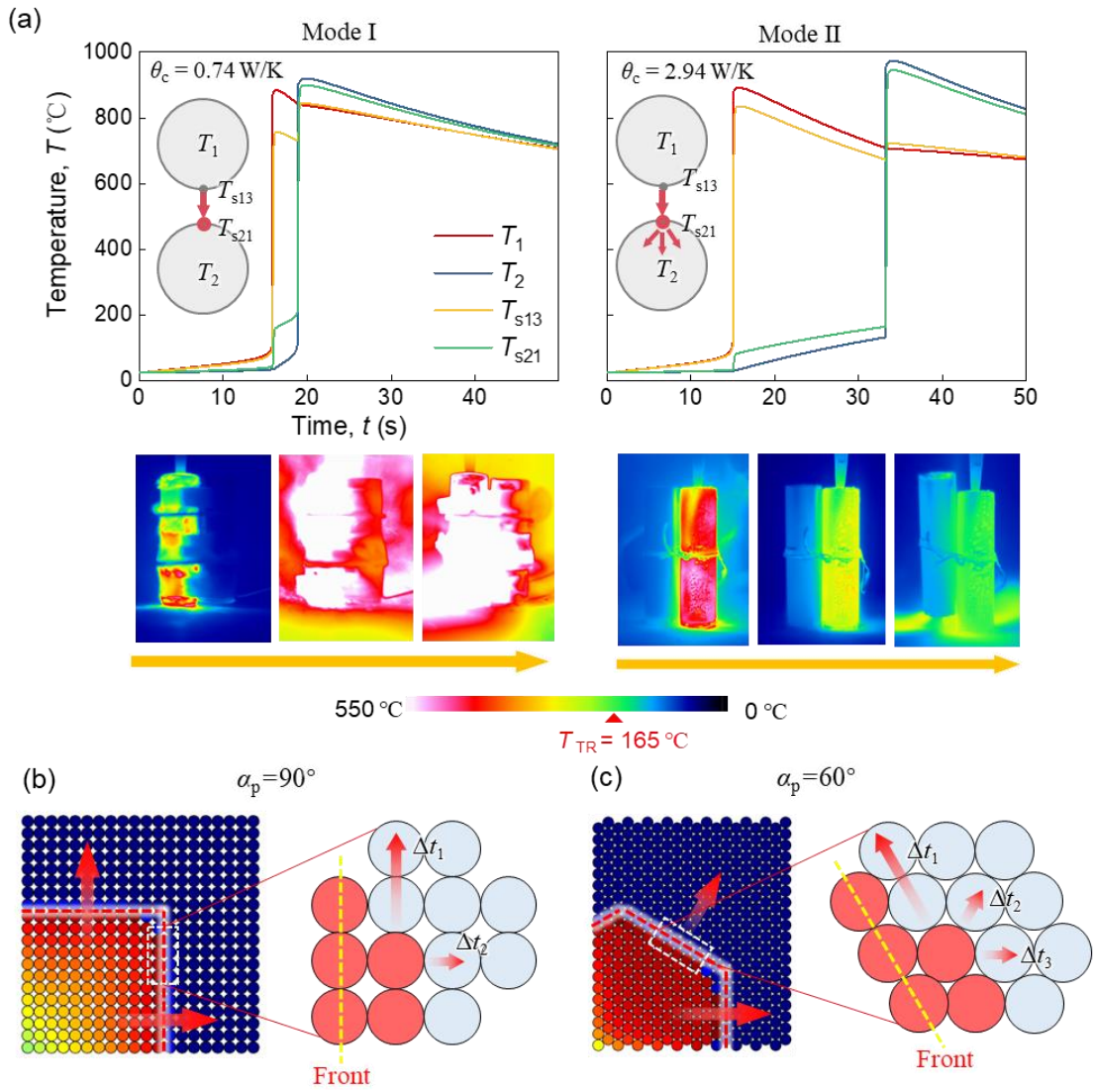


Figure 60 Typical phenomena and mechanisms of TR propagation when thermal contact changes. (a) simulation results:  $1 \times 2$  pack ( $\theta_c = 0.74$  W/K (or  $d = 0$  mm) and  $\theta_c = 2.94$  W/K (or  $d_p = \sim 0.01$  mm)); (b) propagation front of pack at  $\alpha_p = 90^\circ$  under mode II; (c) propagation front of pack at  $\alpha_p = 60^\circ$  under mode II.

In general, the spatial speed as the function of spacing  $d_p$ , and ambient temperature  $T_{amb}$  can be written as

$$v = f(d, T_{amb}) = f(K_c, T_{amb}) = f(K'_c, T') \quad (63)$$

where  $K_c$  is the equivalent thermal transfer coefficient,  $K'_c = K_c/K_c(d=0\text{mm})$  is the normalized equivalent thermal transfer coefficient,  $T'$  is the thermodynamic temperature.

Through parametric calculation, the following empirical formula can be obtained

$$v_n = 1.62(0.52 + 2.04 \times 10^{-6} e^{0.036T'}) (0.62K'_c)^{0.56} \quad (64)$$

The dimensionless propagation spatial speed  $v$  with  $d$  between 0~1mm and ambient temperature between  $-20^\circ\text{C}$ ~ $90^\circ\text{C}$  can be presented as Fig. 61 shown. Consider the relationship between spacing and thermal resistance,

$$K_c = 1/\theta_c = 1/(22.4d^{0.44}) \quad (65)$$

First, the TR propagation speed increases with  $T_{\text{amb}}$ , because a high  $T_{\text{amb}}$  corresponds to a high initial thermal energy within each battery. Second, the TR propagation speed increases when battery spacing  $d_p$  decreases. Decreasing  $d_p$  means decreasing the equivalent thermal resistance. The lower the thermal resistance, the quicker the heat transfer. The  $d_p$ ,  $T_{\text{amb}}$  decide together if TR propagation occurs, and its propagation speed (Fig.61).

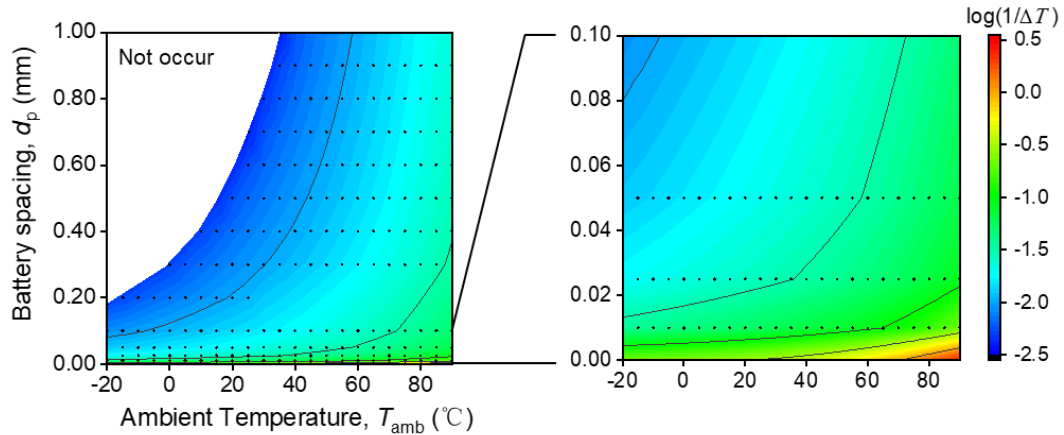


Figure 61 Schematic of the coupling effect of battery spacing and ambient temperature on TR propagation speed. The value  $\log(v)$  is used to indicate the TR propagation spatial speed.  $v$  is the propagation spatial speed and  $D$  is the diameter of the battery.

#### 6.2.4 Thermal runaway propagation under random thermal conditions

For actual battery packs, the thermal contact condition cannot be very even. Besides, the fire or explosion during the TR process, the thermal resistance or heat transfer coefficient may change. For example, the fire of a TR triggered battery could also heat the surrounding batteries expect for the thermal conduction and the thermal radiation. The equivalent heat transfer coefficient becomes large. Also, the explosion of a battery may push the surrounding batteries away. The equivalent heat transfer coefficient becomes smaller. Thus, battery packs with random equal heat transfer coefficients ( $K_c = 1/\theta_c$ ) between 0 W/K and 2.7 W/K were constructed. The average value of 1.35 W/K is the same as the battery packs with  $d_p = 0$  mm and  $\alpha_p = 90^\circ$  discussed above. Simulation results show that the TR propagations of the battery packs with random thermal coefficients are stable and little slower than the battery packs with even thermal coefficients (Fig.62a). Due to the uneven thermal contact condition, the TR cannot always propagation along a straight line, the spatial speed decreases (Fig.62b).

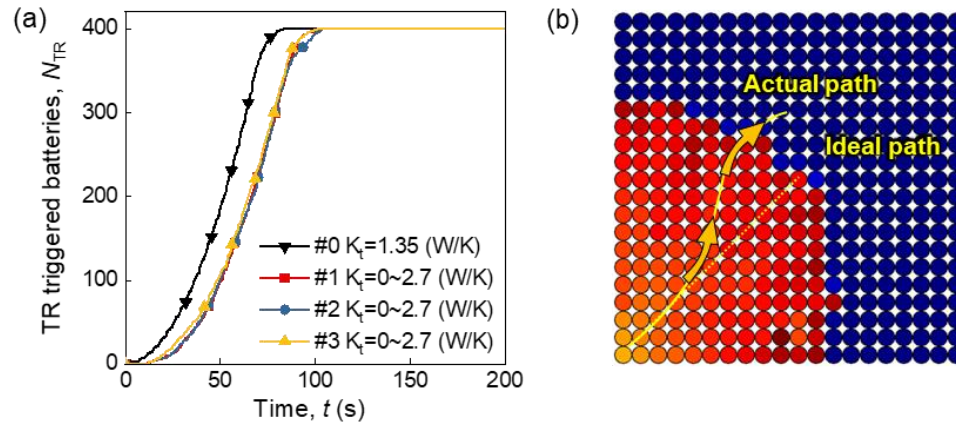


Figure 62 TR propagations under conditions with random thermal contacts among batteries. The equivalent thermal transfer coefficients are set as random between 0 W/K to 2.7 W/K (a)  $N-t$  curves and (b) their related possible propagation path.

### 6.3 Conclusions

In this chapter, the behavior and mechanisms of thermal runaway propagation within a battery pack are unlocked by a series of experiments and a TR propagation computational model. The experiments are conducted by mechanically triggering the TR of a specific-location battery in battery packs of various sizes. The computational model is established by combining the 0D TR, electrical, and thermal conduction models. Two typical modes of TR propagation are discovered, and their mechanisms are further provided through simulation.

- Mode I: under low  $\theta_c$ , a local overheating in the battery surface produces a local short circuit. This early-triggered ISC further accelerates the TR triggering.
- Mode II: under high  $\theta_c$ , conductive heat cannot concentrate on the battery surface. The surface and jellyroll average temperatures converge over time. When the temperatures reach the  $T_{TR}$ , the TR will be triggered inevitably. The total time of TR

propagation is significantly longer than that of Mode I. The batteries are mainly heated to  $T_{TR}$  by their surrounding TR-triggered batteries.

Within a large pack, the TR propagation front is approximately a circle based on Mode I, whereas it is a regular polygon based on Mode II. Numerical computation indicates that small packing space and high ambient temperature can increase the speed of TR propagation. Results provide theoretical insights into the fundamental understanding of TR propagation within battery packs of LIBs along with an efficient and effective computational frame for the safe design of battery packs.

Nonetheless, the simulation methods were idealized or simplify the calculation in this study. To accurately simulate a specific battery pack of an electric vehicle, more detail and difficult effects, such as the effect of fire and explosion, the effect of the cooling system, the effect of battery shape, should be further studied.

## CHAPTER 7 CONCLUDING REMARKS

In this work, we developed a systematic study of the multiphysics behavior safety risk evaluation of LIB cells. First, the concept of short circuit triggering risk was proposed. With the assistance of numerical simulation and experiments, we generate datasets and then establish an ML-based model to describe and predict the internal short circuit risk of a single cell upon mechanical abusive loading. The coefficient of determination  $R^2 > 0.90$  for the entire safety risk curve for both cylindrical cells and pouch cells was observed. The relative error of the average ISC prediction is less than 6.2%. Furthermore, the generalizability of the ML-based safety risk predictor was demonstrated by extending the scenarios for cells with various SOCs and loading conditions. Next, four safety risk levels were defined according to experimental results, and an ML battery safety risk classification model was developed. Our proposed method can accurately predict the safety risk level of the LIBs during cycling conditions in an efficient fashion. With the assistance of numerical simulation, about  $3 \times 10^5$  training samples have been generated, covering common SOC, short circuit resistance, and C-rate ranges. The model demonstrated a satisfactory performance (prediction score  $> 0.93$ ) and robustness (prediction scores  $> 0.87$  with a voltage error of 0.1 mV). Finally, based on the developed experimental methods, multiphysics modeling frameworks, two key safety issues, including defect within cells and TR propagation within packs were further investigated. In terms of defect cells, we discovered that capacity loss caused by deactivating components and current leakage

caused by internal minor short-circuits are two major indicators for defective batteries. The defect deteriorates the safety level of the cell due to the increased thermal stability and decreased mechanical integrity. In terms of TR propagation, we found two TR propagation modes that are determined by the thermal resistance between cells. The TR propagation mode significantly influences the propagation front shape and speed. This study systematically investigates the very fundamental issues, including ISC, TR, TR propagation, and defect based on experimental observation, multiphysics modeling, and proposed corresponding evaluation methods based on experimental data, numerical computation, and data-driven methodology.

This work highlights the promise of the multiphysics modeling framework and streamlines the methodology for understanding battery safety issues mechanical under abuse conditions. The related models and evaluation methods also provide an innovative solution for LIB safety design, safety risks evaluation, and safety risk monitoring.

## REFERENCES

1. Jia, Y.; Liu, B.; Hong, Z.; Yin, S.; Finegan, D. P.; Xu, J., Safety issues of defective lithium-ion batteries: identification and risk evaluation. *Journal of Materials Chemistry A* **2020**.
2. Xu, J.; Wang, L.; Guan, J.; Yin, S., Coupled effect of strain rate and solvent on dynamic mechanical behaviors of separators in lithium ion batteries. *Materials & Design* **2016**, *95*, 319-328.
3. Sahraei, E.; Kahn, M.; Meier, J.; Wierzbicki, T., Modelling of cracks developed in lithium-ion cells under mechanical loading. *RSC Advances* **2015**, *5* (98), 80369-80380.
4. Wierzbicki, T.; Sahraei, E., Homogenized mechanical properties for the jellyroll of cylindrical Lithium-ion cells. *Journal of Power Sources* **2013**, *241*, 467-476.
5. Greve, L.; Fehrenbach, C., Mechanical testing and macro-mechanical finite element simulation of the deformation, fracture, and short circuit initiation of cylindrical Lithium ion battery cells. *Journal of Power Sources* **2012**, *214*, 377-385.
6. Wu, H.; Zhuo, D.; Kong, D.; Cui, Y., Improving battery safety by early detection of internal shorting with a bifunctional separator. *Nature Communications* **2014**, *5* (1), 5193.
7. Bai, P.; Li, J.; Brushett, F. R.; Bazant, M. Z., Transition of lithium growth mechanisms in liquid electrolytes. *Energy & Environmental Science* **2016**, *9* (10), 3221-3229.
8. Weng, J.; Yang, X.; Ouyang, D.; Chen, M.; Zhang, G.; Wang, J., Comparative study on the transversal/lengthwise thermal failure propagation and heating position effect of lithium-ion batteries. *Appl. Energy* **2019**, *255*, 113761.
9. Ouyang, D.; Weng, J.; Hu, J.; Chen, M.; Huang, Q.; Wang, J., Experimental investigation of thermal failure propagation in typical lithium-ion battery modules. *Thermochimica Acta* **2019**, *676*, 205-213.
10. Wang, Q.; Ping, P.; Zhao, X.; Chu, G.; Sun, J.; Chen, C., Thermal runaway caused fire and explosion of lithium ion battery. *Journal of Power Sources* **2012**, *208*, 210-224.
11. Feng, X.; Fang, M.; He, X.; Ouyang, M.; Lu, L.; Wang, H.; Zhang, M., Thermal runaway features of large format prismatic lithium ion battery using extended volume accelerating rate calorimetry. *Journal of Power Sources* **2014**, *255*, 294-301.
12. Huang, P.; Ping, P.; Li, K.; Chen, H.; Wang, Q.; Wen, J.; Sun, J., Experimental and modeling analysis of thermal runaway propagation over the large format energy storage battery module with Li<sub>4</sub>Ti<sub>5</sub>O<sub>12</sub> anode. *Appl. Energy* **2016**, *183*, 659-673.
13. Larsson, F.; Anderson, J.; Andersson, P.; Mellander, B. E., Thermal Modelling of Cell-to-Cell Fire Propagation and Cascading Thermal Runaway Failure Effects for Lithium-Ion Battery Cells and Modules Using Fire Walls. *Journal of the Electrochemical Society* **2016**, *163* (14), A2854-A2865.

14. Liu, X.; Ren, D.; Hsu, H.; Feng, X.; Xu, G.-L.; Zhuang, M.; Gao, H.; Lu, L.; Han, X.; Chu, Z.; Li, J.; He, X.; Amine, K.; Ouyang, M., Thermal Runaway of Lithium-Ion Batteries without Internal Short Circuit. *Joule* **2018**, *2* (10), 2047-2064.
15. Feng, X.; Ouyang, M.; Liu, X.; Lu, L.; Xia, Y.; He, X., Thermal runaway mechanism of lithium ion battery for electric vehicles: A review. *Energy Storage Materials* **2018**, *10*, 246-267.
16. Zhang, X.; Sahraei, E.; Wang, K., Li-ion Battery Separators, Mechanical Integrity and Failure Mechanisms Leading to Soft and Hard Internal Shorts. *Sci Rep* **2016**, *6*, 32578.
17. Zhao, R.; Liu, J.; Gu, J., Simulation and experimental study on lithium ion battery short circuit. *Applied Energy* **2016**, *173*, 29-39.
18. Coman, P. T.; Darcy, E. C.; Veje, C. T.; White, R. E., Modelling Li-Ion Cell Thermal Runaway Triggered by an Internal Short Circuit Device Using an Efficiency Factor and Arrhenius Formulations. *Journal of The Electrochemical Society* **2017**, *164* (4), A587-A593.
19. Liu, B.; Jia, Y.; Li, J.; Yin, S.; Yuan, C.; Hu, Z.; Wang, L.; Li, Y.; Xu, J., Safety issues caused by internal short circuits in lithium-ion batteries. *Journal of Materials Chemistry A* **2018**, *6*, 21475-21484.
20. Abada, S.; Marlair, G.; Lecocq, A.; Petit, M.; Sauvant-Moynot, V.; Huet, F., Safety focused modeling of lithium-ion batteries: A review. *Journal of Power Sources* **2016**, *306*, 178-192.
21. Deng, J.; Bae, C.; Marcicki, J.; Masias, A.; Miller, T., Safety modelling and testing of lithium-ion batteries in electrified vehicles. *Nature Energy* **2018**, *3* (4), 261-266.
22. Abada, S.; Petit, M.; Lecocq, A.; Marlair, G.; Sauvant-Moynot, V.; Huet, F., Combined experimental and modeling approaches of the thermal runaway of fresh and aged lithium-ion batteries. *Journal of Power Sources* **2018**, *399*, 264-273.
23. Li, Y.; Cheng, X.; Zhang, Y.; Zhao, K., Recent advance in understanding the electro-chemo-mechanical behavior of lithium-ion batteries by electron microscopy. *Materials Today Nano* **2019**, *7*, 100040.
24. Lai, X.; Zheng, Y.; Zhou, L.; Gao, W., Electrical behavior of overdischarge-induced internal short circuit in lithium-ion cells. *Electrochimica Acta* **2018**, *278*, 245-254.
25. Guo, R.; Lu, L.; Ouyang, M.; Feng, X., Mechanism of the entire overdischarge process and overdischarge-induced internal short circuit in lithium-ion batteries. *Scientific Reports* **2016**, *6* (1), 30248.
26. Wang, E.; Wu, H.-P.; Chiu, C.-H.; Chou, P.-H., The Effect of Battery Separator Properties on Thermal Ramp, Overcharge and Short Circuiting of Rechargeable Li-Ion Batteries. *Journal of The Electrochemical Society* **2019**, *166* (2), A125-A131.
27. Avdeev, I.; Gilaki, M., Structural analysis and experimental characterization of

- cylindrical lithium-ion battery cells subject to lateral impact. *Journal of Power Sources* **2014**, *271*, 382-391.
28. Xu, J.; Liu, B. H.; Wang, L. B.; Shang, S., Dynamic mechanical integrity of cylindrical lithium-ion battery cell upon crushing. *Engineering Failure Analysis* **2015**, *53*, 97-110.
  29. Xu, J.; Liu, B. H.; Hu, D. Y., State of Charge Dependent Mechanical Integrity Behavior of 18650 Lithium-ion Batteries. *Sci Rep* **2016**, *6*, 21829.
  30. Xu, J.; Liu, B. H.; Wang, X. Y.; Hu, D. Y., Computational model of 18650 lithium-ion battery with coupled strain rate and SOC dependencies. *Appl. Energy* **2016**, *172*, 180-189.
  31. Yuan, C.; Wang, L.; Yin, S.; Xu, J., Generalized separator failure criteria for internal short circuit of lithium-ion battery. *Journal of Power Sources* **2020**, *467*, 228360.
  32. Wang, L.; Yin, S.; Xu, J., A detailed computational model for cylindrical lithium-ion batteries under mechanical loading: From cell deformation to short-circuit onset. *Journal of Power Sources* **2019**, *413*, 284-292.
  33. Xu, J.; Jia, Y.; Liu, B.; Zhao, H.; Yu, H.; Li, J.; Yin, S., Coupling Effect of State-of-Health and State-of-Charge on the Mechanical Integrity of Lithium-Ion Batteries. *Experimental Mechanics* **2018**, *58* (4), 633-643.
  34. Jia, Y.; Yin, S.; Liu, B.; Zhao, H.; Yu, H.; Li, J.; Xu, J., Unlocking the coupling mechanical-electrochemical behavior of lithium-ion battery upon dynamic mechanical loading. *Energy* **2019**, *166*, 951-960.
  35. Lai, W.-J.; Ali, M. Y.; Pan, J., Mechanical behavior of representative volume elements of lithium-ion battery modules under various loading conditions. *Journal of Power Sources* **2014**, *248*, 789-808.
  36. Sahraei, E.; Meier, J.; Wierzbicki, T., Characterizing and modeling mechanical properties and onset of short circuit for three types of lithium-ion pouch cells. *Journal of Power Sources* **2014**, *247*, 503-516.
  37. Zhang, C.; Santhanagopalan, S.; Sprague, M. A.; Pesaran, A. A., Coupled mechanical-electrical-thermal modeling for short-circuit prediction in a lithium-ion cell under mechanical abuse. *Journal of Power Sources* **2015**, *290*, 102-113.
  38. Marcicki, J.; Zhu, M.; Bartlett, A.; Yang, X. G.; Chen, Y.; Miller, T.; L'Eplattenier, P.; Caldichoury, I., A Simulation Framework for Battery Cell Impact Safety Modeling Using LS-DYNA. *Journal of The Electrochemical Society* **2017**, *164* (1), A6440-A6448.
  39. Li, W.; Xia, Y.; Zhu, J.; Luo, H., State-of-Charge Dependence of Mechanical Response of Lithium-Ion Batteries: A Result of Internal Stress. *Journal of The Electrochemical Society* **2018**, *165* (7), A1537-A1546.
  40. Xu, J.; Wu, Y.; Yin, S., Investigation of effects of design parameters on the internal short-circuit in cylindrical lithium-ion batteries. *RSC Advances* **2017**, *7* (24), 14360-14371.

41. Wang, M.; Le, A. V.; Noelle, D. J.; Shi, Y.; Meng, Y. S.; Qiao, Y., Internal-short-mitigating current collector for lithium-ion battery. *Journal of Power Sources* **2017**, *349*, 84-93.
42. Finegan, D. P.; Tjaden, B.; M. M. Heenan, T.; Jervis, R.; Michiel, M. D.; Rack, A.; Hinds, G.; Brett, D. J. L.; Shearing, P. R., Tracking Internal Temperature and Structural Dynamics during Nail Penetration of Lithium-Ion Cells. *Journal of The Electrochemical Society* **2017**, *164* (13), A3285-A3291.
43. Chiu, K.-C.; Lin, C.-H.; Yeh, S.-F.; Lin, Y.-H.; Chen, K.-C., An electrochemical modeling of lithium-ion battery nail penetration. *J. Power Sources* **2014**, *251*, 254-263.
44. Lu, L.; Han, X.; Li, J.; Hua, J.; Ouyang, M., A review on the key issues for lithium-ion battery management in electric vehicles. *Journal of Power Sources* **2013**, *226*, 272-288.
45. Liu, B.; Jia, Y.; Yuan, C.; Wang, L.; Gao, X.; Yin, S.; Xu, J., Safety issues and mechanisms of lithium-ion battery cell upon mechanical abusive loading: A review. *Energy Storage Materials* **2020**, *24*, 85-112.
46. Bandhauer, T. M.; Garimella, S.; Fuller, T. F., A Critical Review of Thermal Issues in Lithium-Ion Batteries. *Journal of the Electrochemical Society* **2011**, *158* (3), R1-R25.
47. Liu, B.; Zhang, J.; Zhang, C.; Xu, J., Mechanical integrity of 18650 lithium-ion battery module: Packing density and packing mode. *Engineering Failure Analysis* **2018**, *91*, 315-326.
48. Liu, B.; Zhao, H.; Yu, H.; Li, J.; Xu, J., Multiphysics computational framework for cylindrical lithium-ion batteries under mechanical abusive loading. *Electrochimica Acta* **2017**, *256*, 172-184.
49. Feng, X.; Ren, D.; He, X.; Ouyang, M., Mitigating Thermal Runaway of Lithium-Ion Batteries. *Joule* **2020**, *4* (4), 743-770.
50. Feng, X.; Fang, M.; He, X.; Ouyang, M.; Lu, L.; Wang, H.; Zhang, M. J. J. o. p. s., Thermal runaway features of large format prismatic lithium ion battery using extended volume accelerating rate calorimetry. **2014**, *255*, 294-301.
51. Wilke, S.; Schweitzer, B.; Khateeb, S.; Al-Hallaj, S. J. J. o. P. S., Preventing thermal runaway propagation in lithium ion battery packs using a phase change composite material: an experimental study. **2017**, *340*, 51-59.
52. Xia, Y.; Chen, G.; Zhou, Q.; Shi, X.; Shi, F., Failure behaviours of 100% SOC lithium-ion battery modules under different impact loading conditions. *Engineering Failure Analysis* **2017**, *82*, 149-160.
53. Zhu, J.; Luo, H.; Li, W.; Gao, T.; Xia, Y.; Wierzbicki, T., Mechanism of strengthening of battery resistance under dynamic loading. *International Journal of Impact Engineering* **2019**, *131*, 78-84.
54. Xu, J.; Liu, B.; Wang, X.; Hu, D., Computational model of 18650 lithium-ion battery with coupled strain rate and SOC dependencies. *Applied Energy* **2016**, *172*, 180-189.

55. Chen, X.; Wang, T.; Zhang, Y.; Ji, H.; Ji, Y.; Yuan, Q., Dynamic mechanical behavior of prismatic lithium-ion battery upon impact. *International Journal of Energy Research* **2019**, *43* (13), 7421-7432.
56. De Sutter, L.; Berckmans, G.; Marinaro, M.; Wohlfahrt-Mehrens, M.; Berecibar, M.; Van Mierlo, J., Mechanical behavior of Silicon-Graphite pouch cells under external compressive load: Implications and opportunities for battery pack design. *Journal of Power Sources* **2020**, *451*, 227774.
57. Keyser, M.; Darcy, E.; Long, D.; Pesaran, A., Passive safety device and internal short tested method for energy storage cells and systems. Google Patents: 2015.
58. Zhang, M. X.; Du, J. Y.; Liu, L. S.; Stefanopoulou, A.; Siegel, J.; Lu, L. G.; He, X. M.; Xie, X. Y.; Ouyang, M. G., Internal Short Circuit Trigger Method for Lithium-Ion Battery Based on Shape Memory Alloy. *Journal of the Electrochemical Society* **2017**, *164* (13), A3038-A3044.
59. Orendorff, C. J.; Roth, P.; Carmignani, C.; Langendorf, J.; Davis, L. In *External Triggers for Internal Short Circuits in Lithium Ion Batteries*, Meeting Abstracts, The Electrochemical Society: 2009; pp 1047-1047.
60. Sun, F.; Moroni, R.; Dong, K.; Markötter, H.; Zhou, D.; Hilger, A.; Zielke, L.; Zengerle, R.; Thiele, S.; Banhart, J.; Manke, I., Study of the Mechanisms of Internal Short Circuit in a Li/Li Cell by Synchrotron X-ray Phase Contrast Tomography. *ACS Energy Letters* **2017**, *2* (1), 94-104.
61. Zhao, R.; Liu, J.; Gu, J. J., A comprehensive study on Li-ion battery nail penetrations and the possible solutions. *Energy* **2017**, *123*, 392-401.
62. Fang, W.; Ramadass, P.; Zhang, Z., Study of internal short in a Li-ion cell-II. Numerical investigation using a 3D electrochemical-thermal model. *Journal of Power Sources* **2014**, *248*, 1090-1098.
63. Ramadass, P.; Fang, W.; Zhang, Z., Study of internal short in a Li-ion cell I. Test method development using infra-red imaging technique. *J. Power Sources* **2014**, *248*, 769-776.
64. Santhanagopalan, S.; Ramadass, P.; Zhang, J., Analysis of internal short-circuit in a lithium ion cell. *Journal of Power Sources* **2009**, *194* (1), 550-557.
65. Ouyang, M.; Zhang, M.; Feng, X.; Lu, L.; Li, J.; He, X.; Zheng, Y., Internal short circuit detection for battery pack using equivalent parameter and consistency method. *Journal of Power Sources* **2015**, *294*, 272-283.
66. Sahraei, E.; Hill, R.; Wierzbicki, T., Calibration and finite element simulation of pouch lithium-ion batteries for mechanical integrity. *Journal of Power Sources* **2012**, *201*, 307-321.
67. Finegan, D. P.; Scheel, M.; Robinson, J. B.; Tjaden, B.; Di Michiel, M.; Hinds, G.; Brett, D. J. L.; Shearing, P. R., Investigating lithium-ion battery materials during overcharge-induced thermal runaway: an operando and multi-scale X-ray CT study. *Physical Chemistry Chemical Physics* **2016**, *18* (45), 30912-30919.
68. Finegan, D. P.; Scheel, M.; Robinson, J. B.; Tjaden, B.; Hunt, I.; Mason, T.

- J.; Millichamp, J.; Di Michiel, M.; Offer, G. J.; Hinds, G.; Brett, D. J. L.; Shearing, P. R., In-operando high-speed tomography of lithium-ion batteries during thermal runaway. *Nature Communications* **2015**, *6* (1), 6924.
69. Hatchard, T.; D. MacNeil, D.; Basu, A.; R. Dahn, J., Thermal Model of Cylindrical and Prismatic Lithium-Ion Cells. *Journal of the Electrochemical Society* **2001**, *148*, A755-A761.
70. Kim, G.-H.; Pesaran, A.; Spotnitz, R., A three-dimensional thermal abuse model for lithium-ion cells. *J. Power Sources* **2007**, *170* (2), 476-489.
71. Finegan, D. P.; Darcy, E.; Keyser, M.; Tjaden, B.; Heenan, T. M. M.; Jarvis, R.; Bailey, J. J.; Malik, R.; Vo, N. T.; Magdysyuk, O. V.; Atwood, R.; Drakopoulos, M.; DiMichiel, M.; Rack, A.; Hinds, G.; Brett, D. J. L.; Shearing, P. R., Characterising thermal runaway within lithium-ion cells by inducing and monitoring internal short circuits. *Energy & Environmental Science* **2017**, *10* (6), 1377-1388.
72. Finegan, D. P.; Darst, J.; Walker, W.; Li, Q.; Yang, C.; Jarvis, R.; Heenan, T. M. M.; Hack, J.; Thomas, J. C.; Rack, A.; Brett, D. J. L.; Shearing, P. R.; Keyser, M.; Darcy, E., Modelling and experiments to identify high-risk failure scenarios for testing the safety of lithium-ion cells. *Journal of Power Sources* **2019**, *417*, 29-41.
73. Chen, M.; Dongxu, O.; Liu, J.; Wang, J., Investigation on thermal and fire propagation behaviors of multiple lithium-ion batteries within the package. *Applied Thermal Engineering* **2019**, *157*, 113750.
74. Feng, X.; Lu, L.; Ouyang, M.; Li, J.; He, X., A 3D thermal runaway propagation model for a large format lithium ion battery module. *Energy* **2016**, *115*, 194-208.
75. Feng, X.; He, X.; Ouyang, M.; Lu, L.; Wu, P.; Kulp, C.; Prasser, S., Thermal runaway propagation model for designing a safer battery pack with 25Ah LiNi<sub>x</sub>Co<sub>y</sub>Mn<sub>z</sub>O<sub>2</sub> large format lithium ion battery. *Appl. Energy* **2015**, *154*, 74-91.
76. Lee, C.; Said, A. O.; Stolarov, S. I., Impact of State of Charge and Cell Arrangement on Thermal Runaway Propagation in Lithium Ion Battery Cell Arrays. *Transportation Research Record* **2019**, *2673* (8), 408-417.
77. Wang, L.; Duan, X.; Liu, B.; Li, Q. M.; Yin, S.; Xu, J., Deformation and failure behaviors of anode in lithium-ion batteries: Model and mechanism. *Journal of Power Sources* **2019**, 227468.
78. Gao, S.; Lu, L.; Ouyang, M.; Duan, Y.; Zhu, X.; Xu, C.; Ng, B.; Kamyab, N.; White, R. E.; Coman, P. T., Experimental Study on Module-to-Module Thermal Runaway-Propagation in a Battery Pack. *Journal of The Electrochemical Society* **2019**, *166* (10), A2065-A2073.
79. Lamb, J.; Orendorff, C. J.; Steele, L. A. M.; Spangler, S. W., Failure propagation in multi-cell lithium ion batteries. *Journal of Power Sources* **2015**, *283*, 517-523.
80. F. Lopez, C.; A. Jeevarajan, J.; P. Mukherjee, P., Experimental Analysis of Thermal Runaway and Propagation in Lithium-Ion Battery Modules. *Journal of The*

- Electrochemical Society* **2015**, *162*, A1905-A1915.
81. Jia, Y.; Xu, J., Modeling of Thermal Propagation Based on Two Cylindrical Lithium-Ion Cells. *Journal of Electrochemical Energy Conversion and Storage* **2019**, *17* (2).
  82. Zhu, J.; Li, W.; Wierzbicki, T.; Xia, Y.; Harding, J., Deformation and failure of lithium-ion batteries treated as a discrete layered structure. *International Journal of Plasticity* **2019**, *121*, 293-311.
  83. Doyle, C. M.; Fuller, T. F.; Newman, J. S., Modeling of Galvanostatic Charge and Discharge of the Lithium/Polymer/Insertion Cell. *Journal of The Electrochemical Society* **1993**, *140*, 1526–1533.
  84. Fuller, T. F.; Doyle, M.; Newman, J., Simulation and optimization of the dual lithium ion insertion cell. *Journal of the Electrochemical Society* **1994**, *141* (1), 1-10.
  85. Doyle, C. M. Design and simulation of lithium rechargeable batteries. University of California, 1995.
  86. Smith, K. A.; Rahn, C. D.; Wang, C.-Y., Control oriented 1D electrochemical model of lithium ion battery. *Energy Conversion and Management* **2007**, *48* (9), 2565-2578.
  87. Hatchard, T. D.; MacNeil, D. D.; Basu, A.; Dahn, J. R., Thermal model of cylindrical and prismatic lithium-ion cells. *Journal of the Electrochemical Society* **2001**, *148* (7), A755-A761.
  88. Kim, G. H.; Pesaran, A.; Spotnitz, R., A three-dimensional thermal abuse model for lithium-ion cells. *J. Power Sources* **2007**, *170* (2), 476-489.
  89. Sahraei, E.; Campbell, J.; Wierzbicki, T., Modeling and short circuit detection of 18650 Li-ion cells under mechanical abuse conditions. *Journal of Power Sources* **2012**, *220*, 360-372.
  90. Zhang, X.; Wierzbicki, T., Characterization of plasticity and fracture of shell casing of lithium-ion cylindrical battery. *Journal of Power Sources* **2015**, *280*, 47-56.
  91. Zhu, J.; Zhang, X.; Sahraei, E.; Wierzbicki, T., Deformation and failure mechanisms of 18650 battery cells under axial compression. *Journal of Power Sources* **2016**, *336*, 332-340.
  92. Fu, R.; Xiao, M.; Choe, S.-Y., Modeling, validation and analysis of mechanical stress generation and dimension changes of a pouch type high power Li-ion battery. *Journal of Power Sources* **2013**, *224*, 211-224.
  93. Xu, J.; Liu, B.; Hu, D., State of Charge Dependent Mechanical Integrity Behavior of 18650 Lithium-ion Batteries. *Scientific Reports* **2016**, *6* (1), 21829.
  94. Guo, M.; Kim, G.-H.; White, R. E., A three-dimensional multi-physics model for a Li-ion battery. *Journal of Power Sources* **2013**, *240*, 80-94.
  95. Zhang, C.; Santhanagopalan, S.; Sprague, M. A.; Pesaran, A. A., A representative-sandwich model for simultaneously coupled mechanical-electrical-thermal simulation of a lithium-ion cell under quasi-static indentation tests. *Journal of Power Sources* **2015**, *298*, 309-321.
  96. Gao, X.; Lu, W.; Xu, J., Modeling framework for multiphysics-multiscale behavior of Si-C composite anode. *Journal of Power Sources* **2020**, *449*, 227501.

97. Deng, J.; Bae, C.; Miller, T.; L'Eplattenier, P.; Bateau-Meyer, S., Accelerate Battery Safety Simulations Using Composite Tshell Elements. *Journal of The Electrochemical Society* **2018**, *165* (13), A3067-A3076.
98. Yuan, C.; Gao, X.; Wong, H. K.; Feng, B.; Xu, J., A Multiphysics Computational Framework for Cylindrical Battery Behavior upon Mechanical Loading Based on LS-DYNA. *Journal of The Electrochemical Society* **2019**, *166* (6), A1160-A1169.
99. Naha, A.; Khandelwal, A.; Agarwal, S.; Tagade, P.; Hariharan, K. S.; Kaushik, A.; Yadu, A.; Kolake, S. M.; Han, S.; Oh, B., Internal short circuit detection in Li-ion batteries using supervised machine learning. *Sci Rep* **2020**, *10* (1), 1301.
100. Zhang, Y.; Tang, Q.; Zhang, Y.; Wang, J.; Stimming, U.; Lee, A. A., Identifying degradation patterns of lithium ion batteries from impedance spectroscopy using machine learning. *Nature Communications* **2020**, *11* (1), 1706.
101. Severson, K. A.; Attia, P. M.; Jin, N.; Perkins, N.; Jiang, B.; Yang, Z.; Chen, M. H.; Aykol, M.; Herring, P. K.; Fraggedakis, D.; Bazant, M. Z.; Harris, S. J.; Chueh, W. C.; Braatz, R. D., Data-driven prediction of battery cycle life before capacity degradation. *Nature Energy* **2019**, *4* (5), 383-391.
102. Shi, S.; Gao, J.; Liu, Y.; Zhao, Y.; Wu, Q.; Ju, W.; Ouyang, C.; Xiao, R., Multi-scale computation methods: Their applications in lithium-ion battery research and development. *Chinese Physics B* **2016**, *25* (1), 018212.
103. Liu, Y.; Guo, B.; Zou, X.; Li, Y.; Shi, S., Machine learning assisted materials design and discovery for rechargeable batteries. *Energy Storage Materials* **2020**, *31*, 434-450.
104. Feng, F.; Teng, S.; Liu, K.; Xie, J.; Xie, Y.; Liu, B.; Li, K., Co-estimation of lithium-ion battery state of charge and state of temperature based on a hybrid electrochemical-thermal-neural-network model. *Journal of Power Sources* **2020**, *455*, 227935.
105. Li, W.; Zhu, J.; Xia, Y.; Gorji, M. B.; Wierzbicki, T., Data-Driven Safety Envelope of Lithium-Ion Batteries for Electric Vehicles. *Joule* **2019**, *3* (11), 2703-2715.
106. Attia, P. M.; Grover, A.; Jin, N.; Severson, K. A.; Markov, T. M.; Liao, Y.-H.; Chen, M. H.; Cheong, B.; Perkins, N.; Yang, Z.; Herring, P. K.; Aykol, M.; Harris, S. J.; Braatz, R. D.; Ermon, S.; Chueh, W. C., Closed-loop optimization of fast-charging protocols for batteries with machine learning. *Nature* **2020**, *578* (7795), 397-402.
107. Xiong, R.; Ma, S.; Li, H.; Sun, F.; Li, J., Toward a Safer Battery Management System: A Critical Review on Diagnosis and Prognosis of Battery Short Circuit. *iScience* **2020**, *23* (4), 101010.
108. Xia, B.; Mi, C.; Chen, Z.; Robert, B. In *Multiple cell lithium-ion battery system electric fault online diagnostics*, 2015 IEEE Transportation Electrification Conference and Expo (ITEC), 14-17 June 2015; 2015; pp 1-7.
109. Feng, X.; Weng, C.; Ouyang, M.; Sun, J., Online internal short circuit

- detection for a large format lithium ion battery. *Appl. Energy* **2016**, *161*, 168-180.
110. Xiong, R.; Li, L.; Tian, J., Towards a smarter battery management system: A critical review on battery state of health monitoring methods. *Journal of Power Sources* **2018**, *405*, 18-29.
111. Jia, Y.; Li, J.; Yuan, C.; Gao, X.; Yao, W.; Lee, M.; Xu, J., Data-Driven Safety Risk Prediction of Lithium-Ion Battery. *Advanced Energy Materials* **2021**, 2003868.
112. Doyle, C. M., *Design and simulation of lithium rechargeable batteries*. 1995.
113. Wang, L.; Yin, S.; Zhang, C.; Huan, Y.; Xu, J., Mechanical characterization and modeling for anodes and cathodes in lithium-ion batteries. *Journal of Power Sources* **2018**, *392*, 265-273.
114. Wang, L.; Yin, S.; Yu, Z.; Wang, Y.; Yu, T. X.; Zhao, J.; Xie, Z.; Li, Y.; Xu, J., Unlocking the significant role of shell material for lithium-ion battery safety. *Materials & Design* **2018**, *160*, 601–610.
115. Liu, Y.; Wu, J. M.; Avdeev, M.; Shi, S. Q., Multi-Layer Feature Selection Incorporating Weighted Score-Based Expert Knowledge toward Modeling Materials with Targeted Properties. *Advanced Theory and Simulations* **2020**, *3* (2), 1900215.
116. Kecman, V., Support Vector Machines – An Introduction. In *Support Vector Machines: Theory and Applications*, Wang, L., Ed. Springer Berlin Heidelberg: Berlin, Heidelberg, 2005; pp 1-47.
117. Jia, Y.; Gao, X.; Mouillet, J.-B.; Terrier, J.-M.; Lombard, P.; Xu, J., Effective thermo-electro-mechanical modeling framework of lithium-ion batteries based on a representative volume element approach. *Journal of Energy Storage* **2020**, 102090.
118. Hong, Z.; Viswanathan, V., Phase-Field Simulations of Lithium Dendrite Growth with Open-Source Software. *ACS Energy Letters* **2018**, *3* (7), 1737-1743.
119. Liu, B.; Xu, J., Cracks of Silicon Nanoparticles in Anodes: Mechanics–Electrochemical-Coupled Modeling Framework Based on the Phase-Field Method. *ACS Applied Energy Materials* **2020**, *3* (11), 10931-10939.
120. Seo, M.; Goh, T.; Park, M.; Koo, G.; Kim, S., Detection of Internal Short Circuit in Lithium Ion Battery Using Model-Based Switching Model Method. *Energies* **2017**, *10* (1), 76.
121. Xia, B.; Chen, Z.; Mi, C.; Robert, B. In *External short circuit fault diagnosis for lithium-ion batteries*, 2014 IEEE Transportation Electrification Conference and Expo (ITEC), 2014; IEEE: 2014.
122. Chen, Z.; Xiong, R.; Lu, J.; Li, X., Temperature rise prediction of lithium-ion battery suffering external short circuit for all-climate electric vehicles application. *Appl. Energy* **2018**, *213*, 375-383.
123. Yang, R.; Xiong, R.; He, H.; Chen, Z., A fractional-order model-based battery external short circuit fault diagnosis approach for all-climate electric vehicles application. *Journal of Cleaner Production* **2018**, *187*, 950-959.
124. Feng, X.; Ren, D.; He, X.; Ouyang, M., Mitigating Thermal Runaway of

- Lithium-Ion Batteries. *Joule* **2020**, 4 (4), 28.
125. Zhou, H.; Yang, Z.; Xiao, D.; Xiao, K.; Li, J., An electrolyte to improve the deep charge–discharge performance of LiNi<sub>0.8</sub>Co<sub>0.15</sub>Al<sub>0.05</sub>O<sub>2</sub> cathode. *Journal of Materials Science Materials in Electronics* **2018**, 29 (8), 1-12.
  126. Spotnitz, R. M.; Weaver, J.; Yeduvaka, G.; Doughty, D. H.; Roth, E. P., Simulation of abuse tolerance of lithium-ion battery packs. *Journal of Power Sources* **2007**, 163 (2), 1080-1086.
  127. Maleki, H.; Shamsuri, A. K., Thermal analysis and modeling of a notebook computer battery. *Journal of Power Sources* **2003**, 115 (1), 131-136.
  128. Carrera, D. M., M. G., *Quantum Tunneling in Chemical Reactions*. 2007; Vol. 30.
  129. Coman, P.; Rayman, S.; E White, R., A lumped model of venting during thermal runaway in a cylindrical Lithium Cobalt Oxide lithium-ion cell. *Journal of Power Sources* **2016**, 307, 56–62.
  130. Coman, P. T.; Darcy, E. C.; Veje, C. T.; White, R. E., Numerical analysis of heat propagation in a battery pack using a novel technology for triggering thermal runaway. *Appl. Energy* **2017**, 203, 189-200.
  131. Golubkov, A. W.; Fuchs, D.; Wagner, J.; Wiltsche, H.; Stangl, C.; Fauler, G.; Voitic, G.; Thaler, A.; Hacker, V., Thermal-runaway experiments on consumer Li-ion batteries with metal-oxide and olivin-type cathodes. *RSC Advances* **2014**, 4 (7), 3633-3642.

### APPENDIX A: Support Vector Regression Problem

Given training vectors  $x_i \in \mathbb{R}^p$ ,  $i=1,2,\dots, n$ , and a vector  $y_i \in \mathbb{R}^p$ ,  $\varepsilon$ -SVR solves the following primal problem:

$$\min_{w,b,\zeta,\zeta^*} \frac{1}{2} w^T w + C \sum_{i=1}^n (\zeta_i + \zeta_i^*), \quad (\text{A1})$$

and subject to

$$\begin{cases} y_i - w^T \phi(x_i) - b \leq \varepsilon_{\text{SVR}} + \zeta_i \\ w^T \phi(x_i) + b - y_i \leq \varepsilon_{\text{SVR}} + \zeta_i^* \\ \zeta_i, \zeta_i^* \geq 0, i = 1, \dots, n \end{cases} \quad (\text{A2})$$

Samples whose prediction is at least  $\varepsilon$  away from their true target will be penalized. These samples penalize the objective by  $\zeta_i$  or  $\zeta_i^*$ , depending on whether their predictions lie above or below the  $\varepsilon$  tube.

The dual problem is

$$\min_{\beta, \beta^*} \frac{1}{2} (\beta - \beta^*)^T P (\beta - \beta^*) + \varepsilon_{\text{SVR}} e^T (\beta + \beta^*) - y^T (\beta - \beta^*), \quad (\text{A3})$$

subject to

$$\begin{cases} e^T (\beta - \beta^*) = 0 \\ 0 \leq \beta_i, \beta_i^* \leq C_{\text{SVR}}, i = 1, \dots, n \end{cases} \quad (\text{A4})$$

where  $e$  is the vector of all ones,  $P_{ij} = \phi(x_i)^T \phi(x_j)$  is the kernel. The prediction is

$$\sum_{i \in \text{SV}} (\beta_i - \beta_i^*) P_{ij} + b, \quad (\text{A5})$$

## APPENDIX B: Multiphysics Model Setups for Data Generation

### 1) 1-D lithium-ion battery model<sup>48</sup>

The geometry and boundary conditions of the battery are shown in Fig. 63.

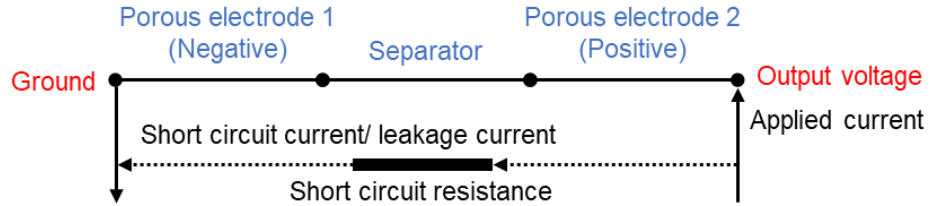


Figure 63 Model setups of the battery model

### 2) 3-D heat transfer model and short circuit considerations

The boundary conditions were set the Fig. 64 shows.

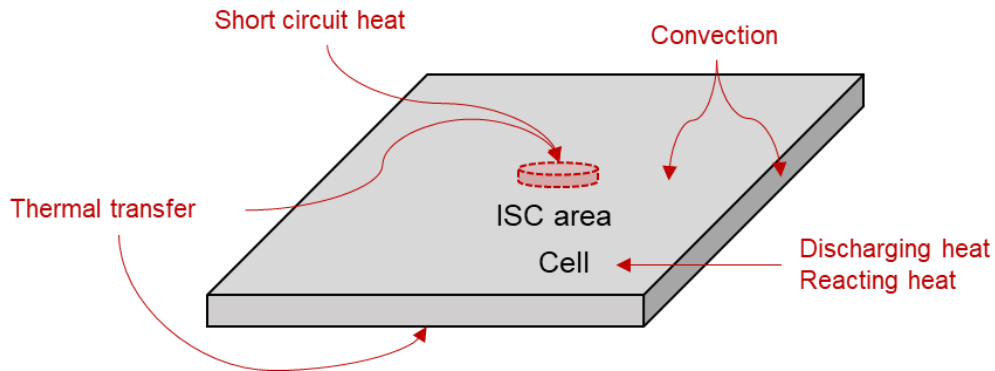


Figure 64 Boundary conditions of the thermal model

The short circuit joule heat  $Q_{short}$  is<sup>65</sup>

$$Q_{short} = I_{short}^2 R_{short}, \quad (B1)$$

where the current  $I$  comes from the battery model.  $Q_{cell}$  is the heat produced by the cell during the discharging process.  $Q_{conv}$  is the thermal convection:

$$Q_{conv} = S_c h_{conv} (T - T_{amb}), \quad (B2)$$

where  $S_c$  is the free surface area,  $T_{amb}$  is the ambient temperature,  $h_{conv}$  thermal convection coefficient, here set as 10 W/(m<sup>2</sup>K). Considering that the cell will expand and

explosion when the TR is triggered,  $h_{conv}$  is modified as

$$h_{convc} = \begin{cases} h_{conv0} = 10 \text{ W} / (\text{m}^2 \text{K}) & (\text{Before TR}) \\ h_{conv1} = 500 \text{ W} / (\text{m}^2 \text{K}) & (\text{TR triggered}) \end{cases}, \quad (\text{B3})$$

where  $h_{conv1}$  is modified to make the temperature curve in decreasing stage match the experimental results.  $Q_{trans}$  is the heat transfer between the cell and the fixture/ indenter:

$$Q_{trans} = S_t h_t (T - T_{amb}), \quad (\text{B4})$$

where  $S_t$  is the total contact area,  $h_t$  is an equivalent coefficient that is set as  $40[\text{W}/(\text{m}^2\text{K})]$ .

#### 4) Thermal runaway model <sup>18, 75, 129</sup>

(a) SEI decomposition, the total rate equals the sum of the decomposition rate and the generation rate:

$$\frac{dc_s}{dt} = \frac{dc_{s,d}}{dt} + \frac{dc_{s,g}}{dt}, \quad (\text{B5})$$

The decomposition rate is:

$$\frac{dc_{s,d}}{dt} = -A_s \exp\left(\frac{-E_s}{RT}\right) c_{s,d}, \quad (\text{B6})$$

The generation rate is:

$$\frac{dc_{s,g}}{dt} = K_{s,g} c_{s,g}, \quad (\text{B7})$$

(b) The reaction between cathode and electrolyte:

$$\frac{d\alpha_c}{dt} = A_c \alpha_c (1 - \alpha_c) \exp\left(\frac{-E_c}{R_g T}\right), \quad (\text{B8})$$

(c) Electrolyte decomposition:

$$\frac{dc_e}{dt} = -A_e \exp\left(\frac{-E_e}{R_g T}\right) c_e, \quad (\text{B9})$$

(d) Anode decomposition

$$\frac{dc_a}{dt} = -A_a \exp\left(\frac{-c_s}{c_{s0}}\right) \exp\left(\frac{-E_a}{R_g T}\right) c_a, \quad (\text{B10})$$

(e) Separator decomposition

$$\frac{dc_{\text{sep}}}{dt} = -A_{\text{sep}} \exp\left(\frac{-E_{\text{sep}}}{R_g T}\right) c_{\text{sep}}, \quad (\text{B11})$$

(f) The intense ISC caused by separator collapse and direct contact between anode and cathode:

$$\frac{dSoC}{dt} = -A_e \exp\left(\frac{-E_e}{R_g T}\right) SoC - \frac{i}{C}, \quad (\text{B12})$$

where  $\frac{i}{C}$  is a modification term for SOC.

The heat generation rates are equal to:

$$\begin{aligned} \frac{dQ_x}{dt} &= h_x m_x \frac{dc_x}{dt} (T > T_{c,x}) \\ \frac{dQ}{dt} &= \sum \frac{dQ_x}{dt} \end{aligned}, \quad (\text{B13})$$

where  $H_x$  is the reaction enthalpy,  $m_x$  is the mass density,  $T_{c,x}$  is triggering temperature. For Eqn. 18,  $H_x$  can be estimated by:

$$H_{ec} = 3600U^2C\eta, \quad (\text{B14})$$

where  $U$  is the nominal voltage,  $C$  is capacity,  $\eta$  is the thermal efficiency, set as 0.5.

## APPENDIX C: Feature Analysis for Safety Risk Classification

## a) Feature importance analysis

For C1:

(1)  $du/dt|_{t=t_0}$  and  $du/dt|_{t=t_0-\Delta t}$  are proportional to the  $i$ :

$$\frac{du}{dt} \propto \left( \frac{dSoC}{dt} = \frac{i}{C} \right), \quad (C1)$$

where  $C$  is the capacity of the battery. The voltage slope difference between a defective battery and a normal battery is

$$\left( \frac{du}{dt} \Big|_{t=t_0} - \frac{du}{dt} \Big|_{t=t_0-\Delta t} \right) \propto \frac{i_{leak}}{C}, \quad (C2)$$

where  $i_{leak} = u / R$  is the leakage current.

(2)  $u(t_0)$  and  $u(t_0 - \Delta t)$  contain  $i_{leak}$  information as:

$$u(t) - u(t_0 - \Delta t) = \left( u(SoC(t_0)) - u(SoC(t_0) - \frac{i - i_{sc}}{i} \Delta t) \right) \propto \frac{\Delta u}{\Delta SoC} \frac{i - i_{sc}}{i} \Delta t, \quad (C3)$$

(3)  $\int_{t_0-\Delta t}^{t_0} u(t)dt$  is equal to:

$$\int_{t-\Delta t}^t u(t)dt \propto \left( \int_{t-\Delta t}^t \frac{u(t)}{R} dt = Q_{leak} \right), \quad (C4)$$

where  $Q_{leak}$  is the leakage capacity.

(4)  $i(t_0)$  and  $i(t_0 - \Delta t)$  influence voltage differences (Eq. C3) and contain information about battery SoC:

$$SoC = f(u, i). \quad (C5)$$

For C2:

(1)  $u(t_0)$  is highly related to SOC (Eq. 23). Based on the feature start voltage and start current (or current integration), the initial electrochemical state can be determined.

Also, it is related to  $R_{short}$  because the voltage changes when the cell is connected to

$R_{short}$ :

$$u(t_0) = \frac{R_{\text{short}}}{R_{\text{short}} + R_0} u(t_0 - \Delta t), \quad (\text{C6})$$

where  $u(t_0 - \Delta t)$  is the voltage before the short circuit.

(2)  $du/dt|_{t=t_0}$  is related to  $R_{\text{short}}$  :

$$\frac{du}{dt} \propto \frac{\Delta u}{\Delta t} \propto u(t_0) - u(t_0 - \Delta t) = \frac{R_{\text{short}}}{R_{\text{short}} + R_0} u(t_0 - \Delta t) - u(t_0 - \Delta t) = -\frac{R_0}{R_{\text{short}} + R_0} u(t_0 - \Delta t) \quad . \quad (\text{C7})$$

### b) Robustness analysis

Take C1, for example. Consider the classification is based on two of the most important features, *i.e.*, voltage and voltage difference:

$$\begin{aligned} \Delta u &= u(t_0) - u(t_0 - \Delta t) = u(\text{SoC}(t_0)) - u(\text{SoC}(t_0 - \Delta t)) \\ &= u(\text{SoC}(t_0)) - u(\text{SoC}(t_0) - \Delta t_l \frac{i - u}{i}) \\ &\sim \frac{iR - u}{iR} \frac{\Delta u}{\Delta \text{SoC}} \Delta t_l, \\ &\sim \frac{\Delta u}{\Delta \text{SoC}} \Delta t_l - \frac{u}{iR} \frac{\Delta u}{\Delta \text{SoC}} \Delta t_l \end{aligned} \quad , \quad (\text{C8})$$

Define the voltage slope difference between a damaged cell and a normal cell  $\delta$  is:

$$\delta = (u'(t_0) - u'(t_0 - \Delta t)) - (u(t_0) - u(t_0 - \Delta t)), \quad (\text{C9})$$

where  $u'(t_0)$  represents the signal from the damaged cell. The order of magnitude of  $d$  is

$$o(\delta) = o(\Delta(\frac{\Delta u}{\Delta \text{SoC}} \Delta t_l - \frac{u}{iR} \frac{\Delta u}{\Delta \text{SoC}} \Delta t_l)) = o(\frac{1}{iR} \frac{(\Delta u)^2}{\Delta \text{SoC}} \Delta t_l), \quad (\text{C10})$$

Since  $\Delta(\Delta u) \approx 0$ , when  $i_e$  is introduced, the order of magnitude of  $\delta$  changes to

$$o(\delta') = o(\delta) + o(\frac{i_e}{i^2} \frac{1}{R} \frac{(\Delta u)^2}{\Delta \text{SoC}} \Delta t_l). \quad (\text{C11})$$

The magnitude of the relative difference is

$$o(\Delta\delta) = \frac{o(\delta') - o(\delta)}{o(\delta)} = o\left(\frac{i_e}{i}\right), \quad (\text{C12})$$

Thus, the accuracy will only be affected when the order of magnitude of  $i_e$  is close to  $i$ . For voltage error  $u_e$ , according to Eq. C10, the order of magnitude of  $d$  changes to:

$$o(\delta'') = o(\delta) + o(u_e), \quad (\text{C13})$$

Here, we can simply select a common sample and obtain the corresponding values,

$$\begin{cases} i = 3.7\text{A} \\ \Delta u = 0.11\text{V} \\ \Delta\text{SoC} = \frac{1}{6} \\ R = 100\ \Omega \end{cases}, \quad (\text{C14})$$

And

$$o(\delta) = o\left(\frac{0.11\text{V}}{3.7\text{A} \times 100\ \Omega} \frac{0.11\text{V}}{1/6}\right) = o(10^{-5}\ \text{V}), \quad (\text{C15})$$

### c) Parametric analysis

According to Eq. 28,  $o(\delta) = (o\Delta t_i \Delta u / iR \cdot (\Delta u / \Delta\text{SoC}))$ . Here,  $\Delta u / \Delta\text{SoC}$  (slope of  $u - \text{SoC}$  curve) changes little. When  $i$  and  $R$  remain unchanged, and  $\Delta t_i$  increases,  $\Delta u$  and  $\delta$  will increase., which means the differences are easier to be captured.

#### APPENDIX D: Calculation of Steady-state Temperature of Defective Cell

The steady-state temperature can be estimated theoretically based on the defected battery equivalent circuit and thermal dynamic equation as

$$\rho V C_p \frac{dT}{dt} = \dot{Q}_j + \dot{Q}_h + \dot{Q}_r, \quad (D1)$$

where  $C_p$  is the specific thermal capacity of the battery,  $\rho$  is the density of the battery,  $V$  is the volume of the battery,  $T$  is the battery temperature,  $\dot{Q}_j$  is the joule heat power,  $\dot{Q}_h$  is the thermal convection power, and  $\dot{Q}_r$  is the thermal radiation power. According to Ohm's law,

$$I_s = \frac{E}{R_s + R_0}, \quad (D2)$$

where  $I_s$  is the short-circuit current (current leakage),  $R_s$  is the short-circuit resistance,  $R_0$  is the internal resistance and  $E$  is the potential of the cell. The charging current  $I_d$  is equal to the sum of short-circuit current and current through the electrodes  $I_0$ :

$$I_d = I_s + I_0, \quad (D3)$$

According to Joule's law,

$$\dot{Q}_j = I_s^2 (R_s + R_0), \quad (D4)$$

The thermal convection power is

$$\dot{Q}_h = (T - T_{amb}) h A, \quad (D5)$$

where  $T_{amb}$  is the ambient temperature,  $h$  is the air convection coefficient and  $A$  is the convection area. The thermal radiation power is

$$\dot{Q}_r = (T^4 - T_{amb}^4) \sigma \varepsilon A, \quad (D6)$$

where  $\sigma$  is the surface emissivity and  $\varepsilon$  is the Stefan-Boltzmann constant.

For steady-state condition,

$$\frac{dT}{dt} = 0, \quad (D7)$$

Solving the equations we can obtain  $T = T_s$ .

## APPENDIX E: PERMISSION LETTERS

Here are the licenses for reusing the contents from my previous publications.



This is a License Agreement between Yikai Jia ("User") and Copyright Clearance Center, Inc. ("CCC") on behalf of the Rightsholder identified in the order details below. The license consists of the order details, the CCC Terms and Conditions below, and any Rightsholder Terms and Conditions which are included below.

All payments must be made in full to CCC in accordance with the CCC Terms and Conditions below.

|                  |             |             |                                    |
|------------------|-------------|-------------|------------------------------------|
| Order Date       | 09-Mar-2022 | Type of Use | Republish in a thesis/dissertation |
| Order License ID | 1197401-1   | Publisher   | Royal Society of Chemistry         |
| ISSN             | 2050-7488   | Portion     | Chapter/article                    |

## LICENSED CONTENT

|                   |  |                  |                            |
|-------------------|--|------------------|----------------------------|
| Publication Title | Journal of materials chemistry, A, Materials for energy and sustainability           | Rightsholder     | Royal Society of Chemistry |
| Article Title     | Safety Issues of Defective Lithium-ion Batteries: Identification and Risk Evaluation | Publication Type | Journal                    |
| Author/Editor     | Royal Society of Chemistry (Great Britain)   | Start Page       | 12472                      |
| Date              | 01/01/2012   | End Page         | 12484                      |
| Language          | English  | Issue            | 25                         |
| Country           | United Kingdom of Great Britain and Northern Ireland                                 | Volume           | 8                          |

## REQUEST DETAILS

|                                 |                         |                             |                                  |
|---------------------------------|-------------------------|-----------------------------|----------------------------------|
| Portion Type                    | Chapter/article         | Rights Requested            | Main product                     |
| Page range(s)                   | 12472                   | Distribution                | United States                    |
| Total number of pages           | 13                      | Translation                 | Original language of publication |
| Format (select all that apply)  | Electronic              | Copies for the disabled?    | No                               |
| Who will republish the content? | Publisher, for profit   | Minor editing privileges?   | No                               |
| Duration of Use                 | Life of current edition | Incidental promotional use? | No                               |
| Lifetime Unit Quantity          | Up to 499               | Currency                    | USD                              |

## NEW WORK DETAILS

|                 |  |                            |               |
|-----------------|--|----------------------------|---------------|
| Title           | SCIENCE MULTIPHYSICS NATURE OF LITHIUM-ION BATTERY SAFETY ISSUES | Institution name           | UNC Charlotte |
| Instructor name | Yikai Jia  | Expected presentation date | 2022-04-01    |

## ADDITIONAL DETAILS

|                        |     |   |           |
|------------------------|-----|---|-----------|
| Order reference number | N/A | The requesting person / organization to appear on the license | Yikai Jia |
|------------------------|-----|---|-----------|

## REUSE CONTENT DETAILS

|   |  |  |  |
|---|--|--|--|
| Title, description or numeric reference of the portion(s) | SCIENCE MULTIPHYSICS<br>NATURE OF LITHIUM-ION<br>BATTERY SAFETY ISSUES | Title of the article/chapter the portion is from | Safety Issues of Defective Lithium-ion Batteries: Identification and Risk Evaluation |
| Editor of portion(s)                                      | Jia, Yikai; Xu, Jun  | Author of portion(s)                             | Jia, Yikai; Liu, Binghe; Hong, Zhiguo; Yin, Sha; Finegan, Donal P; Xu, Jun           |
| Volume of serial or monograph                             | 8  | Issue, if republishing an article from a serial  | 25   |
| Page or page range of portion                             | 12472-12484  | Publication date of portion                      | 2022-04-11   |

## SPECIAL RIGHTSHOLDER TERMS AND CONDITIONS

Permission is granted as long as the article is fully acknowledged and a link is given back to the article on our Platform. Please go to [rsc.li/permissions](https://rsc.li/permissions) for details. Please note that if the material specified above or any part of it appears with credit or acknowledgement to a third party then you must also secure permission from that third party before reproducing that material.

## CCC Terms and Conditions

- Description of Service; Defined Terms. This Republication License enables the User to obtain licenses for republication of one or more copyrighted works as described in detail on the relevant Order Confirmation (the "Work(s)"). Copyright Clearance Center, Inc. ("CCC") grants licenses through the Service on behalf of the rightsholder identified on the Order Confirmation (the "Rightsholder"). "Republication", as used herein, generally means the inclusion of a Work, in whole or in part, in a new work or works, also as described on the Order Confirmation. "User", as used herein, means the person or entity making such republication.
- The terms set forth in the relevant Order Confirmation, and any terms set by the Rightsholder with respect to a particular Work, govern the terms of use of Works in connection with the Service. By using the Service, the person transacting for a republication license on behalf of the User represents and warrants that he/she/it (a) has been duly authorized by the User to accept, and hereby does accept, all such terms and conditions on behalf of User, and (b) shall inform User of all such terms and conditions. In the event such person is a "freelancer" or other third party independent of User and CCC, such party shall be deemed jointly a "User" for purposes of these terms and conditions. In any event, User shall be deemed to have accepted and agreed to all such terms and conditions if User republishes the Work in any fashion.
- Scope of License; Limitations and Obligations.
  - All Works and all rights therein, including copyright rights, remain the sole and exclusive property of the Rightsholder. The license created by the exchange of an Order Confirmation (and/or any invoice) and payment by User of the full amount set forth on that document includes only those rights expressly set forth in the Order Confirmation and in these terms and conditions, and conveys no other rights in the Work(s) to User. All rights not expressly granted are hereby reserved.
  - General Payment Terms: You may pay by credit card or through an account with us payable at the end of the month. If you and we agree that you may establish a standing account with CCC, then the following terms apply: Remit Payment to: Copyright Clearance Center, 29118 Network Place, Chicago, IL 60673-1291. Payments Due: Invoices are payable upon their delivery to you (or upon our notice to you that they are



This is a License Agreement between Yikai Jia ("User") and Copyright Clearance Center, Inc. ("CCC") on behalf of the Rightsholder identified in the order details below. The license consists of the order details, the CCC Terms and Conditions below, and any Rightsholder Terms and Conditions which are included below.

All payments must be made in full to CCC in accordance with the CCC Terms and Conditions below.

|                         |             |                    |                                    |
|-------------------------|-------------|--------------------|------------------------------------|
| <b>Order Date</b>       | 09-Mar-2022 | <b>Type of Use</b> | Republish in a thesis/dissertation |
| <b>Order License ID</b> | 1197401-2   | <b>Publisher</b>   | WILEY - VCH VERLAG GMBH & CO.      |
| <b>ISSN</b>             | 1614-6832   | <b>Portion</b>     | Chapter/article                    |

## LICENSED CONTENT

|                          |   |                         |                           |
|--------------------------|---|-------------------------|---------------------------|
| <b>Publication Title</b> | Advanced Energy Materials                                 | <b>Rightsholder</b>     | John Wiley & Sons - Books |
| <b>Article Title</b>     | Data-Driven Safety Risk Prediction of Lithium-Ion Battery | <b>Publication Type</b> | Journal                   |
| <b>Author/Editor</b>     | Wiley-VCH.  | <b>Start Page</b>       | 2003868                   |
| <b>Date</b>              | 01/01/2011  | <b>Issue</b>            | 18                        |
| <b>Language</b>          | English   | <b>Volume</b>           | 11                        |
| <b>Country</b>           | United Kingdom of Great Britain and Northern Ireland      |                         |                           |

## REQUEST DETAILS

|  |   |                                    |                                  |
|--|---|------------------------------------|----------------------------------|
| <b>Portion Type</b>                    | Chapter/article                         | <b>Rights Requested</b>            | Main product                     |
| <b>Page range(s)</b>                   | 1                                       | <b>Distribution</b>                | United States                    |
| <b>Total number of pages</b>           | 12                                      | <b>Translation</b>                 | Original language of publication |
| <b>Format (select all that apply)</b>  | Electronic                              | <b>Copies for the disabled?</b>    | No                               |
| <b>Who will republish the content?</b> | Publisher, for profit                   | <b>Minor editing privileges?</b>   | No                               |
| <b>Duration of Use</b>                 | Life of current and all future editions | <b>Incidental promotional use?</b> | No                               |
| <b>Lifetime Unit Quantity</b>          | Up to 499                               | <b>Currency</b>                    | USD                              |

## NEW WORK DETAILS

|                        |  |                                   |               |
|------------------------|--|-----------------------------------|---------------|
| <b>Title</b>           | SCIENCE MULTIPHYSICS NATURE OF LITHIUM-ION BATTERY SAFETY ISSUES | <b>Institution name</b>           | UNC Charlotte |
| <b>Instructor name</b> | Yikai Jia  | <b>Expected presentation date</b> | 2022-04-01    |

## ADDITIONAL DETAILS

The requesting person / organization to appear on the license Yikai Jia

## REUSE CONTENT DETAILS

|   |  |  |  |
|---|--|--|--|
| Title, description or numeric reference of the portion(s) | SCIENCE MULTIPHYSICS<br>NATURE OF LITHIUM-ION<br>BATTERY SAFETY ISSUES | Title of the article/chapter the portion is from | Data-Driven Safety Risk<br>Prediction of Lithium-Ion<br>Battery                              |
| Editor of portion(s)                                      | Jia, Yikai; Xu, Jun  | Author of portion(s)                             | Jia, Yikai; Li, Jiani; Yuan,<br>Chunhao; Gao, Xiang; Yao,<br>Weiran; Lee, Minwoo; Xu,<br>Jun |
| Volume of serial or monograph                             | 11   |  |  |
| Page or page range of portion                             | 2003868 (1-12)   | Publication date of portion                      | 2021-03-24   |

## RIGHTSHOLDER TERMS AND CONDITIONS

No right, license or interest to any trademark, trade name, service mark or other branding ("Marks") of WILEY or its licensors is granted hereunder, and you agree that you shall not assert any such right, license or interest with respect thereto. You may not alter, remove or suppress in any manner any copyright, trademark or other notices displayed by the Wiley material. This Agreement will be void if the Type of Use, Format, Circulation, or Requestor Type was misrepresented during the licensing process. In no instance may the total amount of Wiley Materials used in any Main Product, Compilation or Collective work comprise more than 5% (if figures/tables) or 15% (if full articles/chapters) of the (entirety of the) Main Product, Compilation or Collective Work. Some titles may be available under an Open Access license. It is the Licensors' responsibility to identify the type of Open Access license on which the requested material was published, and comply fully with the terms of that license for the type of use specified. Further details can be found on Wiley Online Library <http://olabout.wiley.com/WileyCDA/Section/id-410895.html>.

## CCC Terms and Conditions

1. Description of Service; Defined Terms. This Republication License enables the User to obtain licenses for republication of one or more copyrighted works as described in detail on the relevant Order Confirmation (the "Work(s)"). Copyright Clearance Center, Inc. ("CCC") grants licenses through the Service on behalf of the rightsholder identified on the Order Confirmation (the "Rightsholder"). "Republication", as used herein, generally means the inclusion of a Work, in whole or in part, in a new work or works, also as described on the Order Confirmation. "User", as used herein, means the person or entity making such republication.
2. The terms set forth in the relevant Order Confirmation, and any terms set by the Rightsholder with respect to a particular Work, govern the terms of use of Works in connection with the Service. By using the Service, the person transacting for a republication license on behalf of the User represents and warrants that he/she/it (a) has been duly authorized by the User to accept, and hereby does accept, all such terms and conditions on behalf of User, and (b) shall inform User of all such terms and conditions. In the event such person is a "freelancer" or other third party independent of User and CCC, such party shall be deemed jointly a "User" for purposes of these terms and conditions. In any event, User shall be deemed to have accepted and agreed to all such terms and conditions if User republishes the Work in any fashion.
3. Scope of License; Limitations and Obligations.
  - 3.1. All Works and all rights therein, including copyright rights, remain the sole and exclusive property of the Rightsholder. The license created by the exchange of an Order Confirmation (and/or any invoice) and payment by User of the full amount set forth on that document includes only those rights expressly set forth in the Order Confirmation and in these terms and conditions, and conveys no other rights in the Work(s) to User. All rights not expressly granted are hereby reserved.
  - 3.2. General Payment Terms: You may pay by credit card or through an account with us payable at the end of



This is a License Agreement between Yikai Jia ("User") and Copyright Clearance Center, Inc. ("CCC") on behalf of the Rightsholder identified in the order details below. The license consists of the order details, the CCC Terms and Conditions below, and any Rightsholder Terms and Conditions which are included below.

All payments must be made in full to CCC in accordance with the CCC Terms and Conditions below.

|                  |             |             |                                    |
|------------------|-------------|-------------|------------------------------------|
| Order Date       | 16-Mar-2022 | Type of Use | Republish in a thesis/dissertation |
| Order License ID | 1200453-1   | Publisher   | Elsevier Ltd                       |
| ISSN             | 2352-152X   | Portion     | Chapter/article                    |

## LICENSED CONTENT

|                   |  |                  |  |
|-------------------|--|------------------|--|
| Publication Title | Journal of Energy Storage  | Rightsholder     | Elsevier Science & Technology Journals |
| Article Title     | Thermal runaway propagation behavior within 18,650 lithium-ion battery packs: A modeling study | Publication Type | Journal                                |
|                   |  | Start Page       | 101668                                 |
|                   |  | Volume           | 31                                     |
| Date              | 01/01/2015   |                  |  |
| Language          | Dutch  |                  |  |
| Country           | United Kingdom of Great Britain and Northern Ireland   |                  |  |

## REQUEST DETAILS

|                                 |                         |                             |                         |
|---------------------------------|-------------------------|-----------------------------|-------------------------|
| Portion Type                    | Chapter/article         | Distribution                | Worldwide               |
| Page range(s)                   | 1-10                    | Translation                 | Other translation needs |
| Total number of pages           | 10                      | Enter languages             | English                 |
| Format (select all that apply)  | Print, Electronic       | Copies for the disabled?    | No                      |
| Who will republish the content? | Publisher, for profit   | Minor editing privileges?   | Yes                     |
| Duration of Use                 | Life of current edition | Incidental promotional use? | No                      |
| Lifetime Unit Quantity          | Up to 499               | Currency                    | USD                     |
| Rights Requested                | Main product            |                             |                         |

## NEW WORK DETAILS

|                 |  |                            |               |
|-----------------|--|----------------------------|---------------|
| Title           | MULTIPHYSICS NATURE OF LITHIUM-ION BATTERY SAFETY ISSUES | Institution name           | UNC Charlotte |
|                 |  | Expected presentation date | 2022-04-01    |
| Instructor name | YIKAI JIA  |                            |               |

## ADDITIONAL DETAILS

|                        |     |
|------------------------|-----|
| Order reference number | N/A |
|------------------------|-----|

The requesting person / organization to appear on the license Yikai Jia

## REUSE CONTENT DETAILS

|   |  |  |  |
|---|--|--|--|
| Title, description or numeric reference of the portion(s) | MULTIPHYSICS NATURE OF LITHIUM-ION BATTERY SAFETY ISSUES | Title of the article/chapter the portion is from | Thermal runaway propagation behavior within 18,650 lithium-ion battery packs: A modeling study |
| Editor of portion(s)                                      | Xu, Jun; Li, Yangxing; Uddin, Mesbah; Jia, Yikai         | Author of portion(s)                             | Xu, Jun; Li, Yangxing; Uddin, Mesbah; Jia, Yikai   |
| Volume of serial or monograph                             | 31   | Issue, if republishing an article from a serial  | N/A  |
| Page or page range of portion                             | 101668   | Publication date of portion                      | 2020-07-16   |

## RIGHTSHOLDER TERMS AND CONDITIONS

Elsevier publishes Open Access articles in both its Open Access journals and via its Open Access articles option in subscription journals, for which an author selects a user license permitting certain types of reuse without permission. Before proceeding please check if the article is Open Access on <http://www.sciencedirect.com> and refer to the user license for the individual article. Any reuse not included in the user license terms will require permission. You must always fully and appropriately credit the author and source. If any part of the material to be used (for example, figures) has appeared in the Elsevier publication for which you are seeking permission, with credit or acknowledgement to another source it is the responsibility of the user to ensure their reuse complies with the terms and conditions determined by the rights holder. Please contact [permissions@elsevier.com](mailto:permissions@elsevier.com) with any queries.

## CCC Terms and Conditions

1. Description of Service; Defined Terms. This Republication License enables the User to obtain licenses for republication of one or more copyrighted works as described in detail on the relevant Order Confirmation (the "Work(s)"). Copyright Clearance Center, Inc. ("CCC") grants licenses through the Service on behalf of the rightsholder identified on the Order Confirmation (the "Rightsholder"). "Republication", as used herein, generally means the inclusion of a Work, in whole or in part, in a new work or works, also as described on the Order Confirmation. "User", as used herein, means the person or entity making such republication.
2. The terms set forth in the relevant Order Confirmation, and any terms set by the Rightsholder with respect to a particular Work, govern the terms of use of Works in connection with the Service. By using the Service, the person transacting for a republication license on behalf of the User represents and warrants that he/she/it (a) has been duly authorized by the User to accept, and hereby does accept, all such terms and conditions on behalf of User, and (b) shall inform User of all such terms and conditions. In the event such person is a "freelancer" or other third party independent of User and CCC, such party shall be deemed jointly a "User" for purposes of these terms and conditions. In any event, User shall be deemed to have accepted and agreed to all such terms and conditions if User republishes the Work in any fashion.
3. Scope of License; Limitations and Obligations.
  - 3.1. All Works and all rights therein, including copyright rights, remain the sole and exclusive property of the Rightsholder. The license created by the exchange of an Order Confirmation (and/or any invoice) and payment by User of the full amount set forth on that document includes only those rights expressly set forth in the Order Confirmation and in these terms and conditions, and conveys no other rights in the Work(s) to User. All rights not expressly granted are hereby reserved.
  - 3.2.

General Payment Terms: You may pay by credit card or through an account with us payable at the end of the month. If you and we agree that you may establish a standing account with CCC, then the following terms apply: Remit Payment to: Copyright Clearance Center, 29118 Network Place, Chicago, IL 60673-1291. Payments Due: Invoices are payable upon their delivery to you (or upon our notice to you that they are available to you for downloading). After 30 days, outstanding amounts will be subject to a service charge of 1-1/2% per month or, if less, the maximum rate allowed by applicable law. Unless otherwise specifically set forth in the Order Confirmation or in a separate written agreement signed by CCC, invoices are due and payable on "net 30" terms. While User may exercise the rights licensed immediately upon issuance of the Order Confirmation, the license is automatically revoked and is null and void, as if it had never been issued, if complete payment for the license is not received on a timely basis either from User directly or through a payment agent, such as a credit card company.

- 3.3. Unless otherwise provided in the Order Confirmation, any grant of rights to User (i) is "one-time" (including the editions and product family specified in the license), (ii) is non-exclusive and non-transferable and (iii) is subject to any and all limitations and restrictions (such as, but not limited to, limitations on duration of use or circulation) included in the Order Confirmation or invoice and/or in these terms and conditions. Upon completion of the licensed use, User shall either secure a new permission for further use of the Work(s) or immediately cease any new use of the Work(s) and shall render inaccessible (such as by deleting or by removing or severing links or other locators) any further copies of the Work (except for copies printed on paper in accordance with this license and still in User's stock at the end of such period).
  - 3.4. In the event that the material for which a republication license is sought includes third party materials (such as photographs, illustrations, graphs, inserts and similar materials) which are identified in such material as having been used by permission, User is responsible for identifying, and seeking separate licenses (under this Service or otherwise) for, any of such third party materials; without a separate license, such third party materials may not be used.
  - 3.5. Use of proper copyright notice for a Work is required as a condition of any license granted under the Service. Unless otherwise provided in the Order Confirmation, a proper copyright notice will read substantially as follows: "Republished with permission of [Rightsholder's name], from [Work's title, author, volume, edition number and year of copyright]; permission conveyed through Copyright Clearance Center, Inc. " Such notice must be provided in a reasonably legible font size and must be placed either immediately adjacent to the Work as used (for example, as part of a by-line or footnote but not as a separate electronic link) or in the place where substantially all other credits or notices for the new work containing the republished Work are located. Failure to include the required notice results in loss to the Rightsholder and CCC, and the User shall be liable to pay liquidated damages for each such failure equal to twice the use fee specified in the Order Confirmation, in addition to the use fee itself and any other fees and charges specified.
  - 3.6. User may only make alterations to the Work if and as expressly set forth in the Order Confirmation. No Work may be used in any way that is defamatory, violates the rights of third parties (including such third parties' rights of copyright, privacy, publicity, or other tangible or intangible property), or is otherwise illegal, sexually explicit or obscene. In addition, User may not conjoin a Work with any other material that may result in damage to the reputation of the Rightsholder. User agrees to inform CCC if it becomes aware of any infringement of any rights in a Work and to cooperate with any reasonable request of CCC or the Rightsholder in connection therewith.
4. Indemnity. User hereby indemnifies and agrees to defend the Rightsholder and CCC, and their respective employees and directors, against all claims, liability, damages, costs and expenses, including legal fees and expenses, arising out of any use of a Work beyond the scope of the rights granted herein, or any use of a Work which has been altered in any unauthorized way by User, including claims of defamation or infringement of rights of copyright, publicity, privacy or other tangible or intangible property.
  5. Limitation of Liability. UNDER NO CIRCUMSTANCES WILL CCC OR THE RIGHTSHOLDER BE LIABLE FOR ANY DIRECT, INDIRECT, CONSEQUENTIAL OR INCIDENTAL DAMAGES (INCLUDING WITHOUT LIMITATION DAMAGES FOR LOSS OF BUSINESS PROFITS OR INFORMATION, OR FOR BUSINESS INTERRUPTION) ARISING OUT OF THE USE OR INABILITY

TO USE A WORK, EVEN IF ONE OF THEM HAS BEEN ADVISED OF THE POSSIBILITY OF SUCH DAMAGES. In any event, the total liability of the Rightsholder and CCC (including their respective employees and directors) shall not exceed the total amount actually paid by User for this license. User assumes full liability for the actions and omissions of its principals, employees, agents, affiliates, successors and assigns.

6. Limited Warranties. THE WORK(S) AND RIGHT(S) ARE PROVIDED "AS IS". CCC HAS THE RIGHT TO GRANT TO USER THE RIGHTS GRANTED IN THE ORDER CONFIRMATION DOCUMENT. CCC AND THE RIGHTSHOLDER DISCLAIM ALL OTHER WARRANTIES RELATING TO THE WORK(S) AND RIGHT(S), EITHER EXPRESS OR IMPLIED, INCLUDING WITHOUT LIMITATION IMPLIED WARRANTIES OF MERCHANTABILITY OR FITNESS FOR A PARTICULAR PURPOSE. ADDITIONAL RIGHTS MAY BE REQUIRED TO USE ILLUSTRATIONS, GRAPHS, PHOTOGRAPHS, ABSTRACTS, INSERTS OR OTHER PORTIONS OF THE WORK (AS OPPOSED TO THE ENTIRE WORK) IN A MANNER CONTEMPLATED BY USER; USER UNDERSTANDS AND AGREES THAT NEITHER CCC NOR THE RIGHTSHOLDER MAY HAVE SUCH ADDITIONAL RIGHTS TO GRANT.
7. Effect of Breach. Any failure by User to pay any amount when due, or any use by User of a Work beyond the scope of the license set forth in the Order Confirmation and/or these terms and conditions, shall be a material breach of the license created by the Order Confirmation and these terms and conditions. Any breach not cured within 30 days of written notice thereof shall result in immediate termination of such license without further notice. Any unauthorized (but licensable) use of a Work that is terminated immediately upon notice thereof may be liquidated by payment of the Rightsholder's ordinary license price therefor; any unauthorized (and unlicensable) use that is not terminated immediately for any reason (including, for example, because materials containing the Work cannot reasonably be recalled) will be subject to all remedies available at law or in equity, but in no event to a payment of less than three times the Rightsholder's ordinary license price for the most closely analogous licensable use plus Rightsholder's and/or CCC's costs and expenses incurred in collecting such payment.
8. Miscellaneous.
  - 8.1. User acknowledges that CCC may, from time to time, make changes or additions to the Service or to these terms and conditions, and CCC reserves the right to send notice to the User by electronic mail or otherwise for the purposes of notifying User of such changes or additions; provided that any such changes or additions shall not apply to permissions already secured and paid for.
  - 8.2. Use of User-related information collected through the Service is governed by CCC's privacy policy, available online here: <https://marketplace.copyright.com/rs-ui-web/mp/privacy-policy>
  - 8.3. The licensing transaction described in the Order Confirmation is personal to User. Therefore, User may not assign or transfer to any other person (whether a natural person or an organization of any kind) the license created by the Order Confirmation and these terms and conditions or any rights granted hereunder; provided, however, that User may assign such license in its entirety on written notice to CCC in the event of a transfer of all or substantially all of User's rights in the new material which includes the Work(s) licensed under this Service.
  - 8.4. No amendment or waiver of any terms is binding unless set forth in writing and signed by the parties. The Rightsholder and CCC hereby object to any terms contained in any writing prepared by the User or its principals, employees, agents or affiliates and purporting to govern or otherwise relate to the licensing transaction described in the Order Confirmation, which terms are in any way inconsistent with any terms set forth in the Order Confirmation and/or in these terms and conditions or CCC's standard operating procedures, whether such writing is prepared prior to, simultaneously with or subsequent to the Order Confirmation, and whether such writing appears on a copy of the Order Confirmation or in a separate instrument.
  - 8.5. The licensing transaction described in the Order Confirmation document shall be governed by and construed under the law of the State of New York, USA, without regard to the principles thereof of conflicts of law. Any case, controversy, suit, action, or proceeding arising out of, in connection with, or related to such licensing transaction shall be brought, at CCC's sole discretion, in any federal or state court located in the County of New York, State of New York, USA, or in any federal or state court whose geographical

jurisdiction covers the location of the Rightsholder set forth in the Order Confirmation. The parties expressly submit to the personal jurisdiction and venue of each such federal or state court. If you have any comments or questions about the Service or Copyright Clearance Center, please contact us at 978-750-8400 or send an e-mail to [support@copyright.com](mailto:support@copyright.com).

v 1.1